Surface Science Studies of Model Metal Oxide Systems

Bobbie-Jean Àine Shaw

Thesis submitted for the Degree of Doctor of Philosophy of the University College London

Department of Chemistry

UNIVERSITY COLLEGE LONDON

2016

I, Bobbie-Jean Shaw, confirm that the work presented in this thesis is my own. Where information has been derived from other sources, I confirm that this has been indicated in the thesis.

Bobbie-Jean Shaw

September 2016

ABSTRACT

The work presented in this thesis details the investigation of two important metal oxides: ultrathin films of CeO_2(111) and single crystal rutile TiO_2(110).

Near ambient pressure photoelectron spectroscopy (NAPPES) has been used to investigate the effects of temperature, and water and oxygen adsorption on the band gap state of rutile TiO_2(110). This state has long been attributed to bridging oxygen vacancies, hydroxyls and, more recently, also to subsurface titanium interstitials and oxygen vacancies. In this experiment the non-stoichiometric rutile TiO_2(110) surface was exposed to water and oxygen at an array of temperatures whilst monitoring the band gap state and other core-level spectra. Our results show that temperature, oxygen and high pressures of water have a marked effect on the band gap state of rutile TiO_2(110).

Scanning tunnelling microscopy (STM), low-energy electron diffraction (LEED) and Auger electron spectroscopy (AES) have been employed to study the structure and growth of ultrathin CeO_2(111) films supported on Pt(111) and Rh(111). Atomically resolved STM images of these ultrathin films have been obtained, which allowed for examination of the defect structure of these thin films, in addition to the nucleation sites of certain adsorbates. To this effect, the behaviour of individual Au atoms at room temperature on this surface has been investigated, whereby it was observed that the single Au adatoms exhibited no preferential adsorption site.

The growth and structure of iron nanowires supported on rutile TiO_2(110) has also been investigated with low energy electron microscopy (LEEM), X-ray photoemission electron microscopy (XPEEM), scanning tunnelling microscopy (STM) and atomic force microscopy

(AFM). The nanowires were grown by the deposition of iron onto the substrate, which was held at an elevated temperature. The magnetic domain structure was studied using X-ray magnetic circular dichroism (XMCD) and spin-polarised low energy electron microscopy (SPLEEM). The chemical analysis of the nanowires was performed via micro X-ray photoelectron spectroscopy (μ-XPS) and X-ray absorption spectroscopy (XAS). Our experimental results indicate that the growth orientation of the nanowires is dictated by the anisotropy of the substrate, i.e. the nanowires grow along the [001] direction of the substrate. The iron nanowires possess an iron core appear and the larger structures appear to be encapsulated by mixed Fe-Ti oxides, possible a combination of $FeTiO_3$ and α-Fe_2O_3, whilst the smaller ones display a (3×3) oxygen overlayer. A magnetic contrast was only observed in XMCD, which we attribute to the difference in sensitivity between this technique and SPLEEM.

To my Father…

ACKNOWLEDGEMENTS

I would like to start by thanking my supervisor Prof. Geoff Thornton, for all his wisdom and guidance during the course of my PhD studies and for giving me the opportunity to work in a field I love. I would also like to thank all the members of the Thornton group that I had the privilege to work with, for their invaluable help and companionship. Dr. David Grinter deserves special recognition for all his patience, assistance, and above all friendship, over the last few years for which I am truly grateful. Dr. Chi Pang and Dr. Oliver Yim must also be thanked for all their good advice and assistance.

I was given the opportunity to partake in experiments with some truly amazing people, and I would like so say a special thank you Dr. Chris Muryn, Dr. Francesco Maccherozzi, Dr. Sarnjeet Dhesi, Dr. Greg Cabailh, Prof. Takanori Koshikawa, Dr. Masahiko Suzuki, Prof. Tsuneo Yasue and Ms. Yuri Inaoka.

I would also like to thank Prof. Ana Cristina Gomes Silva for her advice and relentless encouragement, and Dr. Nenad Bundaleski, who inspired me to love science.

A big thank you to Mr. Luís Reino, my rock, for believing in me and supporting my dreams. Last, but not least, I thank my family for their unconditional love and patience.

PUBLICATIONS LIST

Spectromicroscopy of a Model Water-Gas-Shift Catalyst: Gold Nanoparticles Supported on Ceria.

D. C. Grinter, C. Muryn, B. Santos, B. J. Shaw, T. O. Menteş, A. Locatelli, G. Thornton
Journal of Physical Chemistry C, 118, 19194-19204, **2014**

Diffusion Barriers Block Defect Occupation on Reduced CeO_2 (111.)

P. G. Lustemberg, Y. Pan, B. J. Shaw, D. Grinter, C. Pang, G. Thornton, R. Pérez, M. V. Ganduglia-Pirovano, N. Nilius
Physical Review Letters, 116, 236101, **2016**

GLOSSARY

AES	Auger Electron Spectroscopy
AFM	Atomic Force Microscopy
ALS	Advanced Light Source
BE	Binding Energy
CB	Conduction Band
CVD	Chemical Vapour Deposition
DFT	Density Functional Theory
DLS	Diamond Light Source
eV	Electron Volt
FEL	Fast Entry Loadlock
FFT	Fast Fourier Transform
IMFP	Inelastic Mean Free Path
LEED	Low Energy Electron Diffraction
LEEM	Low Energy Electron Microscopy
LDOS	Local Density of States
ML	Monolayer
MS	Mass Spectrometry
NAPPES	Near-Ambient Photoelectron Photoemission Spectroscopy
NC-AFM	Non-Contact Atomic Force Microscopy
PEEM	Photoemission Electron Microscopy
PES	Photoemission Spectroscopy
PVD	Physical Vapour Deposition

QMS	Quadrupole Mass Spectrometer
RESPES	Resonant Photoemission Spectroscopy
RFA	Retarding Field Analysis
RGA	Residual Gas Analysis
RH	Relative Humidity
RT	Room Temperature
SPM	Scanning Probe Microscope
STM	Scanning Tunnelling Microscopy
SV	Start Voltage
TSP	Titanium Sublimation Pump
UCL	University College London
UHV	Ultra High Vacuum
VB	Valence Band
VT-STM	Variable Temperature Scanning Tunnelling Microscopy
WGS	Water-Gas-Shift
WKB	Wentzel-Kramers-Brillouin
XAS	X-ray Absorption Spectroscopy
XMCD	X-ray Magnetic Circular Dichroism
XMLD	X-ray Magnetic Linear Dichroism
XPEEM	X-ray Photoemission Electron Microscopy
XPS	X-ray Photoelectron Spectroscopy
SPELEEM	Spectroscopic Photoemission and Low Energy Electron Microscope
SPLEEM	Spin Polarised Low Energy Electron Microscopy
μ **-XPS**	Micro X-ray Photoelectron Spectroscopy

TABLE OF CONTENTS

LIST OF FIGURES

CHAPTER 1

INTRODUCTION

1.1 The Surface Science of Metal Oxides

The term *surface science* dates back to the early 1960's, and encompasses the study of physical and chemical phenomena that occur at solid surfaces or at the interface between solid-gas, solid-liquid or solid-vacuum phases. One of the early motivations for the study of surfaces was the elucidation of the atomic level mechanisms underlying heterogeneous catalysis, and this spurred the development of experimental techniques with unparalleled capabilities. Amongst the plethora of catalytic processes, the most notable include the Haber-Bosch for ammonia synthesis, the Fischer-Tropsch for synthesis gas transformation, and the three-way-catalyst for exhaust gas purification [1].

The majority of the catalytic systems of interest are extremely complex, thus simplifications are performed to exclude unnecessary interferents. Therefore, the majority of surface science experiments are usually performed on single crystal surfaces under well-controlled conditions, i.e. ultra high vacuum (UHV). These conditions are not representative of the real operating

environments of most catalyst systems and results in the termed *materials* or *pressure gap*, which must be contemplated when extrapolating the results of model systems to realistic ones. In recent years, much effort has been made to bridge these gaps by developing scientific instrumentation capable of performing surface science experiments in more technologically relevant conditions, for example at near ambient pressures [2-4].

Since the inception of surface science, its associated experimental techniques have experienced considerable progress. Most notably, advances in the field of scanning probe microscopy (SPM) have made atomic level imaging, chemical specificity and atomic manipulation a reality [5]. One of the most infamous examples of the latter is the image of IBM spelled out on a nickel substrate using single xenon atoms by Eigler *et al*. [6].

The initial focus of surface science studies was predominantly on metals and semiconductors, due to their relative structural, chemical and physical simplicity and ease of preparation. However, the discovery of the outstanding catalytic properties of metal oxides, and the realisation that the majority of metal surfaces appear oxidised in ambient conditions, drove surface scientists to concentrate their efforts on this fascinating class of materials. One of the major landmarks in the study of these materials was the discovery of the photocatalytic ability of titanium dioxide (TiO_2) to dissociate water without the application of an external voltage, by Fujishima and Honda in 1972 [7].

Metal oxides cover a broad spectrum of physical and chemical properties; for example some oxides are exceptional superconductors yet others are the best insulators, some are sufficiently inert to function as corrosion protection layers, whereas others are so chemically active they are applied as catalysts [8]. A large number of technologically important oxides are good insulators, which makes their study problematic when using electron-based techniques due to charging. Such surface science techniques include scanning tunnelling microscopies and photoemission spectroscopies, which are implemented throughout the work presented in this thesis. Two of the

most common methods are n-type doping of the oxide via high temperature annealing, and growth of ultrathin oxide films on conducting metal substrates. The former method is the preferred preparation method for rutile TiO_2, resulting in the reduction of the oxide that is evidenced by the change of the crystal colour from transparent to dark blue [9]. The latter procedure is the favoured method for the growth of, for example, cerium dioxide (CeO_2) ultrathin films [10].

1.2 Titanium Dioxide

Titanium dioxide, titania or TiO_2 is regarded as the prototypical metal oxide surface and has been one of the most investigated of all metal oxides, with applications in a variety of fields of including water purification [11], gas sensing [12], solar cells [13] and electronic devices [14].

There are three polymorphs of TiO_2, rutile, anatase and brookite. Rutile titania, specifically its (110) surface, is the thermodynamically most stable of the three structures at higher temperatures and also the most dominant in the literature, despite not displaying the highest catalytic activity [9,15]. The anatase polymorph of titania is the most photoactive, and the (101) face is its thermodynamically most stable surface. The bandgap of TiO_2 is approximately 3.4 eV for anatase and 3.0 eV for rutile, thus titania absorbs the ultraviolet part of the solar spectrum. The scarcity of literature on anatase in comparison to rutile is mainly due to difficulty in obtaining natural mineral samples with sufficient purity or growing large synthetic single crystals [15]. A comprehensive summary of the applications, surface and bulk structure, chemical properties and interaction with different adsorbate atoms is provided in the reviews of Diebold [9] and Pang *et al*. [16].

1.3 Cerium Dioxide

Cerium dioxide, ceria, or CeO_2 is a widely used material with a vast number of industrial applications including as a main component in the three-way catalytic converter for automotive exhaust gas purification [17,18], as an electrolyte in fuel cells [19], and as a heterogeneous catalyst for a growing number technological relevant processes [20,21]. One of the most high profile applications was discovered by Fu *et al*., when gold nanoparticles supported on ceria were observed to be a powerful catalyst for the low temperature water-gas-shift reaction, which is used for the production of hydrogen as a green alternative to fossil fuels [22]. The success of ceria in all these applications relies on the ability of cerium to cycle between the Ce^{3+} and Ce^{4+} oxidation states and the high mobility of lattice oxygen, which permits facile oxidation and reduction in addition to excellent oxygen storage and release capacity during reactions [23,24].

Ceria is insulating at room temperature due to its wide band gap of about 6 eV, which makes the study of this material problematic when using electron-based techniques. In order to reduce charging many preparation methods have been devised, these include doping of the crystal [25] and conducting the experiment at elevated temperatures [26]. However, a different approach was taken for the work presented in this thesis whereby CeO_2(111) ultrathin films were grown epitaxially on conducting metal substrates, namely Pt(111) and Rh(111).

1.4 Thesis Overview

The work presented in this thesis focuses on the two aforementioned metal oxides, titanium dioxide (TiO_2) and cerium dioxide (CeO_2), in the form of singles crystals for the former and ultrathin films in the case of the latter. The experiments described in this thesis aim to explore the interaction of these metal oxide surfaces with various adsorbates using several surface science techniques, the details of which will be explained below.

In chapter 2 of this thesis, the theoretical aspects of the surface science techniques employed for the investigation of the metal oxide systems are examined. An understanding of the physical principles that govern the experimental techniques is vital for a correct interpretation of the experimental results. The designated techniques are scanning tunnelling microscopy (STM), low energy electron diffraction (LEED), Auger electron spectroscopy (AES), X-ray photoelectron spectroscopy (XPS), X-ray adsorption spectroscopy (XAS), X-ray photoemission electron microscopy (XPEEM), low energy electron microscopy (LEEM), X-ray magnetic circular and linear dichroism (XMCD and XMLD) and spin-polarised low energy electron microscopy (SPLEEM).

Chapter 3 describes the instrumentation used to perform the research presented in chapters 4 to 6 of this thesis, specifically an *Omicron* variable temperature scanning tunnelling microscope (VT-STM), a spin polarised low energy electron microscope (SPLEEM); a spectroscopic photoemission and low energy electron microscope (SPELEEM), and an ambient pressure photoelectron spectroscopy (APPES) apparatus; the operation and features of the auxiliary equipment used for sample preparation and characterisation are also discussed.

The first chapter of results is presented in chapter 4. This section discusses a near-ambient photoelectron study of water on rutile TiO_2(110), in which the titania surface was exposed to increasing amounts of water while XPS spectra were simultaneously acquired. The main objective of this study was to observe the affect of water adsorption on the band gap state of rutile TiO_2, which is thought to play a crucial role in photocatalysis in technologically relevant conditions.

Chapter 5 details the characterisation of a model catalyst system for the low temperature water-gas-shift reaction, where H and CO_2 are produced from H_2O and CO. CeO_2(111) ultrathin films were grown on Pt(111) and Rh(111) substrates and characterised using STM, LEED and AES.

Moreover, gold nanoparticles were deposited *in situ* on these films, and their interaction with the $CeO_2(111)$ surface structure was investigated on an atomic level by STM.

The final section of results is disclosed in chapter 6, and consists of a magnetic, chemical and topographic characterisation study of iron nanostructures on rutile $TiO_2(110)$ that take on two different forms, that of elongated nanowires and also pseudohexagonal islands. In addition, a real time growth study of the Fe nanostructures was also performed. Two separate instruments were used in this study, SPELEEM and SPLEEM. The former is capable of magnetic, topographic and elemental contrast, and the latter is limited to magnetic and topographic contrast mechanisms.

References

[1] K.W. Kolasinski, Surface Science, John Wiley & Sons, 2008.

[2] D.F. Ogletree, H. Bluhm, G. Lebedev, C.S. Fadley, Z. Hussain, M. Salmeron, Rev. Sci. Instrum. 73 (2002) 3872.

[3] K. Andersson, G. Ketteler, H. Bluhm, S. Yamamoto, H. Ogasawara, L.G.M. Pettersson, M. Salmeron, A. Nilsson, J Phys Chem C 111 (2007) 14493.

[4] A. Křepelová, T. Bartels-Rausch, M.A. Brown, H. Bluhm, M. Ammann, J Phys Chem A 117 (2013) 401.

[5] A. Zhao, S. Tan, B. Li, B. Wang, J. Yang, J.G. Hou, Phys. Chem. Chem. Phys. 15 (2013) 12428.

[6] D.M. Eigler, E.K. Schweizer, Nature 344 (1990) 524.

[7] A. Fujishima, K. Honda, Nature 238 (1972) 37.

[8] U. Diebold, S.-C. Li, M. Schmid, Annu. Rev. Phys. Chem. 61 (2010) 129.

[9] U. Diebold, Surf Sci Rep 48 (2003) 53.

[10] H.-J. Freund, G. Pacchioni, Chem. Soc. Rev. 37 (2008) 2224.

[11] D. Suryaman, K. Hasegawa, J Hazard Mater 183 (2010) 490.

[12] D. Buso, M. Post, C. Cantalini, Advanced … (2008).

[13] S. So, K. Lee, P. Schmuki, Phys. Status Solidi RRL 6 (2012) 169.

[14] S.K. Kim, K.M. Kim, D.S. Jeong, W. Jeon, K.J. Yoon, C.S. Hwang, J. Mater. Res. 28 (2012) 313.

[15] M.J. Jackman, A.G. Thomas, C. Muryn, J Phys Chem C 119 (2015) 13682.

[16] C.L. Pang, R. Lindsay, G. Thornton, Chem. Rev. (2013) 130515130929008.

[17] J. Kašpar, P. Fornasiero, Journal of Solid State Chemistry (2003).

[18] S. Matsumoto, Catalysis Today 90 (2004) 183.

[19] G. Jacobs, Applied Catalysis a: General 252 (2003) 107.

[20] R.J. Gorte, AIChE J. (2010) NA.

[21] A. Trovarelli, P. Fornasiero, Catalysis by Ceria and Related Materials, 2013.

[22] Q. Fu, Science 301 (2003) 935.

[23] Z.-P. Liu, S. Jenkins, D. King, Phys. Rev. Lett. 94 (2005).

[24] S. Bernal, J.J. Calvino, M.A. Cauqui, J.M. Gatica, C. Larese, J.A. Pérez Omil, J.M. Pintado, Catalysis Today 50 (1999) 175.

[25] M. Nolan, V.S. Verdugo, H. Metiu, Surf Sci 602 (2008) 2734.

[26] F. Esch, Science 309 (2005) 752.

CHAPTER 2

THEORETICAL ASPECTS OF INSRUMENTATION

Abstract

This chapter aims to review the theoretical aspects of the surface science techniques used in this thesis, specifically Scanning Tunnelling Microscopy (STM), Low Energy Electron Diffraction (LEED), Auger Electron Spectroscopy (AES), X-ray Photoelectron Spectroscopy (XPS), X-ray Photoemission Electron Microscopy (XPEEM), Spin-Polarised Low Energy Electron Microscopy (SPLEEM), X-ray Magnetic Circular Dichroism (XMCD) and Low Energy Electron Microscopy (LEEM).

2.1 Scanning Tunnelling Microscopy

Since its invention in the early 1980s by Gerd Binnig and Heinrich Rohrer, the scanning tunnelling microscope (STM) has enabled the imaging of surfaces with unprecedented resolution and helped shape the fields of surface science and nanotechnology [1,2]. This revolutionary technique has made possible the routine imaging of surfaces at an atomic scale, and even the individual manipulation and spectroscopic characterisation of molecules and single atoms [3-5].

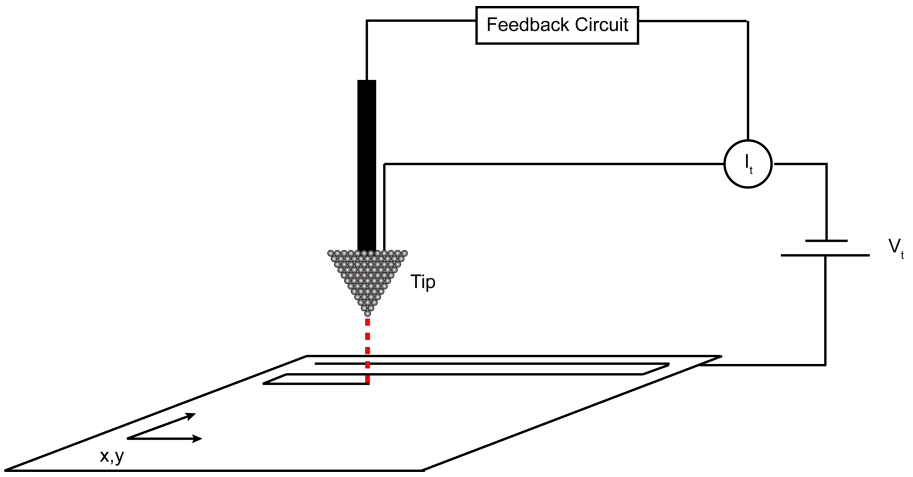

Figure 2.1 - Schematic diagram of the basic experimental setup of an STM. An atomically sharp tip is rastered across a surface and the tip-sample separation is controlled using a feedback loop.

STM is based on the concept of quantum mechanical tunneling and is performed by instruments of surprisingly simple design, as depicted in figure 2.1. In STM, an atomically sharp metal tip is brought within a few Ångström of the surface of a conducting or semi-conducting sample and a small bias voltage is applied between the two. When the tip-sample separation is such that their wavefunctions overlap, a finite probability for electrons to tunnel between them exists, without the requirement for mechanical contact. As the tip is scanned over the sample, the resulting tunneling current is measured and a contour map of the surface is formed; a precise control of the vertical position z of the tip is possible owing to the exponential dependence of the tunneling current on the tip-sample distance.

Classical physics postulates that an electron can only traverse the potential barrier imposed by tip-sample separation if the kinetic energy of the electron is greater than that of the barrier. On the other hand however, quantum mechanics predicts a finite transmission probability, which may be calculated by likening the tip-sample separation to a one-dimensional tunneling problem as described below.

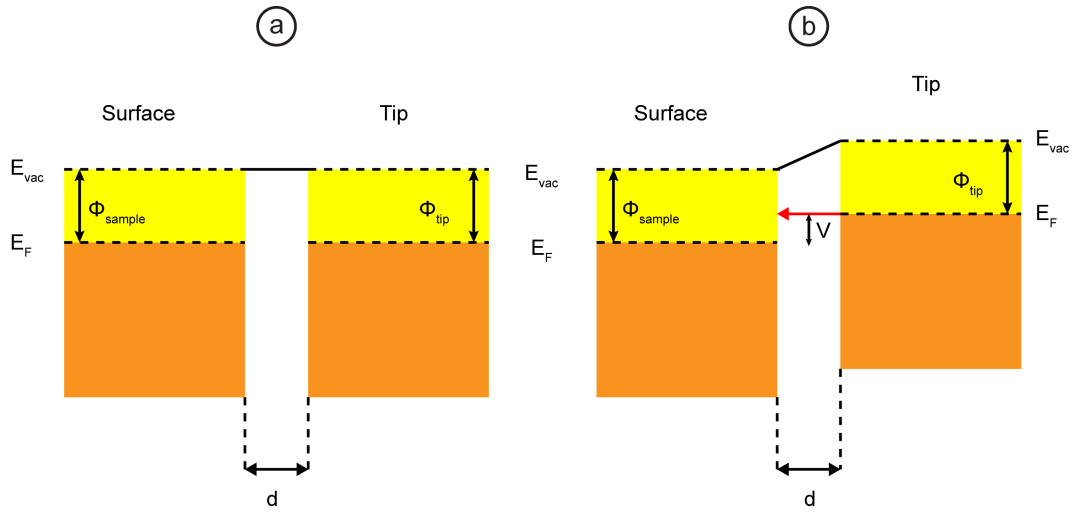

Figure 2.2 – Diagram depicting the band structure and potential barrier between the sample surface and the tip when a) no bias voltage is applied and b) a bias voltage V is applied. The tip-sample separation is represented by d, and E_{vac} and E_F are the vacuum and Fermi levels, respectively.

The wavefunction Ψ of an electron found within a rectangular barrier is given by the solutions to the Schrödinger equation in one-dimension z as displayed in equation 2.1:

$$\psi(z) = e^{-\kappa z} \tag{2.1}$$

where $\kappa^2 = 2m(V_B - E)/\hbar^2$ is the decay constant that depends on the potential of the barrier V_B, the energy of the state E and the electron mass m. The barrier height V_B is not constant across the gap, as evidenced in figure 2.2, however in the presence of a small bias voltage an average value can be used instead. In the simplest case V_B is the vacuum level, so for electrons occupying states at the Fermi level, $V_B - E$ is simply equal to the workfuntion ϕ. In the low bias voltage and temperature range, the tunneling current I is given by equation 2.2:

$$I \propto e^{-2\kappa d} \tag{2.2}$$

thus the tunneling current decays exponentially with the barrier width d [4,6]. Since a typical workfuntion has a value of few eV, 2κ is approximately 2 Å^{-1}, implying an order of magnitude change in I when d is varied by 1 Å; it is this exponential current-distance relationship that confers STM such topographical sensitivity. This very simple description provides a basic explanation of the exponential dependency of the tunnelling current on the tip-sample separation, yet more complex formalisms are required to explain the tunnelling process in more detail, such as those devised by Tersoff and Hamann [7,8], Chen [9], Lang [10-12], and Wentzel-Kramers-Brillouin [13].

2.1.1 Tersoff and Hamann Model

The preeminent quantitative theory of the tunneling current in STM stemmed from Bardeen's perturbation theory and was developed by Tersoff and Hamann. As the prevailing factor governing STM imaging is the relative change in tunneling current across the surface, rather than its absolute value, Bardeen's perturbation theory was suitably applied even though the wavefunction tail in the gap region is not rigorously treated. The tunneling current formalism as proposed by Bardeen is given by equation 2.3:

$$I = \frac{2\pi e}{\hbar} \sum_{\mu,\upsilon} f(E_\mu)[1 - f(E_\upsilon + eU)] \left|M_{\mu\nu}\right|^2 \delta(E_\mu - E_\nu) \tag{2.3}$$

where $f(E)$ is the Fermi function, U is the applied voltage bias, $M_{\mu\nu}$ is the tunnelling matrix element between the states $\psi_\mu$of the tip and ψ_ν of the surface, and E_μ and E_ν are the respective energy of each state in the absence of tunneling. In the low temperature and small voltage limit equation 2.3 is reduced to:

$$I = \frac{2\pi}{\hbar} e^2 V \sum_{\mu,\nu} \left|M_{\mu\nu}\right|^2 \delta(E_\nu - E_F)\, \delta(E_\mu - E_F) \tag{2.4}$$

where E_F is the Fermi level. To solve equation 2.4, the matrix element $M_{\mu\nu}$ needs to be calculated. Bardeen demonstrated that the matrix elements $M_{\mu\nu}$ can be expressed by equation 2.5, where the integral $\int dS$ is over any surface within the barrier region [14].

$$M_{\mu\nu} = \frac{\hbar}{2m}\int \left(\psi_\mu^* \nabla\psi_\nu - \psi_\nu \nabla\psi_\mu^*\right) dS \tag{2.5}$$

The tunnelling current is a convolution of electronic states of the tip to those of the sample, however determination of the wavefuntions is not trivial. Tersoff and Hamann thus proposed that the tip be modelled as a simple point probe that would yield maximum resolution, as depicted in figure 2.3. Furthermore, as the STM image is solely related to the properties of the surface, the STM measures an intrinsic property of the surface, rather than a property of the surface-tip system [6]. Based on this assumption, the matrix element is proportional to the amplitude of ψ_ν at the position r_0 of the tip, and hence equation 2.5 simplifies to:

$$I \propto \sum_\nu |\psi_\nu(r_t)|^2 \delta(E_\nu - E_F) \equiv \rho(r_t, E_F) \tag{2.6}$$

This result demonstrates that, for low bias voltages, the tunnelling current is proportional to the surface charge density arising from states at E_F, i.e. the surface local density of states $\rho(r_t, E_F)$ at E_F [6]. Therefore, STM images represent a contour map of constant surface local density of states (LDOS). When higher bias voltages are applied, it is a plausible assumption that equation 2.6 could be easily generalised to the simple expression of equation 2.7:

$$I \sim \int_{E_F}^{E_F+V} \rho(r_t, E)\, dE \tag{2.7}$$

This expression neglects the energy dependence of the matrix elements and the tip density of states. Nevertheless, it is still a reasonable approximation for higher bias voltages as long as the voltage is much smaller that the workfunction, $(V \ll \phi)$ [6]. Although simplistic in nature, Tersoff and Hamman's formalism predicts that STM images display the LDOS at E_F, as later confirmed by more complex models.

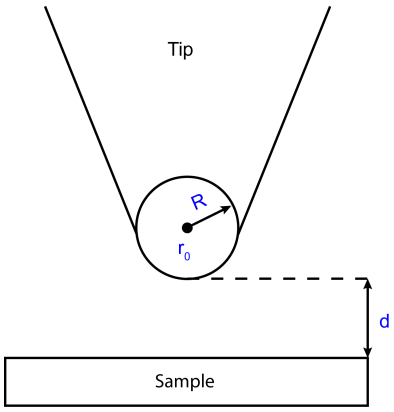

Figure 2.3 – Model of the tip used in the Tersoff and Hamman approximation [8].

2.1.1 Chen Model

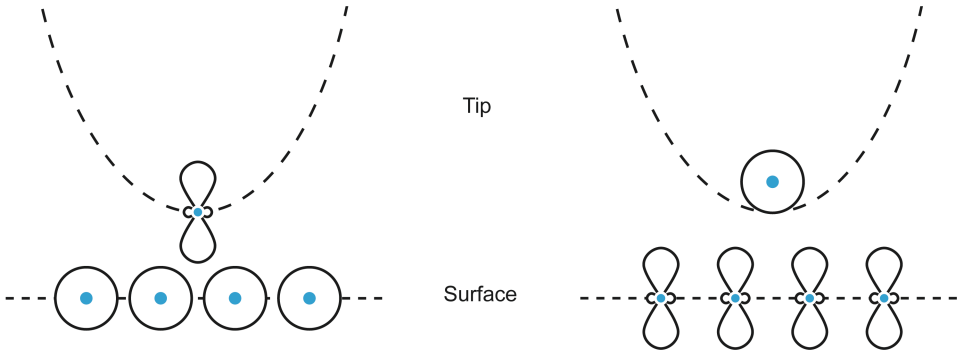

Figure 2.4 – Illustration of Chen's reciprocity principle demonstrating that scanning an *s* sample with a d_{z^2}-terminated tip is equivalent to scanning a d_{z^2} sample with an *s*-terminated tip in STM [9].

The tunneling model proposed by Tersoff and Hamann estimated a maximum lateral resolution of about 6 Å, however features with a spacing as low as 2 Å were observed experimentally [15]. As a result, an extension to the earlier model was formulated by Chen, which accommodates more detailed models of the tip structure and predicted atomic resolution on metal surfaces [9]. Most common tip materials include tungsten (W), platinum (Pt) and iridium (Ir), which are *d* band metals and have a Fermi level density of states originating primarily from *d* states. As such, it seems inappropriate to model *d* band metal tips using an *s*-wave

approximation. Moreover, first-principle calculations also reveal the existence of d_{z^2} dangling-bond states near the Fermi level of W which are thought to play a major role in tunnelling [4]. Chen also introduced the reciprocity principle, illustrated in figure 2.4. According to this principle, scanning an *s* wave sample using a d_{z^2} tip is equivalent to an *s* wave tip scanning a d_{z^2} sample.

2.1.2 Lang Model

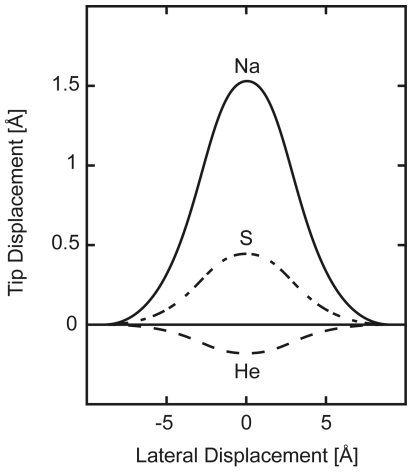

Figure 2.5 – Calculated tip displacement ΔZ versus lateral displacement ΔY for an STM scan of Na, S, and He adsorbate atoms on a jellium surface at a small bias voltage [11].

In order to ascertain the effect of different adsorbates on STM imaging, Lang performed calculations using the Bardeen tunneling formulism and represented the tip (Na) and the sample (He, Na or S) using two planer electrodes [10-12]. The results are displayed in figure 2.5 and show the result of constant current scans over the three different surfaces. Scanning over the Na and S atoms leads to an increase in the LDOS at the Fermi level owing to Na *3s* and S *2p* resonances. In the case of He, the metal states are polarised away from the Fermi level during scanning, resulting in a reduction in the LDOS. This change in the LDOS results in the adsorbates appearing as either protrusions (Na, S) or depressions (He) when the STM is operated in constant current mode. These findings emphasize the non-triviality of STM image

analysis and the importance of theoretical calculations as a tool for accurate interpretation.

2.1.3 Wentzel-Kramers-Brillouin Approximation

The study of semi-conducting materials, such as metal oxides, requires the use of a high voltage bias during scanning, typically in the range of 1-4 V. The Tersoff and Hamman theory was developed for low voltages and, as such, doesn't account for tunneling current contributions from states situated below the Fermi level. Therefore, in the case of high bias voltages the semi-classical Wentzel-Kramers-Brillouin (WKB) approximation is better suited. In this model, the tunneling probability is calculated between two planar electrodes at zero temperature and the resultant tunnelling current is the integral over the energy range where both filled-initial and empty-final states are available for tunnelling [6,13]. The tunnelling current in the WKB theory is of the form:

$$I = \int_0^{eV} \rho_s(r,E)\, \rho_t(r,-eV,+E)\, T(E,eV,r)\, dE \tag{2.8}$$

where $\rho_s(r,E)$ and $\rho_t(r,E)$ are the density of states of the sample and tip at location r and energy E, measured with respect to their Fermi levels, when the sample is biased negatively $eV < 0$, and when a positive biased is used $eV > 0$. The tunnelling transmission probability T for electrons with energy E and applied bias voltage V at a tip-sample separation z is given by equation 2.9:

$$T(z,E,eV) = \exp\left(-\frac{2z\sqrt{2m}}{\hbar}\sqrt{\frac{\Phi_s+\Phi_t}{2}+\frac{eV}{2}-E}\right) \tag{2.9}$$

The tunnelling transmission probability T is largest for $E = 0$ if $eV < 0$ and $E = eV$ if $eV > 0$,

i.e. if a negative bias is applied to the sample, the tunnelling probability is largest for electrons at the Fermi level of the sample, and if the sample is biased positively then the probability is largest for the electrons at the Fermi level of the tip. In other words, the tunnelling probability is largest for electrons at the Fermi level of the negatively biased electrode [16].

2.2 Low Energy Electron Diffraction

The experimental confirmation of the wave nature of electrons postulated by Louis de Broglie in 1924 [17], was first achieved by Clinton Davisson [18] and George Thompson [19] in the 1920s. Their experimental findings paved the way for the development of low energy electron diffraction (LEED), which has become a fundamental technique for the determination of the structure of surfaces. De Broglie postulated that the wavelength of an electron is given by equation 2.10:

$$\lambda = \frac{h}{\sqrt{2m_e E}} \tag{2.10}$$

where h is Planck's constant, m_e is the mass of the electron and E is the kinetic energy of the electron. The kinetic energy of electrons employed in LEED experiments typically range from 20 to 200 eV, which corresponds to wavelengths of between 2.74 and 0.87 Å. This order of magnitude is commensurate with the interatomic distances of many crystalline solids, and hence the atomic diffraction condition is satisfied [20,21]. Moreover, owing to the very short inelastic mean free path of the low-energy electrons (<10 Å), LEED is a very surface sensitive technique because the electrons only probe the topmost layers of the sample surface. A plot of the mean free path of electrons versus kinetic energy for a number of elements is displayed in figure 2.6, and highlights the surface sensitivity inherent in using electrons with energies in the range 10-1000 eV.

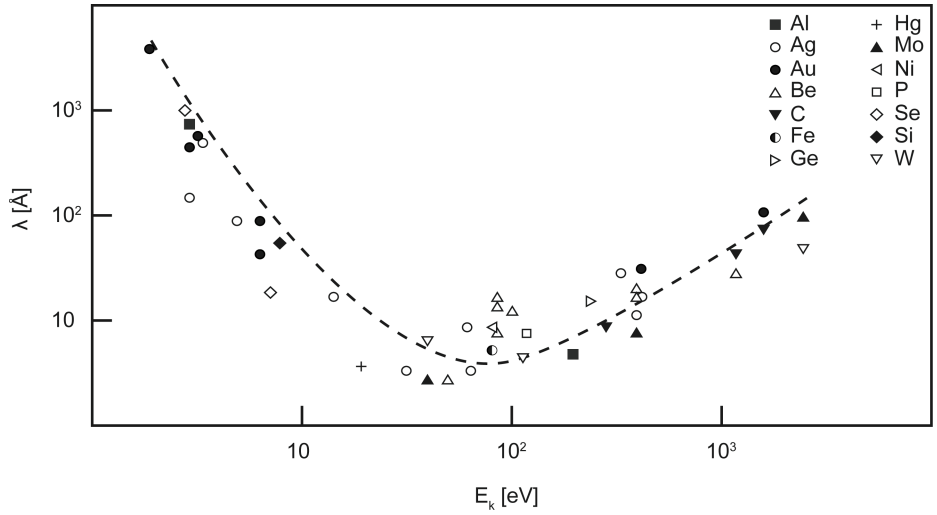

Figure 2.6 – Theoretical and experimental mean free path values of an electron λ versus kinetic energy E_k for various elements, highlighting the surface sensitivity of the low energy electrons used in techniques such as LEED [22].

Figure 2.7 illustrates the process of diffraction from 1D atomic lattice, which is based on Bragg's law. Equation 2.11 gives the path difference Δs between two parallel incident beams:

$$\Delta s = \Delta s_1 - \Delta s_2 = d(\sin\theta_2 - \sin\theta_1) \tag{2.11}$$

where d is the lattice spacing, θ_1 is the angle of an incoming beam and θ_2 is the angle of the diffracted beam. Constructive interference between the diffracted beams takes place when the path difference is equal to an integer number of wavelengths n:

$$\Delta s = d(\sin\theta_2 - \sin\theta_1) = n\,\lambda \tag{2.12}$$

hence if the incident beam angle θ_1 and diffracted beam angle θ_2 are known, and n=1, the atomic separation d can be calculated and the surface structure of a crystal lattice can be determined.

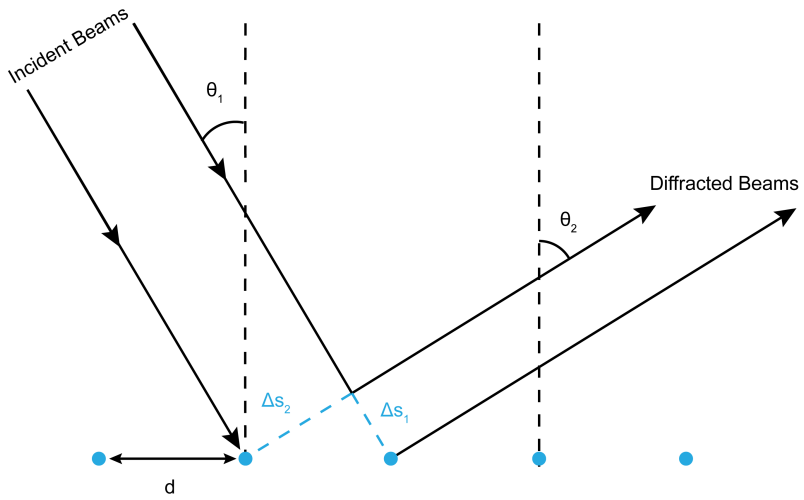

Figure 2.7 – Illustration of diffraction from a one-dimensional lattice of atoms separated by a distance d. θ_1 and θ_2 represent the angles of the incident and diffracted beams, respectively. The blue lines denote the path difference between the parallel beams.

2.3 Auger Electron Spectroscopy

Auger Electron Spectroscopy (AES) is a popular surface science technique for determining the elemental composition of surfaces. Underlying this spectroscopic technique is the Auger effect, which is based on the analysis of electrons emitted from an excited atom after a series of internal relaxation events. The Auger effect was discovered independently by both Lise Meitner [23,24] and Pierre Auger [25] in the 1920s.

The Auger effect is illustrated in figure 2.8 and occurs when an incident photon or electron causes the photoemission of a core electron, creating an electron vacancy in that level. An autoionisation process follows this, where the vacancy is filled by an electron from a level with lower binding energy (down electron) [26]. The resultant quantum of energy, equal to the difference in binding energy between the core hole and the down electron, can be removed from the atom as a photon (X-ray fluorescence) or alternatively by transfer to a third electron (Auger electron), which can then escape into the vacuum. The kinetic energy of the Auger electron E_{kin} is given by the following equation:

$$E_{kin} = E_k - E_{L_1} - E_{L_{2,3}} - \phi \tag{2.13}$$

The notation of Auger peaks is standardised and includes the letters of the levels of the three electrons involved. For instance, the Auger transition in figure 2.8 is notified as $KL_1L_{2,3}$. The kinetic energy of the Auger electrons is independent of the incident radiation energy that creates the initial core vacancy, and depends solely on the binding energies of electrons within the atom. Hence, Auger electrons may be used for elemental identification, providing the element has three or more electrons [27].

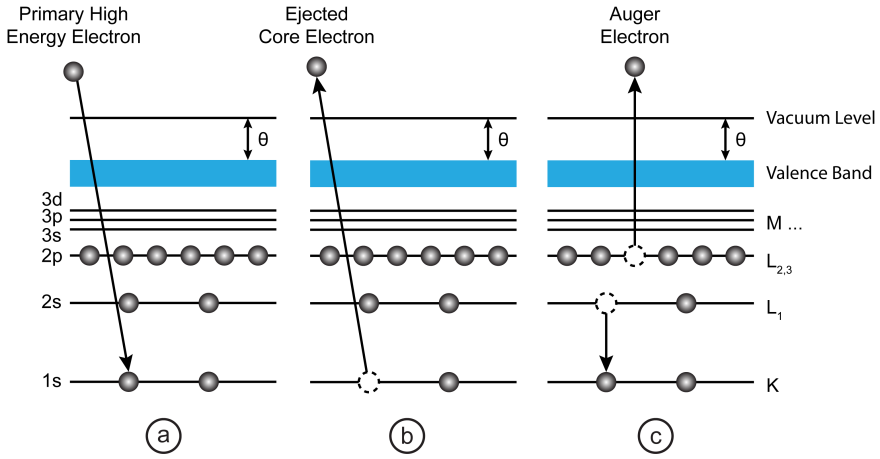

Figure 2.8 – Energy level diagram of the Auger process displaying a) the initial ground state, b) the electron transitions, and c) the final state. In AES a primary high-energy electron causes the emission of a core electron. The core level hole is then filled by an electron from a higher level, resulting in the emission of an Auger electron.

2.4 X-ray Photoelectron Spectroscopy

X-ray photoelectron spectroscopy (XPS), also termed electron spectroscopy for chemical analysis (ESCA), is a widely used surface analysis method due to its relative simplicity in use and data interpretation. The origins of XPS date back to 1887, when Hertz first observed the

photoelectric effect [28]. Thereafter, major contributions from Moseley [29,30], Robinson [31,32], Rutherford [33], Rawlinson [34], Einstein [35], de Broglie [17] and Siegbahn [36,37], amongst others, established XPS as one of the most important techniques in surface science.

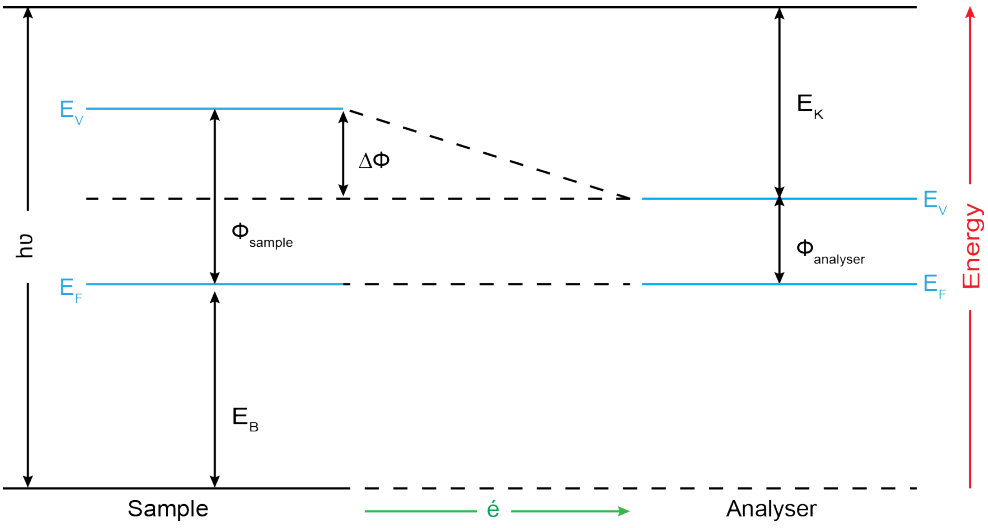

Figure 2.9 – Energy level diagram exhibiting the relationship between photon energy hv, binding energy E_B, kinetic energy E_K, and workfunction ϕ in XPS.

A standard XPS experiment involves the irradiation of a sample with photons of a known energy from an X-ray source. Different types of X-ray sources can be used: synchrotron sources for variable photon energies, or fixed X-ray sources including Mg K_α (1253.6 eV, linewidth 0.70 eV) and Al K_α (1486.6 eV, linewidth 0.85 eV). The photoemitted electrons generated close to the sample surface, i.e. up to 100 Å, are detected in an energy analyser, which scans across a certain energy range to produce a spectrum where intensity (counts per second) is plotted as a function of the binding energy.

The kinetic energy E_K of a photoelectron is schematically derived from the energy level scheme shown in figure 2.9. An X-ray with characteristic energy hv transfers its energy to a core level electron with binding energy E_B, resulting in the ejection of that core level electron. The conducting sample is in electrical contact with the analyser, allowing for the establishment of a

common reference for measuring electron energy, the Fermi level. The relation between the various energies thus can be written as:

$$E_B = h\nu - \phi_{sample} + \Delta\phi - E_K \tag{2.14}$$

where ϕ_{sample} represents the workfunction of the sample. The contact potential $\Delta\phi$ is defined as the difference between the work function of the sample ϕ_{sample} and that of the analyser $\phi_{analyser}$:

$$\Delta\phi = \phi_{sample} - \phi_{analyser} \tag{2.15}$$

As a result, the sample work function ϕ_{sample} cancels out, and as the photoelectron energy $h\nu$ and the analyser workfuntion $\phi_{analyser}$ are known, the kinetic energy E_K determines the binding energy E_B and vice versa:

$$E_B = h\nu - \phi_{analyser} - E_K \tag{2.16}$$

The workfunction of the analyser $\phi_{analyser}$ can be determined by performing an energy calibration. This is achieved by adjusting the energy scale to zero at the Fermi level of a reference sample, for example silver (Ag) or gold (Au). Henceforth, the analyser workfuntion $\phi_{analyser}$ is zero and the binding E_B and kinetic energy E_K are directly related through equation 2.17,

$$E_K = h\nu - E_B \tag{2.17}$$

This is only valid for conductive samples where the Fermi level of the sample and the analyser are equal. In the case of insulating or semi-conducting samples that are prone to charging, the Fermi level is not well defined and a shift of the energy scale may occur.

2.4.1 Spectral Features

Figure 2.10 displays a typical XPS wide scan spectrum of rutile TiO_2(110) recorded using synchrotron radiation. A number of peaks are visible in the spectrum, which appear superimposed on a background that increases towards high binding energy with step-like increases on the high binding energy side of each significant peak. The step-like appearence of the photoelectron peaks is due to inelastic collisions of the photoelectrons upon leaving the sample. The background is made up of contributions from secondary electrons on the high binding energy side of the spectrum, while Bremsstrahlung radiation dominates the low binding energy side. The peaks observed in the spectrum can be grouped into three types: peaks due to X-ray excited Auger emission, photoemission from core levels, and photoemission from valence bands.

The most narrow and intense peaks are characteristic of core levels and are a direct representation of the electronic structure of the sample. Doublet core level peaks, such as the Ti *2p* at a binding energy of 458.5 eV, arise through spin-orbit coupling. The peak width ΔE is a convolution of several contributions, as shown in equation 2.18:

$$\Delta E = \sqrt{\Delta E_n^2 + \Delta E_p^2 + \Delta E_a^2} \tag{2.18}$$

where ΔE_n is the inherent width of the core level, ΔE_p is the width of the excitation source and ΔE_a is the resolution of the analyser. Appropriate fitting of XPS data requires the selection of a

correct line shape for the photoelectron peaks and background. The natural line shape of the peaks depends on the composition of the material, i.e. insulators, semiconductors and metals with low electron state densities around the Fermi level exhibit a Lorentzian natural line shape, whereas in the case of metals with high electron density around the Fermi level a Doniach-Sunjic (D-S) line shape is more appropriate. Although the original line shapes are simply Lorentzian or D-S type, experimental data must also be convoluted with an additional Gaussian function to account for the analyser resolution [38]. Moreover, backgrounds are customarily fit using either a linear, Shirley [39] or Tougaard model [40].

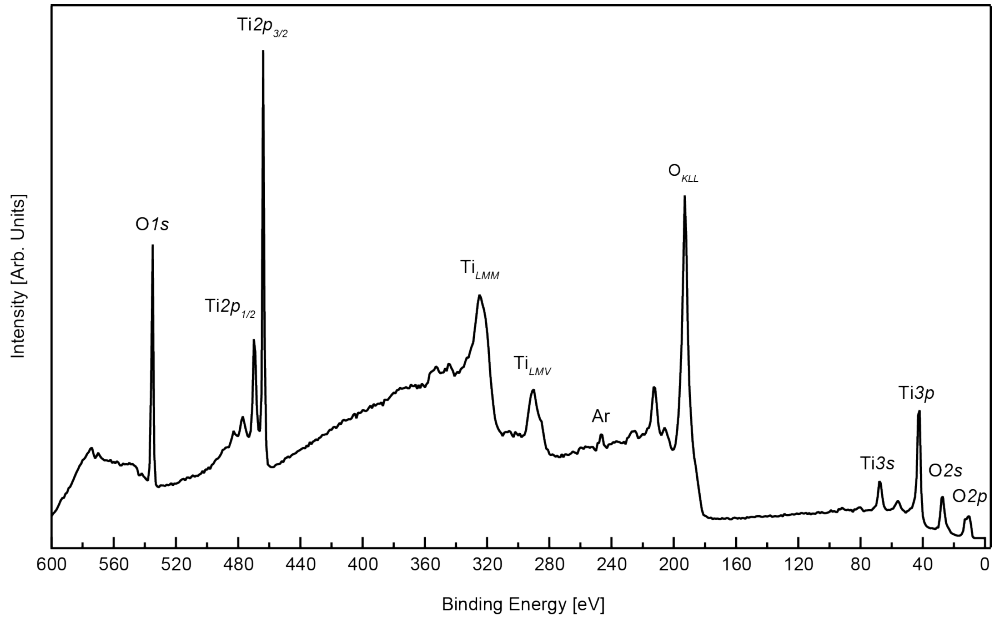

Figure 2.10 – XPS widescan of a rutile TiO_2(110) sample with the Auger and XPS peaks identified ($h\nu$ = 700 eV).

The valence band is comprised of electrons involved in de-localised or bonding orbitals, with binding energies between roughly 0 and 20 eV. The levels in this region are very closely spaced resulting in a band structure. The appearance of the valence band is heavily dependent on the nature of the material; in conducting materials the occupied valence band overlaps the empty conduction band, whilst in insulating materials these are separated by a band gap. The intensity of the valence band is generally much lower than that of the core levels owing to the small photoionisation cross-section of the valence level electrons. Therefore, this region is best

probed using low-energy photon sources, such as those applied in ultraviolet photoelectron spectroscopy (UPS), or variable energy sources such as synchrotron radiation [26].

2.4.2 Initial and Final State Effects

The binding energy E_B of a photoelectron is equal to the difference between the energy of the initial and final atomic states, i.e. the energy difference of the atom with *n* and *n-1* electrons,

$$E_B = E_f(n-1) - E_i(n) \tag{2.19}$$

where $E_f(n-1)$ is the final state energy and $E_i(n)$ is the initial state energy. If no rearrangement of the electronic structure were to occur, the binding energy would be simply equal to the negative orbital energy of the initial state of the electron $-\varepsilon_k$,

$$E_B \backsimeq -\varepsilon_k \tag{2.20}$$

which is an approximation of Koopmans' theorem [41]. However, when a photoelectron is ejected, the remaining electrons relax and the energy of the final state is reduced. Additionally, if the atom is located in a solid material, relaxation of the electrons of neighbouring atoms can occur in response to the ionisation even. The one electron theory of equation 2.20 also neglects electron correlation and relativistic effects, both of which tend to increase the binding energy of the electron. Taking this into account, a more accurate expression for the binding energy E_B is given by equation 2.21 [42]:

$$E_B = -\varepsilon_k - \delta\varepsilon_{relax} + \delta\varepsilon_{rel} + \delta\varepsilon_{corr} \tag{2.21}$$

From equation 2.21 it is clear that both initial and final states contribute to the binding energy. The initial state refers to the ground state of an atom prior to photoemission. A chemical shift is an initial state effect, whereby an energetic shift arises due to chemical bonding. The extent of shift depends on the oxidation state of the atom, i.e. the binding energy increases in accordance with the oxidation state.

Final state features are evidenced by the appearance of satellite peaks, and result from relaxation energy generated by the photoemitted electron. This relaxation energy can either excite valence electrons to a higher unfilled state (shake-up) or to an unbound continuum state (shake-off). Another final state effect is the spin-orbit splitting of any *p*, *d* or *f* state, which can occur when the system has unpaired electrons in the valence levels. In accordance with the LS coupling scheme the total angular momentum j is given by the sum of the spin angular momentum s and the orbital angular momentum ℓ. Any state with an orbital angular momentum $\ell > 0$ and one unpaired electron gives rise to a doublet, corresponding to $j = |\ell \pm 1/2|$.

2.4.3 Resonance Photoemission Spectroscopy

Resonant photoemission was discovered by Guillot *et al*. in 1977, where it was observed that for energies near the *3p* edge of nickel, there was a strong resonance enhancement of a weak valence band structure about 6 eV below the Fermi level [43]. The angular-momentum selection rule for electronic transitions stipulates that $\ell \longrightarrow (\ell \pm 1)$. Resonance is typically observed when the final state of the electronic transition is associated with a partially filled inner atomic shell, e.g. $3p \longrightarrow 3d$ (transition metals), $4d \longrightarrow 4f$ (rare earths), and $5d \longrightarrow 5f$ (actinides). Resonance photoemission spectroscopy (RESPES) is based on the quantum-mechanical interference between two different excitation processes that ultimately yield the

same final state. In the case of a transition metal, the direct photoemission process produces an electron with kinetic energy E:

$$3p^6 3d^n + h\nu \longrightarrow 3p^6 3d^{n-1} + e^-(E) \tag{2.22}$$

Simultaneously, optical adsorption may also lead to excitation of an electron from the *3p* to the *3d* level,

$$3p^6 3d^n + h\nu \longrightarrow [3p^6 3d^{n+1}]^* \tag{2.23}$$

The excited state then decays in an Auger-like process, in which the core hole is filled by one electron and a second electron is emitted to produce a final state identical to the direct photoemission process,

$$[3p^6 3d^{n+1}]^* \longrightarrow 3p^6 3d^{n-1} + e^-(E) \tag{2.24}$$

Since the initial and final states in equations (2.22) and, (2.23) (2.24) are the same, constructive interference between the two channels occurs, appearing as an enhancement of photoemission peaks in the spectra. The resonant peaks display an asymmetric lineshape, known as a Fano lineshape, which is defined by equation 2.25:

$$f(\varepsilon) = \frac{(q+\varepsilon)^2}{1+\varepsilon^2} = 1 + \frac{q^2 - 1 + 2q\varepsilon}{1+\varepsilon^2} \tag{2.25}$$

where q is referred to as the lineshape parameter, which is a transition probability function, and ε is the reduced energy variable given by equation 2.26:

$$\varepsilon = \frac{E - E_\phi - F(E)}{\pi |V_E|} \tag{2.26}$$

where ϕ is the intermediate state with a core hole (equation 2.23), V_E is the Auger matrix element for the second step of the process (equation 2.24), and $F(E)$ is a self-energy arising from the interaction with the continuum that causes the state ϕ to be shifted from E_ϕ:

$$F(E) = P \int \frac{|V_E|^2}{E - E'} \tag{2.27}$$

where P is the principal value. Examples of the asymmetric Fano lineshape are shown in figure 2.11 for various values of q [44].

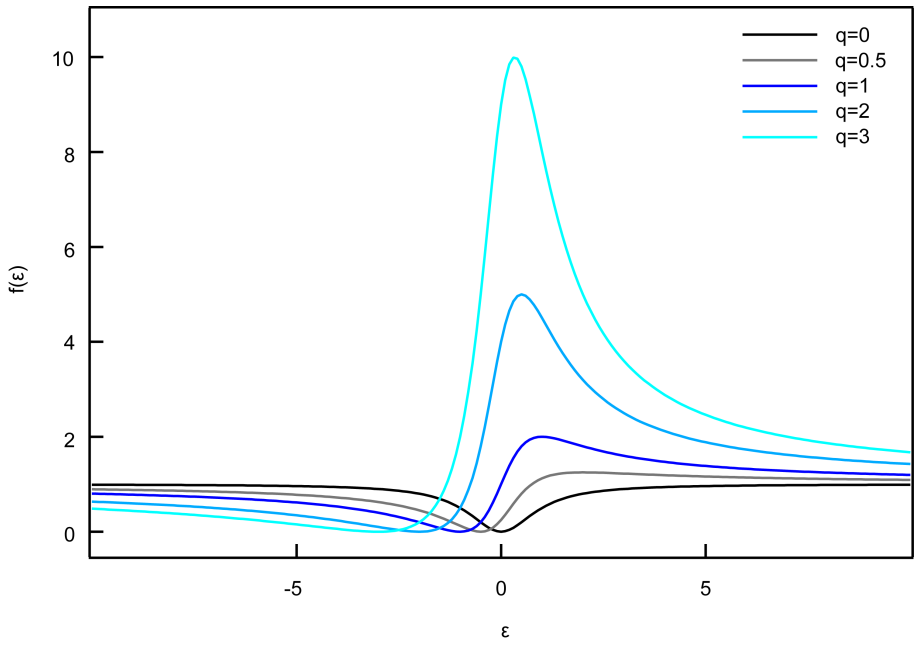

Figure 2.11 – Fano lineshapes for several values of the lineshape parameter q.

2.5 Photoemission Electron Microscopy

Photoemission electron microscopes record a full-field image of a surface based on the spatial distribution of emitted photoelectrons. The invention of photoemission electron microscopy (PEEM) dates back to 1933 when Brüche used ultraviolet light from a mercury lamp to image photoelectrons emitted from a metal sample [45]. X-ray photoemission electron microscopy (XPEEM), where X-rays are used as the excitation source, was developed by Tonner and Harp in 1988 [46]. In 1993, Stöhr *et al*. demonstrated the magnetic contrast capability of XPEEM by imaging magnetic domains at high resolution [47].

The illumination of a sample with X-rays excites a very broad spectrum of electrons, which confers on XPEEM the capability to perform laterally resolved versions of some of the most fundamental X-ray spectroscopies, namely X-ray electron emission spectroscopies such as X-ray photoelectron spectroscopy (XPS) and Auger electron spectroscopy, and X-ray adsorption spectroscopy (XAS). The contrast in XPEEM is generated by lateral variations in the X-ray absorption cross-section. Since the absorption of X-rays in matter in an energy-dependent process, X-ray absorption spectroscopy (XAS) is a powerful technique for investigating elemental, chemical and magnetic properties of samples, when tuneable synchrotron radiation is used as the excitation source.

The measurement of X-ray adsorption can be performed in transmission or total electron yield mode, as illustrated in figure 2.12. The transmission technique requires a sufficiently thin sample that allows the transmission of the incident X-rays, while the total electron yield (TEY) mode can be employed for conventional samples; the latter is the one applied in XPEEM. Contrary to the transmission mode, the absorbed X-ray intensity is not measured directly in TEY mode, rather the photocurrent generated by the absorbed X-rays. When photons are absorbed by the sample, core holes are created that are filled by Auger electron emission. On

the way to the surface, Auger processes and inelastic electron scattering generate a plethora of low energy electrons through inelastic scattering processes. The total number of emitted photoelectrons is then directly proportional to the number of absorbed photons in a near surface region of the sample [48, 49].

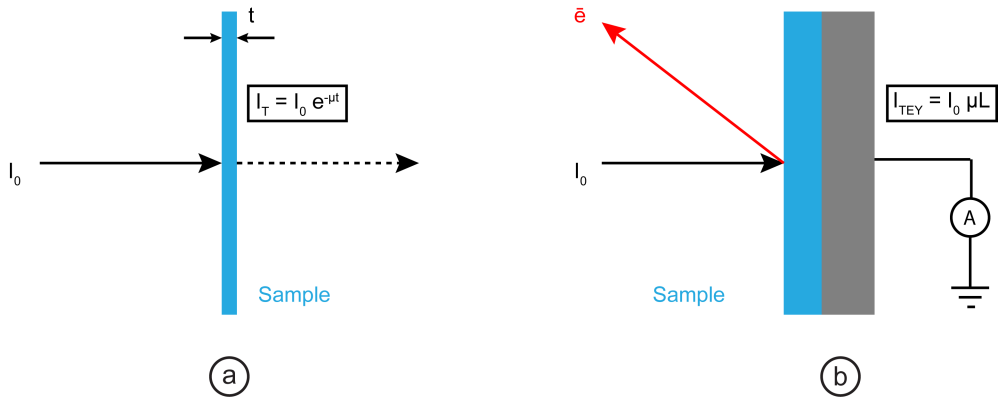

Figure 2.12 – Diagram of the two common methods of recording X-ray absorption spectra a) transmission mode and b) the total electron yield mode, where μ represents the absorption coefficient, t the sample thickness, L the electron sampling depth, and I_0 the intensity of the incident X-ray beam.

The absorption process is heavily dependent on the polarisation of the photons used. In optics this is known as *dichroism*, though when deriving from preferential spin alignment or magnetic order the appropriate designation is *magnetic dichroism*. This is the foundation for two special imaging modes of XAS: X-ray magnetic circular dichroism (XMCD) and X-ray magnetic linear dichroism (XMLD).

XMLD was first predicted by Thole *et al*. in 1985 for the $M_{4,5}$ edges of rare earth materials [50]. However, experimental evidence of the effect was only acquired one year later, by van der Laan *et al*. [51]. XMLD is utilised in the characterisation of ferromagnetic and especially antiferromagnetic materials, which cannot be studied by many techniques because of their compensated spin structure. In the paramagnetic state these materials have a spherically symmetric core and valence density charge. However when they are in a magnetic state with collinear spin alignment, the spin-orbit coupling may result in an elliptical deformation of the

charge. This charge distortion is uniaxially symmetric about the spin direction, thus the X-ray absorption intensity will differ for E aligned parallel and perpendicular to the spin direction. The intensity of the XMLD effect has a $cos^2\theta$ dependence and is proportional to,

$$I_{XMLD} \sim (1 - 3cos^2\theta)\langle M^2\rangle_T \tag{2.28}$$

where $\langle M^2\rangle_T$ reflects the temperature dependence of the long range magnetic order, and θ is the angle between the linear electric field vector E and the orientation of the magnetisation axis [49, 52]. The use of circularly polarised photons renders the absorption process spin dependent, thus the intensity difference of spectra acquired in this manner corresponds to the difference between the number of spin-up and spin-down holes, i.e. the magnetic moment. This is the basis for X-ray magnetic circular dichroism, which was theoretically predicted in 1975 by Erskine and Stern for the $M_{2,3}$-edges of nickel [53], with the first experimental observation of the effect in 1983 by Schütz et *al*. at the K-edge of metallic iron [54].

The essence of XMCD can be explained using a two-step process in a simple one-electron model. The first step in the X-ray absorption process involves the creation of a net spin polarisation through the transfer of the angular momentum of the incident circularly polarised photons to the photoelectrons excited from a core level, obeying the conservation of angular momentum principle. Assuming the photoelectron is excited from a spin-orbit split level, e.g. $2p_{3/2}$ (L_3 edge), the angular momentum of the photon can be transferred in part to the spin of the photoelectron due to spin-orbit coupling, consequently the excited photoelectrons are spin-polarised. Right circularly polarised photons transfer the opposite momentum to the electron than left circularly polarised photons, thus photoelectrons with opposite spins are created in the two cases. Since the $2p_{3/2}$ (L_3) and $2p_{1/2}$ (L_2) levels have opposite spin-orbit coupling ($\ell + s$ and $\ell - s$, respectively), the spin polarisation will be opposite at both edges. In the second step of the process, the photoelectrons are excited to the spin-split valence band composed of

different spin-up and spin-down populations, which acts as a detector for the spin of the photoelectrons. The maximum dichroism effect is obtained when the magnetisation direction is aligned with the photon spin direction. As illustrated in figure 2.13, the difference spectra of the white line intensities recorded with right and left circular polarisation are designated as A and B, for the L_3- and L_2-edge, respectively. The integrals over the spin-orbit split edges may be defined as:

$$A = \int_{L_3} (\mu^+ - \mu^-)\, dE \tag{2.29}$$

$$B = \int_{L_2} (\mu^+ - \mu^-) dE \tag{2.30}$$

The sum rules relate the measured polarisation dependent X-ray absorption intensities with certain valence band properties, specifically the number of holes per atom N, the spin magnetic moment per atom m_s and the orbital magnetic moment per atom m_o. In conventional X-ray absorption spectroscopy, the number of empty valence states for the L-edge in a *3d* transition metal can be determined through the *charge sum rule*, which relates the measured averaged peak intensity to the number of empty states N per atom, as shown in equation 2.31:

$$\langle I_{L_3} + I_{L_2} \rangle = CN \tag{2.31}$$

where C is the square of the $p \longrightarrow d$ radial transition matrix and has a value of about 10 Mb eV [55]. The *spin sum rule* relates the angle averaged dichroism intensities, A and B in figure 2.13, with the magnitude of the spin magnetic moment m_s per atom according to equation 2.32:

$$\langle A - 2B \rangle = -\frac{C}{\mu_B} m_s \tag{2.32}$$

where the constant C is the same as in the charge sum rule and μ_B is the Bohr magneton. The orbital moment m_o is determined by use of the *orbital sum rule*, which links the angle averaged dichroism intensities with the size of the average orbital moment per atom, as shown in equation 2.33:

$$\langle A + B \rangle = -\frac{3C}{2\mu_B} m_o \tag{2.33}$$

where C and μ_B are as before. The sum rules for the orbital and spin moment were derived by Thole *et al*. in 1992 and Carra *et al*. in 1993, respectively [56, 57].

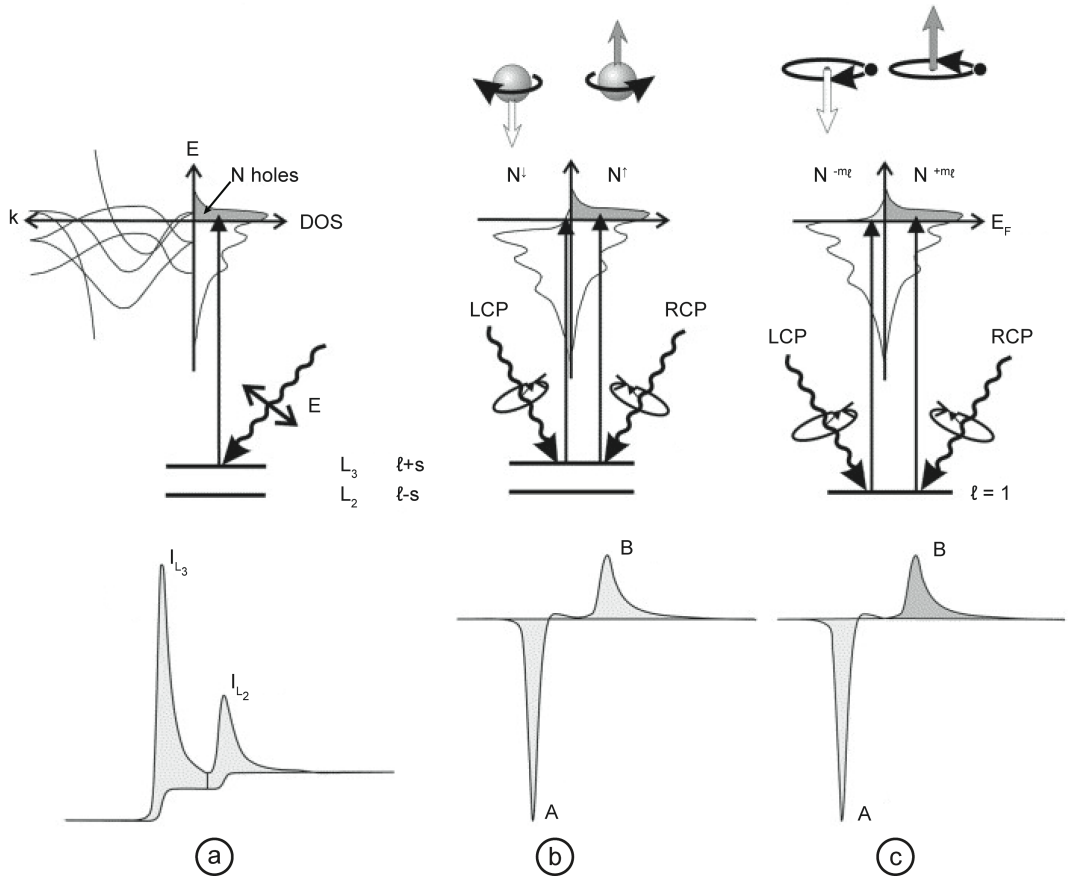

Figure 2.13 – Schematic of the electronic transitions in a) conventional L-edge X-ray absorption, b) and c) X-ray magnetic circular dichroism, in a one-electron model. The illustrated transitions are from the spin-orbit split *2p* core shell to empty conduction band states above the Fermi level. In conventional X-ray absorption the intensity of the two peaks, I_{L_3} and I_{L_2}, is proportional to the number N of d holes. The use of circularly polarised light allows b) the spin moment, and c) the orbital moment to be determined through the dichroic difference intensities A and B, according to the sum rules. Adapted from [49].

2.6 Low Energy Electron Microscopy

Low energy electron microscopy (LEEM) was invented by Bauer in 1962 [58]. Since then it has developed into one of the leading techniques for *in situ* studies of surface structure, morphology, magnetism and dynamic processes [59]. LEEM is classified as a type of cathode lens electron microscopy, whereby the sample is utilised as a cathode element. LEEM images are formed using low-energy electrons that are reflected from the sample without energy loss, i.e. elastically backscattered electrons. In crystalline materials, elastic backscattering of a coherent electron beam results in diffraction. Consequently, LEEM is a diffraction based imaging technique, intimately related to LEED, which can provide information on complementary real and reciprocal space.

The image and diffraction pattern are formed as follows. In the first instance, electrons generated by a cathode in the electron gun are accelerated to the microscope potential, typically between 15 and 20 keV. The electron beam is focused by the illumination optics to a crossover point in the back of the focal plane of the objective lens. Subsequently, the beam is deflected by a magnetic sector field onto the optical axis of the objective lens, at normal sample incidence. The objective lens acts simultaneously on the incident and reflected beams; it focuses the beam to infinity and decelerates it to the desired incident energy, given by a variable voltage bias between the electron gun cathode and the sample. The reflected electrons are then reaccelerated to the microscope potential and refocused by the objective. In the case of crystalline samples, electron reflection is confined to specific Bragg angles by diffraction. The objective lens focuses electrons that are emitted from the sample at the same angle to the same point in the back focal plane, producing a diffraction pattern. After emerging from the objective lens, the reflected electrons are deflected by the sector field into the imaging column and an image is formed through selection of one of the diffracted beams using a contrast aperture in the diffraction plane.

Several contrast mechanisms can be exploited in LEEM that derive from the amplitude and phase of the imaging electron wave. Amplitude contrast is the most common contrast mechanism in LEEM, and originates from sample features with different reflection coefficients, resulting in a spatial variation of the amplitude of the elastically reflected wave. Phase contrast appears due to modifications of the phase of the imaging electron wave upon interaction with a surface that results in interference effects. Examples of phase contrast include step contrast and quantum size contrast. Step contrast arises due to the interference of the reflected electron waves that originate from terraces either side of the step. The phase shift is given by equation 2.34:

$$\phi = kd = \frac{2\pi}{\lambda} 2a_0 \tag{2.34}$$

where d is the path length difference between waves that are reflected from terraces on the opposite sides of a step, a_0 is the step height and λ is the wavelength of the backscattered electrons. Quantum contrast is associated with the quantum size effect (QSE) in electron reflectivity, which may occur in the presence of a thin film. The QSE in electron reflectivity is caused by the interference between the wave that is reflected from the surface of a film and from the interface between the film and the substrate. The interference arises due to a difference in path length for the two waves, which leads to a phase shift between the waves [60].

The aforementioned contrast mechanisms are enhanced by magnetic contrast when spin polarised electrons are used to illuminate the surface, in which case the technique is known as spin-polarised LEEM, or SPLEEM. Under the conventional condition of normal incidence of the incident and reflected beams, the magnetic contrast in SPLEEM is dominated by the exchange interaction. The magnetic contrast stems from the asymmetry A of the reflected intensities for oppositely polarised light, termed spin-up $I_{\uparrow}$ and spin-down $I_{\downarrow}$:

$$A = \frac{1}{P}\frac{I_{\uparrow} - I_{\downarrow}}{I_{\uparrow} + I_{\downarrow}} \tag{2.35}$$

where P is the degree of spin polarisation of the incident beam. Subtraction of the spin-up and spin-down images in the numerator eliminates features that do not originate exclusively in the magnetisation of the sample, such as topographical image features that are found in conventional LEEM. Division by the spin-up and spin-down image sum yields an image in which intensities are proportional to $1/P$ and the component of the local magnetisation vector that coincides with the incident beam polarisation direction [59]. The electron source in LEEM is often a LaB_6 filament, as in many other electron microscopes. However, SPLEEM requires spin polarised electrons, as such the LaB_6 filament is replaced with a spin gun. The spin gun is composed of a spin polarised electron source that produces spin polarised electrons, and a spin manipulator that permits accurate control of the spin polarisation vector. Modern spin guns are capable of producing electron beams with a spin polarisation of 90% and a brightness of $1.3\times10^{7} A.cm^{-2}.sr^{-1}$ [61].

References

[1] G. Binnig, H. Rohrer, C. Gerber, and E. Weibel, Appl. Phys. Lett. **40**, 178 (1982).

[2] G. Binnig, H. Rohrer, C. Gerber, and E. Weibel, Phys. Rev. Lett. **49**, 57 (1982).

[3] F. Chiaravalloti, D. Riedel, G. Dujardin, and H. P. Pinto, Phys. Rev. B **79**, 245431 (2009).

[4] R. Wiesendanger, *Scanning Probe Microscopy and Spectroscopy* (Cambridge University Press, 1994).

[5] D. M. Eigler and E. K. Schweizer, Nature **344**, 524 (1990).

[6] D. A. Bonnell, *Scanning Tunneling Microscopy and Spectroscopy: Theory, Techniques and Applications* (VCH Publishers, 1993).

[7] J. Tersoff and D. R. Hamann, Phys. Rev. Lett. **50**, 1998 (1983).

[8] J. Tersoff and D. Hamann, Phys. Rev., B Condens. Matter **31**, 805 (1985).

[9] C. Chen, Phys. Rev. Lett. **65**, 448 (1990).

[10] N. Lang, Phys. Rev. Lett. **55**, 230 (1985).

[11] N. Lang, Phys. Rev. Lett. **56**, 1164 (1986).

[12] N. Lang, Phys. Rev., B Condens. Matter **34**, 5947 (1986).

[13] R. J. Hamers, Annu. Rev. Phys. Chem. **40**, 531 (1989).

[14] J. Bardeen, Phys Rev Letters **6**, 57 (1961).

[15] J. Wintterlin, J. Wiechers, H. Brune, T. Gritsch, H. Höfer, and R. Behm, Phys. Rev. Lett. **62**, 59 (1989).

[16] N. Nilius, Surf Sci Rep **64**, 595 (2009).

[17] L. de Broglie, Nature **112**, 540 (1923).

[18] C. Davisson and L. H. Germer, Physical Review **30**, 705 (1927).

[19] G. P. Thomson and A. Reid, Nature **119**, 890 (1927).

[20] K. Oura, V. G. Lifshits, A. Saranin, A. V. Zotov, and M. Katayama, *Surface Science* (Springer Science & Business Media, 2003).

[21] D. P. Woodruff and T. A. Delchar, *Modern Techniques of Surface Science*, Cambridge University Press (Cambridge University Press, 1994).

[22] A. Zangwill, *Physics at Surfaces* (Cambridge University Press, 1988).

[23] L. Meitner, Z. Physik **17**, 54 (1923).

[24] L. Meitner, Z. Physik **19**, 307 (1923).

[25] P. Auger, J. Phys. Radium **6**, 205 (1925).

[26] D. Briggs and M. P. Seah, *Practical Surface Analysis*, Second (John Willey & Sons, 1990).

[27] G. Attard and C. Barnes, *Surfaces* (Oxford University Press, 1998).

[28] H. Hertz, Ann. Phys. **267**, 983 (1887).

[29] H. Moseley, Philosophical Magazine **26**, 1024 (1913).

[30] H. Moseley, Philosophical Magazine **28**, 703 (1914).

[31] H. Robinson and W. F. Rawlinson, Philosophical Magazine **28**, 277 (1914).

[32] H. R. Robinson, Philosophical Magazine **50**, 241 (1925).

[33] E. Rutherford, H. Robinson, and W. F. Rawlinson, Philosophical Magazine **28**, 281 (1914).

[34] W. F. Rawlinson, Philosophical Magazine **28**, 274 (1914).

[35] A. Einstein, Ann. Phys. **323**, 639 (1905).

[36] E. Sokolowski, C. Nordling, and K. Siegbahn, Arkiv Fysik **12**, 301 (1957).

[37] C. Nordling, E. Sokolowski, and K. Siegbahn, Physical Review **105**, 1676 (1957).

[38] S. Hofmann, *Auger- and X-Ray Photoelectron Spectroscopy in Materials Science: a User-Oriented Guide* (Springer Berlin Heidelberg, 2012).

[39] D. A. Shirley, Phys. Rev. B **5**, 4709 (1972).

[40] S. Tougaard, Phys. Rev. B **34**, 6779 (1986).

[41] T. Koopmans, Physica **1**, 104 (1934).

[42] K. W. Kolasinski, *Surface Science* (John Wiley & Sons, 2008).

[43] C. Guillot, Y. Ballu, J. Paigné, J. Lecante, and K. P. Jain, Phys. Rev. Lett. **39**, 1632 (1977).

[44] R. Z. Bachrach, *Synchrotron Radiation Research: Advances in Surface and Interface Science Techniques* (Springer US, 2012).

[45] E. Z. Bruche, Z Phys **86**, 48 (1933).

[46] B. P. Tonner and G. R. Harp, Rev. Sci. Instrum. **59**, 853 (1988).

[47] J. Stöhr, Y. Wu, B. D. Hermsmeier, M. G. Samant, G. R. Harp, S. Koranda, D. Dunham, and B. P. Tonner, Science **259**, 658 (1993).

[48] P. Hawkes and J. C. H. Spence, *Science of Microscopy* (Springer Science & Business

Media, 2008).

[49] J. Stöhr and H. C. Siegmann, *Magnetism* (Springer Berlin Heidelberg, Berlin, Heidelberg, 2006).

[50] B. Thole, G. van der Laan, and G. Sawatzky, Phys. Rev. Lett. **55**, 2086 (1985).

[51] G. van der Laan, B. Thole, G. Sawatzky, J. Goedkoop, J. Fuggle, J. Esteva, R. Karnatak, J. Remeika, and H. Dabkowska, Phys. Rev., B Condens. Matter **34**, 6529 (1986).

[52] H. Hopster and H. P. Oepen, *Magnetic Microscopy of Nanostructures* (Springer Science & Business Media, 2006).

[53] J. L. Erskine and E. A. Stern, Phys. Rev. B **12**, 5016 (1975).

[54] G. Schutz, W. Wagner, W. Wilhelm, P. Kienle, and R. Zeller, Physical Review **58**, 737 (1987).

[55] J. Stöhr and R. Nakajima, IBM Journal of Research and Development **42**, 73 (1998).

[56] B. Thole, P. Carra, F. Sette, and G. van der Laan, Phys. Rev. Lett. **68**, 1943 (1992).

[57] P. Carra, B. T. Thole, M. Altarelli, and B. Wang, Phys. Rev. Lett. **70**, 694 (1993).

[58] E. Bauer, Academic Press **1**, 11 (1962).

[59] M. S. Altman, J. Phys.: Condens. Matter **22**, 084017 (2010).

[60] N. Rougemaille and A. K. Schmid, Eur. Phys. J. Appl. Phys. **50**, 20101 (2010).

[61] M. Suzuki, M. Hashimoto, T. Yasue, T. Koshikawa, Y. Nakagawa, T. Konomi, A. Mano, N. Yamamoto, M. Kuwahara, M. Yamamoto, S. Okumi, T. Nakanishi, X. Jin, T. Ujihara, Y. Takeda, T. Kohashi, T. Ohshima, T. Saka, T. Kato, and H. Horinaka, Appl. Phys. Express **3**, 026601 (2010).

CHAPTER 3

INSTRUMENTATION

Abstract

The equipment used in any scientific experiment is of key importance to the systematic and rigorous acquisition of reliable data. This chapter will focus on the physical aspects of the instrumentation involved in each stage of the experiments.

3.1 Ultra High Vacuum

Ultra high vacuum (UHV) conditions are generally defined as pressures below 1×10^{-10} mbar. Such conditions are essential to the undertaking of all the experiments described in this thesis. The reason behind the use of such low pressures can be explained by kinetic theory, whereby an estimate of the time required to form one monolayer (ML) can be calculated. Let us define one ML as being equivalent to 1×10^{15} cm^{-2}. This means that in the case of the CO on Ag(111), monolayer coverage is reached in approximately 10 hours at a CO pressure of 1×10^{-10} mbar, assuming unity sticking probability [1]. This demonstrates the importance of such a sterile environment in order to have a reasonable time frame in which to execute the scientific studies. Moreover, the limited mean free path of electrons between collisions with gas phase molecules deems UHV conditions essential to an array of electron-based spectroscopies. The achievement of such conditions requires a complex network of specialised instrumentation, which will be discussed in this chapter.

3.2 The Scanning Probe Microscope

3.2.1 Overview

The scanning probe microscopy instrument used in the experiments was a commercial *Omicron* variable temperature scanning tunnelling microscope (VT-STM), as pictured in figure 3.1. The apparatus consists of two interconnected UHV chambers, one dedicated to sample preparation and the other to sample analysis. The Preparation Chamber houses standard sample preparation facilities, such as an ion sputter gun, a cerium doser, a sample heater and high-purity gas-line setup for the inlet of gases via high-precision leak valves such as oxygen and argon, while the Scanning Tunnelling Microscope (STM), Low Energy Electron Diffraction (LEED) and Auger Electron Spectroscopy (AES) optics are contained within the Analysis Chamber. Both chambers are equipped with Residual Gas Analysers, which allow for the verification of the purity of the

gas-lines and also of the atmosphere within each chamber. A manual gate valve located between the preparation and analysis chamber allows for the isolation of each chamber from each other; this allows sample preparation without contamination of the analysis chamber. The introduction of samples and tips is achieved without breaking vacuum due to a fast-entry load lock (FEL) attached to the preparation chamber. A schematic of the VT-STM system and auxiliary preparation and analysis instrumentation is shown in figure 3.2.

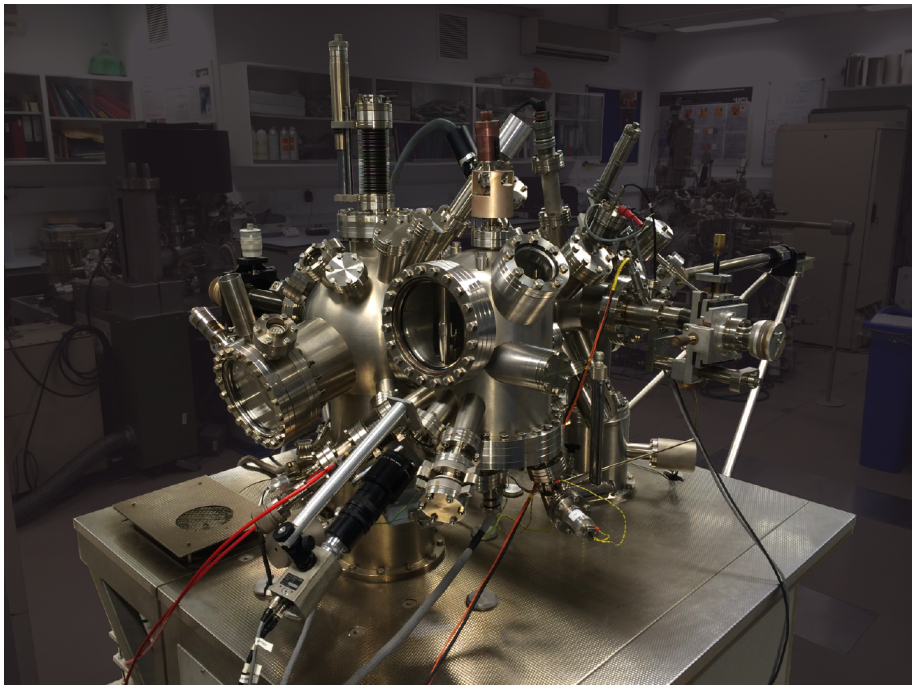

Figure 3.1 - Photograph of the *Omicron* VT-STM system.

In order to achieve UHV conditions, an intricate network of pumping devices are used to reduce the pressure inside the vacuum system. In order to handle elevated gas loads experienced during the reduction of the pressure of the system from atmospheric to around 10^{-6} mbar, the system is initially pumped by a turbo-molecular pump (attached to the preparation chamber), which in turn is backed by a rotary pump. Actual UHV conditions are attained by baking the entire system for about 24 hours at ~140 °C to remove undesirable gas molecules characterised by lower out-gassing rates which are adsorbed on the inner chamber surface, predominantly water and light hydrocarbons. After the bake has terminated, the system is cooled down to room

temperature, and ion getter pumps and titanium sublimation pumps are actuated, one of each per chamber, ultimately allowing pressures in the low 10^{-11} mbar region to be achieved. The measurement of pressures down to 10^{-2} mbar is performed by Pirani gauges; below this region the pressure is measured using Bayard-Alpert type hot-cathode ionisation gauges.

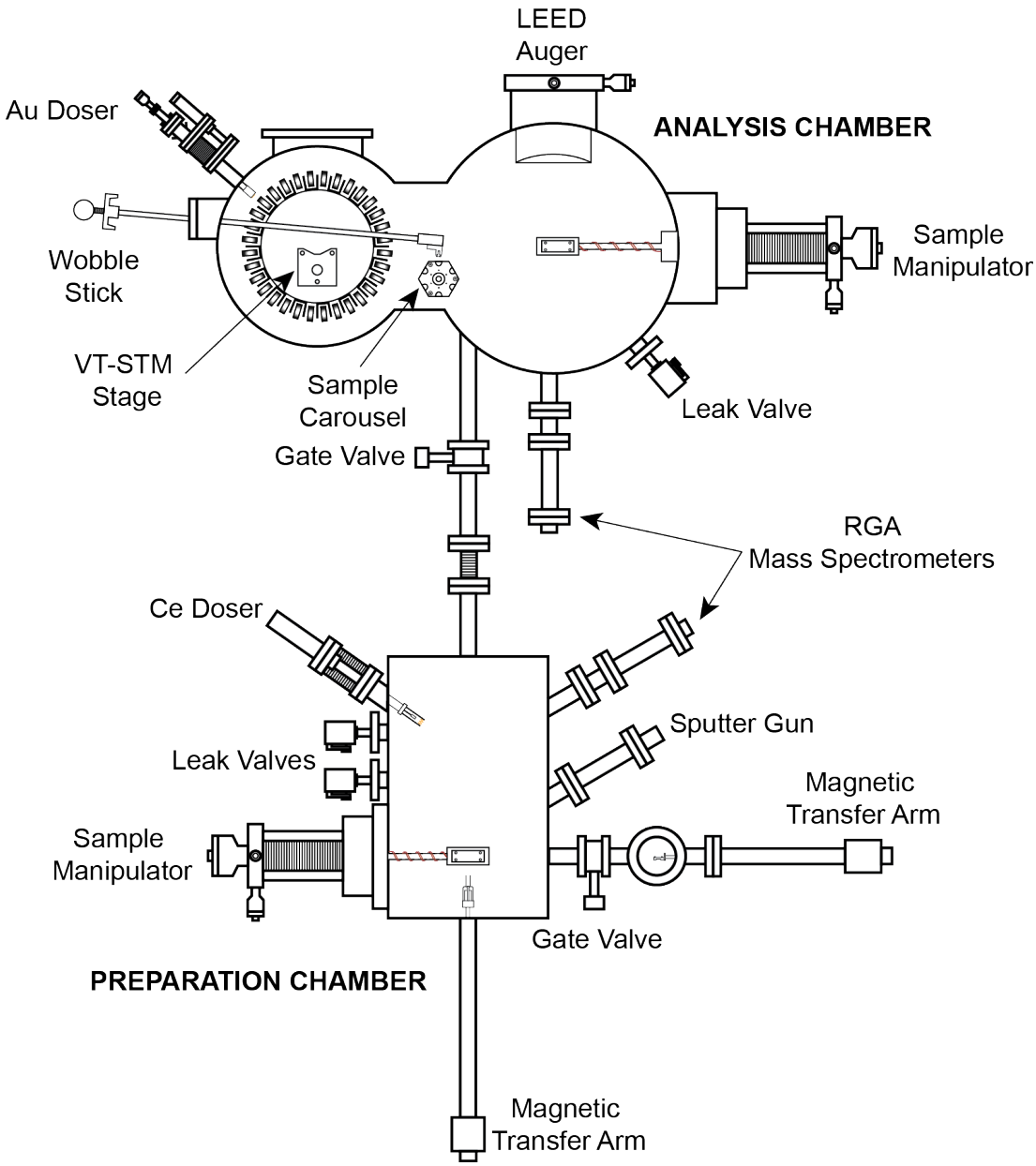

Figure 3.2 - Omicron VT-STM system overview diagram displaying the location of the principal sample preparation and analysis instruments.

3.2.2 Microscope Operation

The *Omicron* VT-STM is capable of operation at sample temperatures between 25 and 1500 K. A metal evaporator (Au) is mounted with line of sight to the sample [2]. The samples are mounted onto a tantalum plate and positioned sample-side down and above an upward facing tip on the stage, as shown in the photograph of figure 3.3. The design of the stage unit is so that the sample remains stationary while the tip is dynamic; the high precision movement of the tip is achieved by a piezoelectric drive permitting motion in the z direction (approach and retraction from the sample surface), x and y directions (rastering of the sample for image acquisition).

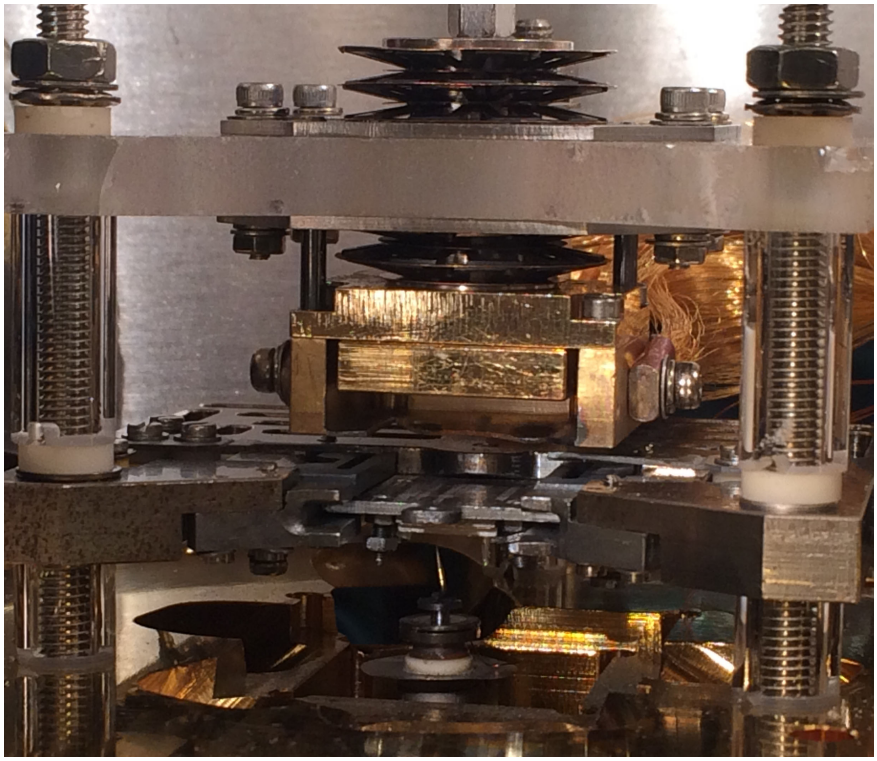

Figure 3.3 – Side-view photograph of the *Omicron* VT-STM stage where the tip is pointing upwards towards the sample.

The correct operation of the microscope requires isolation from external perturbations such as vibrations, as these can interfere with the sensitive scanning process. The source of these vibrations is varied, ranging from mechanical to electrical sources and are identified by their

characteristic frequency. To overcome this the VT-STM is housed in the basement of UCL Chemistry and an array of damping mechanisms have been integrated; the stage is suspended by vertical springs and is equipped with an eddy-current damping system through permanent magnets placed between the copper fins at the periphery of the STM stage. Additionally, the entire UHV system is mounted on *Halcyonics* platforms with active vibration isolation technology.

3.2.3 Scanning Tunnelling Microscope Modes

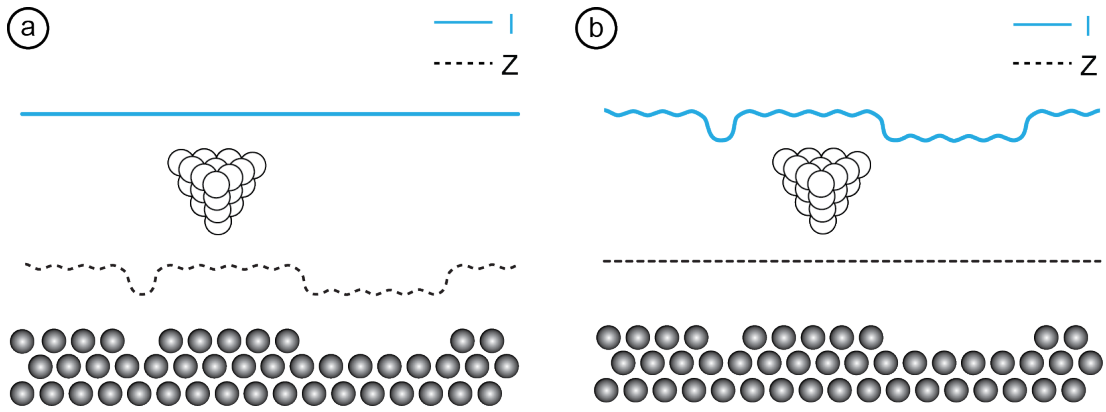

Figure 3.4 – Diagrams of the two operational modes of STM: a) Constant current mode, where the tunnelling current (I) is kept constant by adjusting the tip-sample separation (Z) during rastering of the sample. b) Constant height mode, where the tip-sample separation (Z) is kept constant and the tunnelling current (I) between the sample surface and the tip is recorded.

A scanning tunnelling microscope possesses two possible modes of operation, constant height and constant current, as displayed in figure 3.4. The constant current mode entails the adjustment of the z distance between the tip and the sample as the tip is rastered in the x and y directions across the sample in order to maintain a constant current; these adjustments are made by the z-piezo drive via a negative feedback loop mechanism. In constant height mode the opposite is performed, i.e. the tip-sample separation is maintained constant while the tunnelling current is altered to this effect. It is important to note that scanning in constant height mode is

only feasible for atomically flat surfaces as otherwise rough surfaces may result in the crashing of the tip. The recorded height or tunnelling current modifications for each point probed is then translated into a topographical image of the surface.

3.2.4 Scanning Tunnelling Microscopy Tips

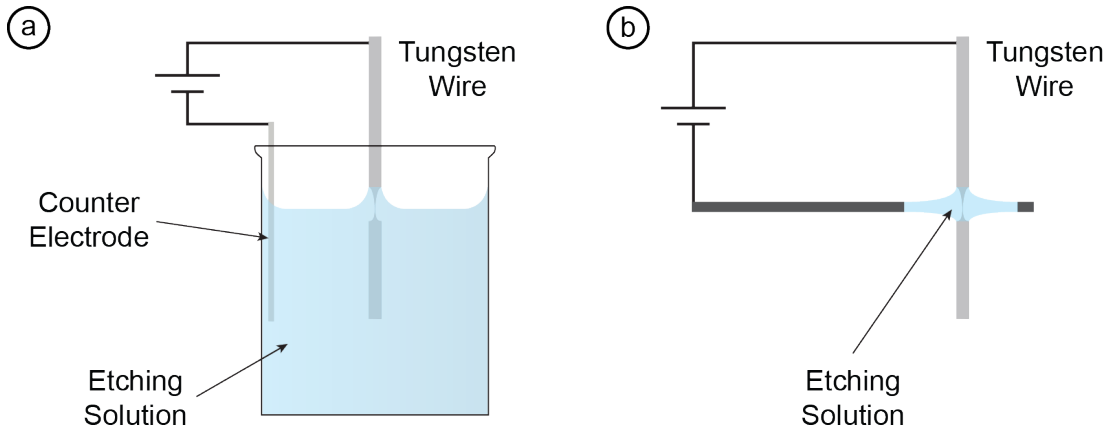

Figure 3.5 – Schematic illustrations of the two electrochemical etching methods for tip fabrication: a) the immersion method, and b) the plate method.

A stable tip with an atomically sharp apex is a prerequisite for all nanoscale scanning probe microscopy. Three types of STM tips were used throughout the course of these experiments: commercial (*Unisoku*) and manually cut platinum-iridium, and tungsten tips. The latter was produced in our laboratory by electrochemical etching of tungsten wire in an aqueous solution of 2M sodium hydroxide (NaOH) using one of the methods described in figure 3.5. After etching, the tips are observed with an optical microscope and rinsed carefully with distilled water and isopropanol prior to introduction into the UHV system, where the tips are then annealed at ~500 K to remove any remaining contaminants. It is also possible to further condition tips during the scanning process itself by performing z pulses, i.e. narrowing of the tip-sample distance, or voltage pulses, i.e. ramping of the voltage up to a maximum value of 10 V.

3.3 Sample Preparation Instruments

3.3.1 Argon Ion Sputter Gun

Ion bombardment or sputtering with inert ions, such as argon, is a common practice for the removal of surface contaminants. Argon gas is introduced into the system through a high-precision leak valve in the vicinity of the sputter gun. Located within the sputter gun is a hot tungsten filament responsible for the emission of electrons, which are accelerated towards a high voltage grid. When these electrons collide with the argon atoms, these are ionised and a beam of Ar^+ ions is produced and accelerated through various focussing elements towards the grounded sample. Impact of the Ar^+ ion beam results in the removal of atoms due to the transfer of kinetic energy, resulting in a roughened surface profile. Smoothing of the surface and removal of embedded argon ions is accomplished by annealing the sample in UHV.

3.3.2 Sample Heater and Manipulation

Samples were mounted onto *Omicron* sample plates either with spot-welded tantalum strips or bolted molybdenum clips. Magnetic transfer arms perform the manoeuvring of samples between the various chambers of the VT-STM system. In the measurement chamber, the transfer of samples and tips between the manipulator and the carousel or STM stage is achieved by using a "wobble" stick; the carousel has a storage capacity for 6 samples or tips. In each UHV chamber there is a sample manipulator with a built-in heating unit that offers 360° rotation and movement along all three axes. The sample heater works by electron bombardment, i.e. electrons are emitted from two hot tungsten filaments and accelerated towards the back of the sample holder held at a high positive bias. The sample temperature is measured using an infrared pyrometer.

3.3.3 Metal Deposition

Physical vapour deposition (PVD) was the elected method for the evaporation of metals onto the various substrates involved in the work presented in this thesis. Ultrathin films of ceria were grown on platinum (111) and rhodium (111) single crystals by the evaporation of Ce metal foil (*99.9%, Advent RM*) contained within a molybdenum crucible of a homemade electron-beam evaporator, as displayed in figure 3.6. A thoriated tungsten filament is mounted in close proximity to the crucible, and upon heating, thermionic emission occurs and the electrons are accelerated from the filament towards the crucible due to a voltage bias gradient.

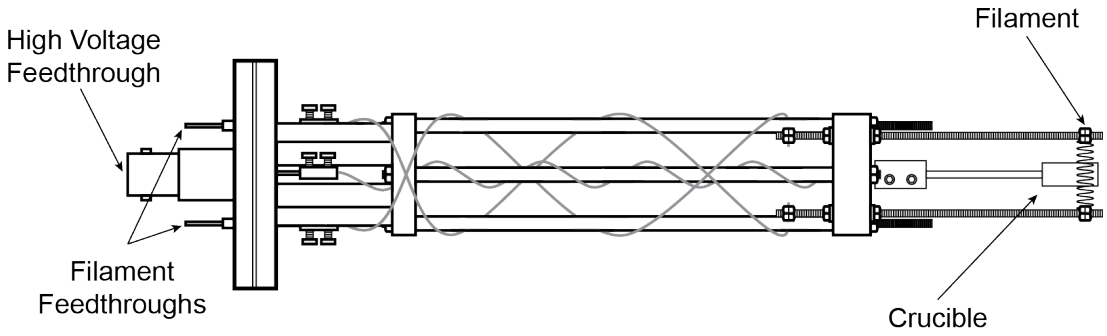

Figure 3.6 – Schematic of the homemade electron-beam evaporator used for the physical vapour deposition of cerium.

The deposition of gold nanoparticles onto the surface of the ceria ultrathin films was performed using two different commercial UHV evaporators, an *Omicron* EFM-3 and Compact Vapour Source as displayed in the schematics of figure 3.7 [3]. The EFM-3 is an e-beam type evaporator where Au wire (*99.9%, Advent RM*) is contained within molybdenum crucible. In the case of the Compact Vapour Source evaporator, Au wire is placed inside a resistively heated alumina crucible. Both evaporators possess water-cooling networks, shutter mechanisms for controlled dose times and k-type thermocouples that allow accurate readings of the crucible

temperature; the EFM-3 evaporator also has an incorporated flux monitor to regulate the metal evaporation rate.

The work concerning the formation of iron nanowires on rutile TiO_2(110) involved the use of a homemade e-beam evaporator, similar to the one used for Ce deposition, and a commercial *Omicron* EFM-3 evaporator as described above.

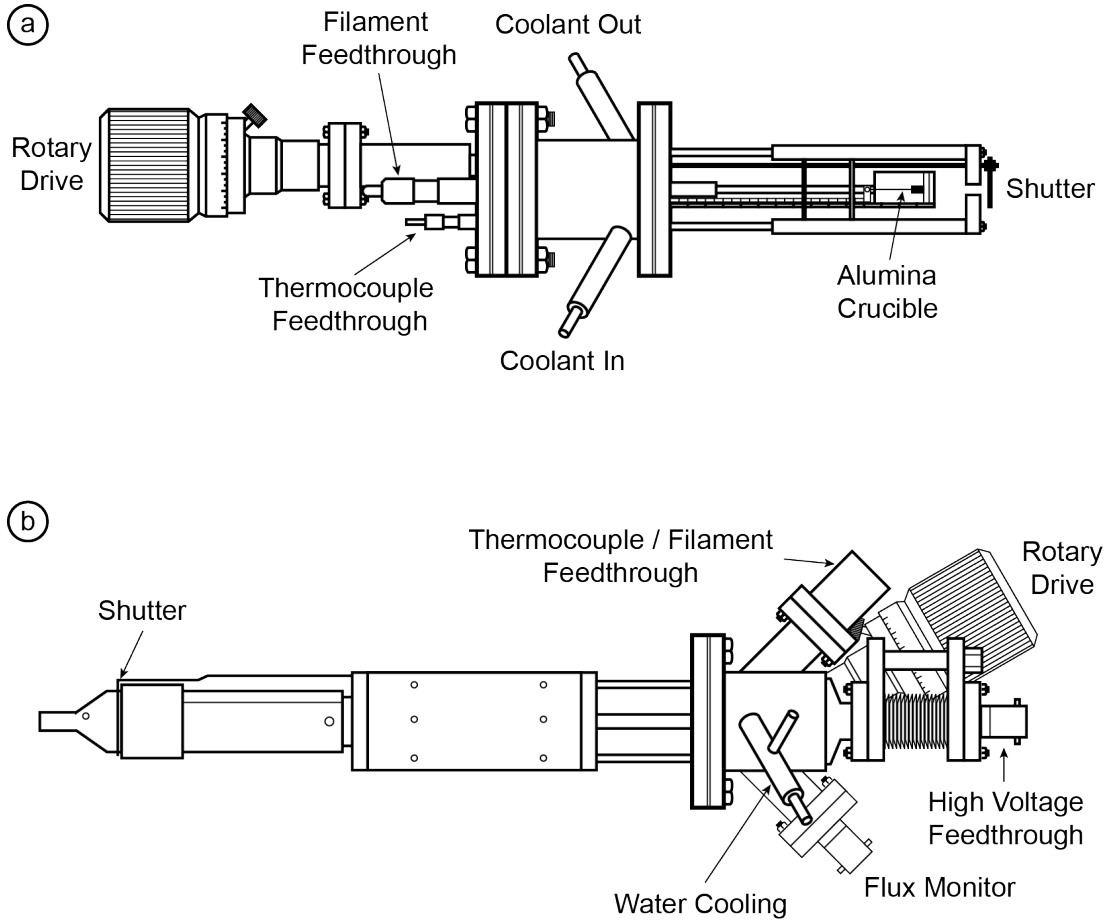

Figure 3.7 – Schematic of the two evaporators used throughout the work presented in this thesis: a) *J. Taylor and C. Nicklin* Compact Vapour Source, and b) *Omicron* EFM-3.

3.4 Auxiliary Analytical Instruments

3.4.1 Low Energy Electron Diffraction Optics

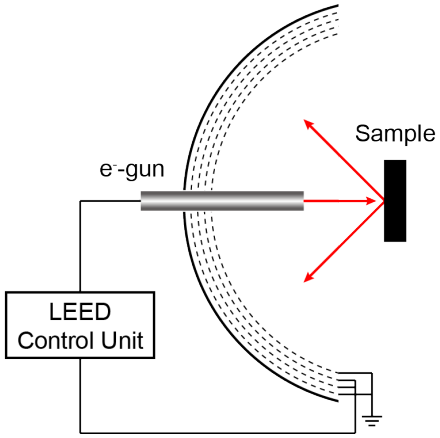

Figure 3.8 – Schematic displaying the optics and electronics for LEED.

An *Omicron* rear-view low energy electron diffraction (LEED) optics was used to perform LEED with the purpose of determining the order and symmetry of both single crystalline surfaces and adsorbed phases under UHV conditions. The apparatus is illustrated in figure 3.8 and comprises an electron gun, a four concentric grid system and a fluorescent phosphor screen. The electron gun generates a monochromatic electron beam in the energy range of 30 – 300 eV, which in turn is focused onto a conducting sample; the sample is earthed in order to prevent charging. The four-grid system ensures that only the electrons that are elastically scattered after undergoing diffraction reach the detector. The grids nearest and farthest from the sample are grounded to ensure that the electrons travel in a field free region; the grounding of the latter also screens out the high voltages applied to the detector. Together, the two intermediate grids form a filter and are negatively biased to $V = -E_p + \Delta V$, where E_p denotes the energy of the electron beam and ΔV is the range of 0 – 10 V. This bias ensures that only the elastically scattered electrons reach the screen, which is held at a positive high voltage (~ 6 kV) in order to accelerate the transmitted electrons to a sufficient kinetic energy to cause light emission from

the coated fluorescent screen. The impact of the diffracted electrons give rise to a pattern consisting of bright spots imprinted upon a dark background [4].

The same *Omicron* optics can also be employed for Auger electron spectroscopy (AES) when the four-grid system is used in retarding field analyser (RFA) mode, as illustrated in figure 3.9. In this mode, a modulating voltage is applied to the middle grids and a lock-in amplifier acts as a phase-sensitive detector to retrieve the Auger spectra. The Auger data is useful in determining the presence of contaminants and other adsorbates on the surface of the sample.

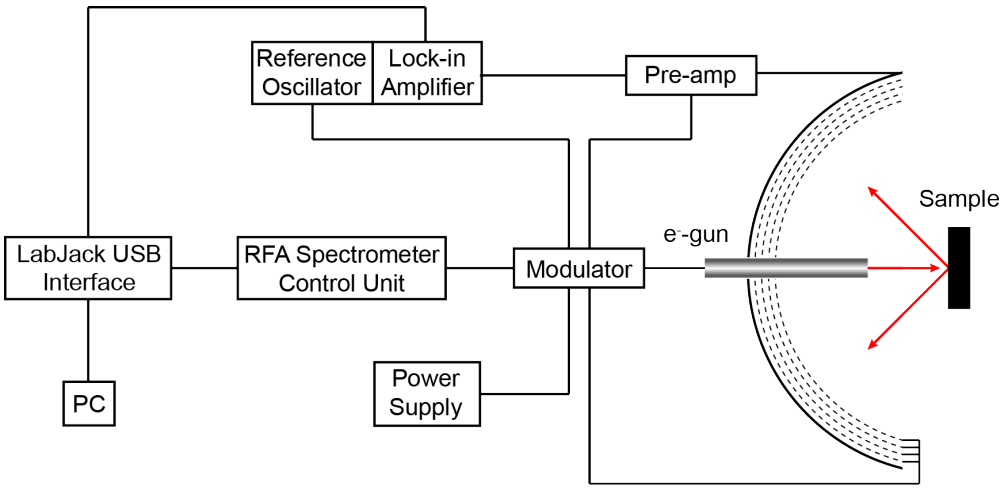

Figure 3.9 – Schematic displaying the optics operating in RFA mode for AES.

3.4.2 Quadrupole Mass Spectrometry

The VT-STM system has two *ESS Minitorr II* quadrupole mass spectrometers (QMS), one located in preparation chamber and another in the analysis chamber. This allows the composition of the residual vacuum to be determined in addition to the purity of the gases introduced from the various gas lines, namely argon used for sputtering and oxygen for oxidation. Leak checks can also be performed by focussing a small jet of helium onto the suspect area whilst monitoring the residual gas analysis (RGA) mass spectrum for the appearance of a peak at mass 4.

3.5 Synchrotron Radiation Beamlines

3.5.1 Advanced Light Source

The Molecular Science Beamline 11.0.2 stationed at the Advanced Light Source of the Lawrence Berkeley National Laboratory (California, U.S.A.), specifically the near-ambient pressure photoemission endstation, was employed for the experiment described in chapter 4. A schematic overview of the principal beamline components is shown in figure 3.10. An elliptically polarising undulator with a 5 cm period provides photons with energies between 75 – 2150 eV. The soft X-rays from the undulator are focused vertically onto the pre-mirror of a SX700 style plane-grating monochromator, which is equipped with two gratings (150 and 1200 lines/mm) [5]. The photons from the monochromator are then focused by one of the toroidal focus mirrors that generate a stigmatic focus. The horizontal and vertical Kirkpatrick–Baez mirrors ultimately focus the beam in the experimental chambers down to a spot size of 7 × 10 μm [6].

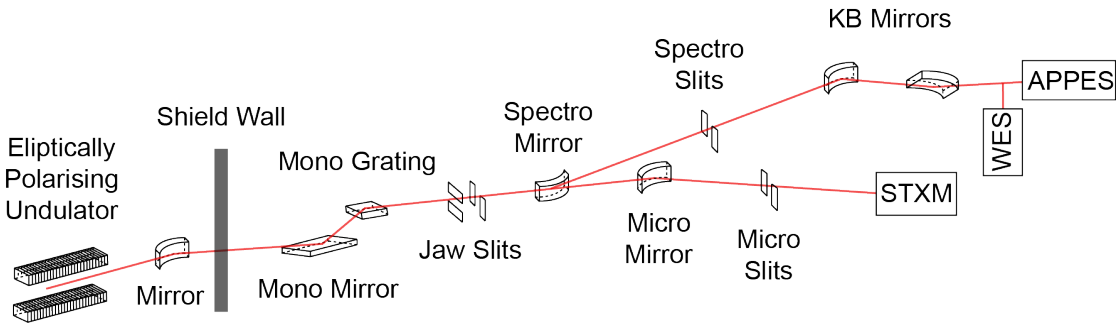

Figure 3.10 – Diagram of the layout of beamline 11.0.2 at the Advanced Light Source.

The beamline is divided into two branchlines and three end-stations. One of the branchlines is solely dedicated to the scanning transmission X-ray microscopy (STXM) endstation, while the other is split between the ambient pressure photoelectron endstation (NAPPES) and wet spectroscopy end-station (WES).

The NAPPES endstation permits spectroscopy studies up to pressures of 10 Torr. Conducting photoemission experiments at elevated pressures is far from trivial owing to the attenuation of the photoelectron signal due to scattering with gas phase molecules. Additionally, the setup must also take into account that the X-ray source and the electron analyser must be maintained under high vacuum. Therefore, the X-ray source is separated from the ambient pressure region by a 100 nm thick silicon nitride window, with a window-sample separation of 5 - 30 mm depending on the working pressure, i.e. smaller distances are selected for higher pressures in order to minimise gas-phase X-ray adsorption. Additionally, the aperture leading to of the *Specs Phoibos 150* hemispherical electron analyser is placed at a very small distance (0.5 mm) from the sample. As electrons are admitted through the aperture, they are focused in a first differential pumping stage onto a second aperture, and in the second differential stage onto a third aperture, before entering a final lens stage and eventually being focused onto the entrance slit of the hemispherical analyser. The pressure differential between the ambient pressure region and the analyser is about eight orders of magnitude [6].

The UHV system is composed of an analysis and a preparation chamber, both with a base pressure better than 2×10^{-10} Torr. In addition, there is also a load-lock chamber, which facilitates the fast exchange of samples. The preparation chamber is equipped with Auger and LEED optics for surface analysis, a sputter gun for sample cleaning, an evaporator and quartz crystal monitor for metal deposition, a residual gas analyzer for thermal desorption spectroscopy, leak valves for gas introduction, and a plasma source for dosing the sample with gas ions or radicals [7].

3.5.2 Diamond Light Source

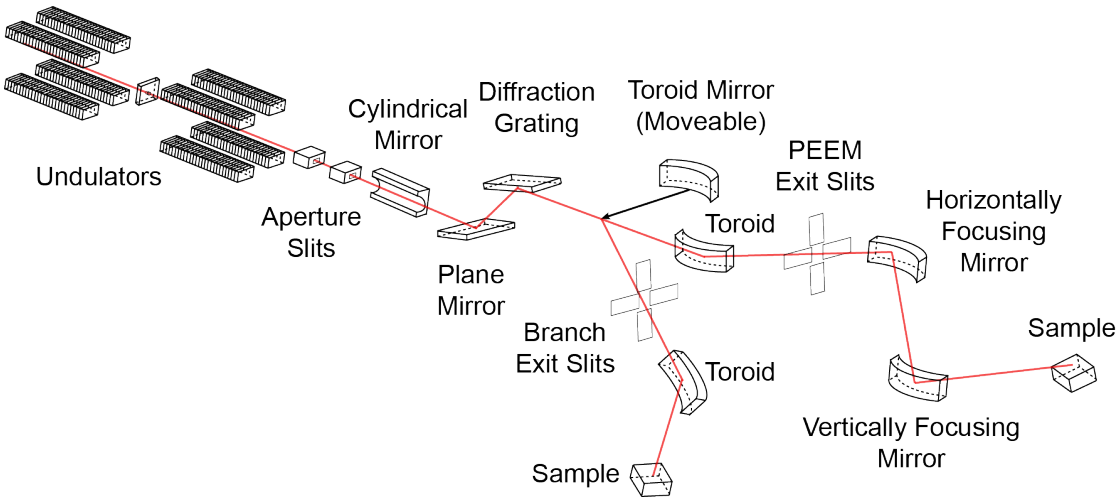

Figure 3.11 – Diagram of the layout of the I06 beamline at Diamond Light Source.

The experiments detailed in chapter 6 were conducted at the Nanoscience Beamline I06 of the Diamond Light Source (Oxfordshire, U.K.). The beamline offers variable circular and linearly polarised radiation in the energy range of 80 – 2100 eV. The photon energy range for circularly polarised light is 106 – 1300 eV, while linear polarised light is available from 80 – 2100 eV. The layout of the beamline is displayed in figure 3.11 and commences with two *APPLE II* undulators that provide left and right circularly polarised light in addition to linear light with an arbitrary polarisation between *s* and *p* polarisation. A set of mirror position after the undulators absorb most of the unwanted power from the insertion devices and collimate and focus the beam onto a monochromator. The collimated light plane monochromator is optimised for the mid energy-range region and has a resolving power $E / \Delta E$ in excess of 10000. Two toroidal mirrors placed after the monochromator focus the beam alternately at two exit slits which are the sources for either the Kirkpatrick–Baez refocus mirrors for the photoemission electron microscope (PEEM), or the toroidal refocus mirrors in the case of the branchline. The area of the focused photon beam is $3 \times 10\ \mu\text{m}^2$ [8].

In addition to the PEEM, the instrument (*Elmitec LEEM III*) also has a high stability electron gun for low energy electron microscopy (LEEM), thus this instrument is frequently known as a spectroscopic photoemission and low energy electron microscope (SPELEEM). The spatial resolution of the PEEM when using soft X-ray is in the order of 30-50 nm from a sample with an atomically flat surface, however when X-ray magnetic circular dichroism (XMCD) or X-ray magnetic linear dichroism (XMLD) are employed as contrast mechanisms the best resolution nears 60 nm. The PEEM endstation is also equipped with a scanning tunneling microscope (STM) in addition to standard sample preparation and characterisation facilities, including Auger electron spectroscopy (AES) and low energy electron diffraction (LEED). Photographs of the PEEM endstation can be visualised in figures 3.12 and 3.13.

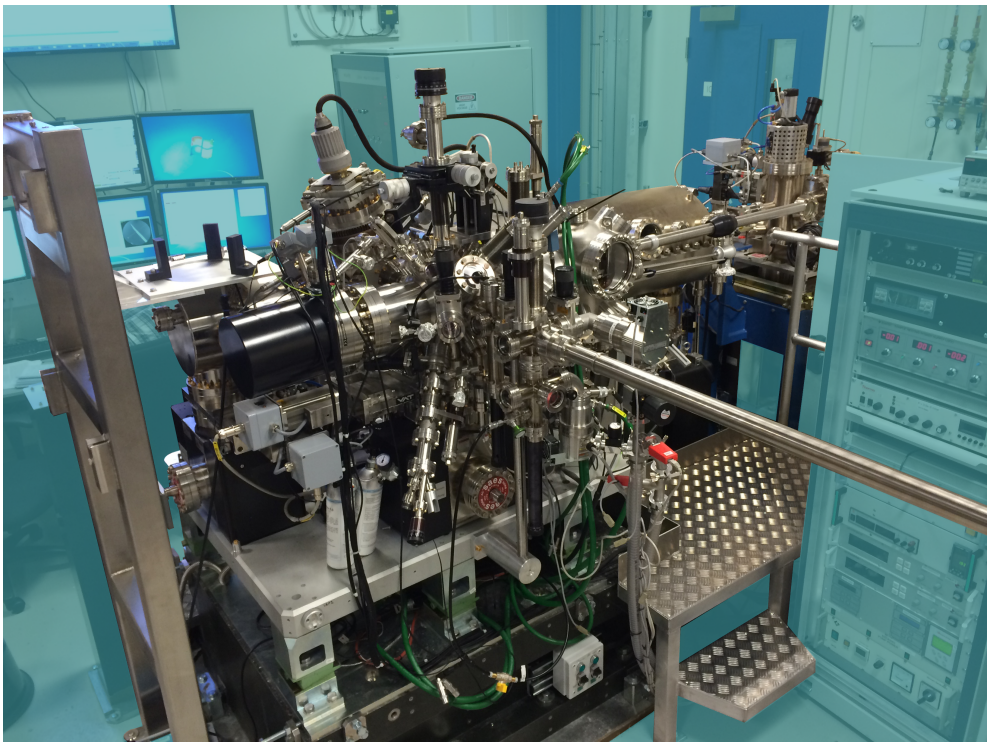

Figure 3.12 – Photograph of the preparation chamber side of the PEEM endstation of the I06 beamline located at Diamond Light Source.

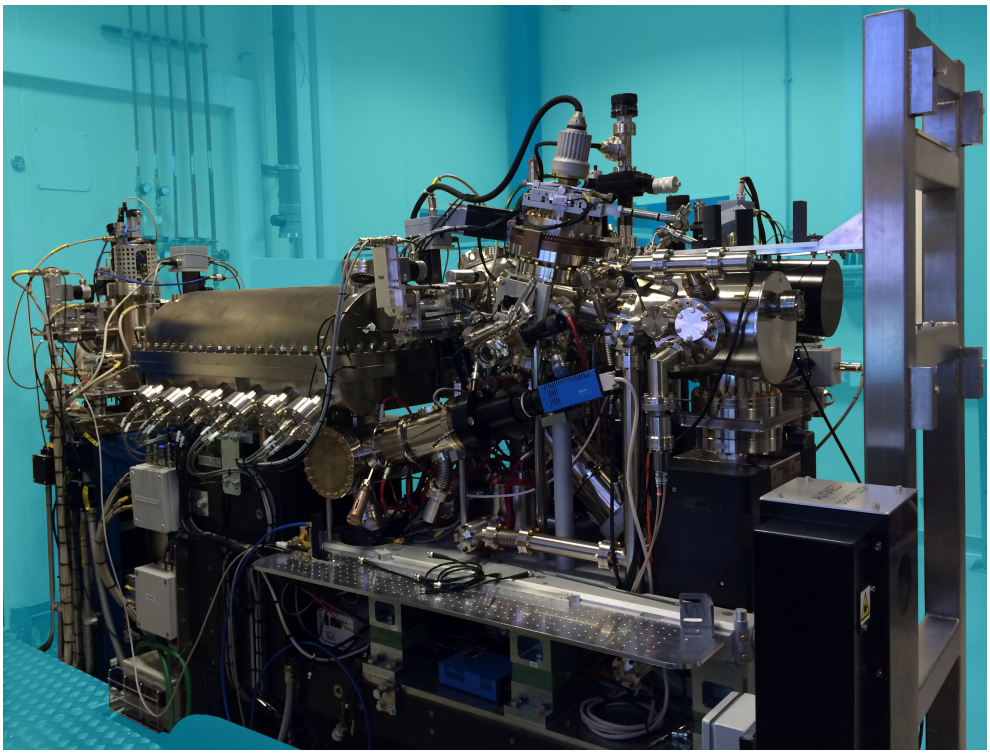

Figure 3.13 – Photograph of the analysis chamber side of the PEEM endstation of the I06 beamline located at Diamond Light Source.

A schematic diagram of the SPELEEM instrument can be visualised in figure 3.14. The complex optical layout of the instrument allows it to operate in energy-filtered imaging, energy-filtered micro-diffraction or micro-XPS (μXPS) mode (dispersive plane operation). In the energy-filtered mode the photoemission from the sample is stimulated using X-rays, and the field (ii), intermediate (iii) and projective lens (iv) magnify the image formed by the objective. Subsequent energy selection of the emitted photoelectrons is accomplished via the exit slit (EXS); an image of the probed area is then projected onto the detector using the projective lenses (p_2, p_3). The purpose of the contrast aperture (CA) in the diffraction plane is to restrict the acceptance angle of the photoelectrons, ensuring optimum resolution.

The intermediate (iii) and the projective lens (p_1) image the diffraction pattern produced by the objective in the energy-filtered micro-diffraction mode. The insertion of the analyser exit slit (EXS) permits angle resolved photoemission and X-ray photoelectron diffraction

measurements. The imaging plane field-limiting aperture (FLA) allows the selection of the probed sample area.

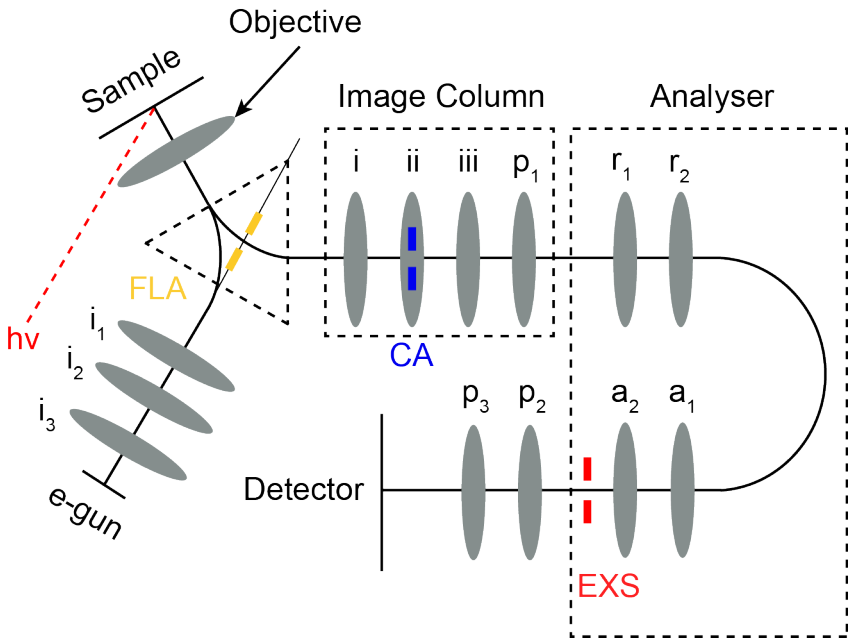

Figure 3.14 – Schematic diagram of the SPELEEM instrument. The sample is illuminated with soft X-rays (synchrotron) or low-energy electrons (electron gun); electrons from the electron gun are focused onto the sample by an illumination column composed of three condenser lenses (i_1, i_2 and i_3). The photoemitted or reflected electrons are accelerated by a strong field in the objective lens, which yields a magnified image of the sample. This image is further magnified by the transfer (i), field (ii) and intermediate lens (iii) onto the first projective lens (p_1) and into the energy analyser via the retarding lenses (r_1 and r_2). Located at the exit of the analyser are two sets of lenses, which accelerate (a_1 and a_2) and project (p_2 and p_3) the energy-selected electrons onto a two-dimensional image detector. Adapted from [9].

The contrast aperture (CA) is not inserted in the micro-XPS mode. Here the intermediate (iii) and projective lens (p_1) magnify the objective image, and the projective lenses p_2 and p_3 image the dispersive plane of the analyser onto the detector. As before, the field-limiting aperture (FLA) determines the probed area of the sample, and the contrast aperture (CA) limits the angular acceptance [9].

References

[1] D. P. Woodruff and T. A. Delchar, “Modern Techniques of Surface Science - D. P. Woodruff, T. A. Delchar - Google Books,” 1994.

[2] Omicron, “Omicron VT-STM User’s Guide,” pp. 1–20, Mar. 1994.

[3] J. Taylor and C. Nicklin, “The Compact Vapour Source,” pp. 1–9, Feb. 1996.

[4] G. Attard and C. Barnes, “Surfaces,” *Oxford Science Publications*, 1998.

[5] R. Follath and F. Senf, “New plane-grating monochromators for third generation synchrotron radiation light sources,” *Nucl Instrum Methods Phys Res A*, vol. 390, no. 3, pp. 388–394, Jan. 1997.

[6] H. Bluhm, K. Andersson, T. Araki, K. Benzerara, G. E. Brown, J. J. Dynes, S. Ghosal, M. K. Gilles, H. C. Hansen, J. C. Hemminger, A. P. Hitchcock, G. Ketteler, A. L. D. Kilcoyne, E. Kneedler, J. R. Lawrence, G. G. Leppard, J. Majzlam, B. S. Mun, S. C. B. Myneni, A. Nilsson, H. Ogasawara, D. F. Ogletree, K. Pecher, M. Salmeron, D. K. Shuh, B. Tonner, T. Tyliszczak, T. Warwick, and T. H. Yoon, “Soft X-ray microscopy and spectroscopy at the molecular environmental science beamline at the Advanced Light Source,” *Journal of Electron Spectroscopy and Related Phenomena*, vol. 150, no. 2, pp. 86–104, Feb. 2006.

[7] G. Ketteler, S. Yamamoto, H. Bluhm, K. Andersson, D. E. Starr, D. F. Ogletree, H. Ogasawara, A. Nilsson, and M. Salmeron, “The Nature of Water Nucleation Sites on TiO2(110) Surfaces Revealed by Ambient Pressure X-ray Photoelectron Spectroscopy,”

J Phys Chem C, vol. 111, no. 23, pp. 8278–8282, Jun. 2007.

[8] S. S. Dhesi, S. A. Cavill, A. Potenza, H. Marchetto, R. A. Mott, P. Steadman, A. Peach, E. L. Shepherd, X. Ren, and U. H. Wagner, "The nanoscience beamline (I06) at diamond light source," *AIP Conference Proceedings*, vol. 1234, no. 1, pp. 311–314, 2010.

[9] A. Locatelli and E. Bauer, "Recent advances in chemical and magnetic imaging of surfaces and interfaces by XPEEM," *J. Phys.: Condens. Matter*, vol. 20, no. 9, p. 093002, Feb. 2008.

CHAPTER 4

NEAR-AMBIENT PRESSURE PHOTOELECTRON SPECTROSCOPY OF WATER ON TiO_2(110)

Abstract

Near ambient pressure photoelectron spectroscopy (NAPPES) has been used to investigate the effects of temperature, and water and oxygen adsorption on the band gap state of rutile TiO_2(110). This state has long been attributed to bridging oxygen vacancies, hydroxyls and, more recently, also to subsurface titanium interstitials and oxygen vacancies. The majority of information we have on these systems is derived from ultra high vacuum investigations, which are far from the real operating conditions of this catalytic system. Here we conduct our X-ray photoelectron spectroscopy experiments at near-ambient pressures. In this work we expose the non-stoichiometric rutile TiO_2(110) surface to water and oxygen at an array of temperatures whilst monitoring the band gap state and other core-level spectra. Our results show that temperature, oxygen and high pressures of water have a marked effect on the band gap state of rutile TiO_2(110).

4.1 Introduction

Titanium dioxide is one of the most studied metal oxides in surface science, mostly due to its role as a key component in numerous technologies such as photocatalysis [1], self-cleaning surfaces [2], dye-sensitised solar cells [3], pigments [4], semiconducting devices [5], gas sensing [6], to name but a few. The interest in TiO_2 was prompted by the discovery of its remarkable photocatalytic water-splitting capabilities by Fujishima and Honda, in 1972 [7]. In fact, the interaction between water and TiO_2 underpins many processes that drive modern commercial applications. The vast amount of research into TiO_2 has resulted in the rutile (110) surface becoming the prototypical metal oxide surface with which to explore the surface physics and chemistry of metal oxides in general.

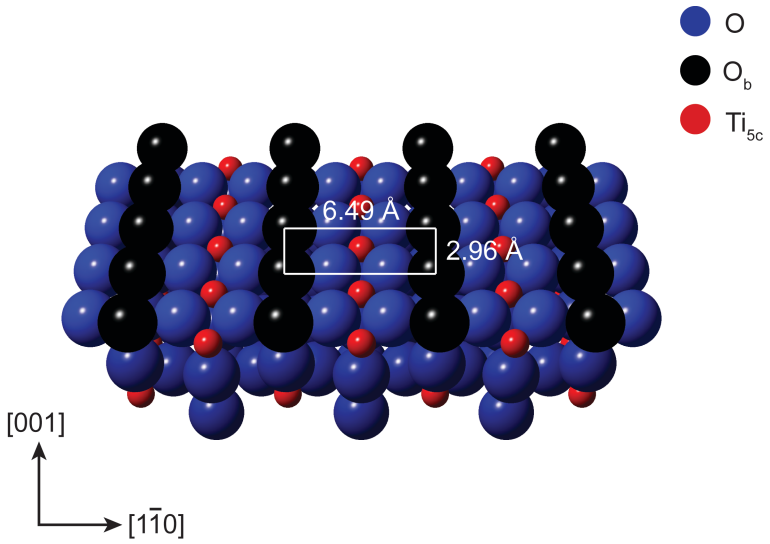

Figure 4.1 – Ball model of the stoichiometric rutile TiO_2(110) surface, where the black, blue and red spheres represent bridging oxygen, in-plane oxygen and titanium atoms, respectively. The dimensions of the (110) surface unit cell are represented by the inset rectangle.

A ball model of the stoichiometric rutile TiO_2(110) surface and its respective unit cell are displayed in figure 4.1. The structure at the solid-vacuum interface is composed of alternating rows of twofold coordinated bridging oxygen (O_b) and fivefold coordinated titanium atoms (Ti_{5c}) that run in the [001] direction, as well as in-plane oxygen (O). Rutile TiO_2 possesses a band gap of about 3 eV, and thus requires a specific preparation method in order to make it

sufficiently conducting for electron-based techniques. This method involves cycles of Argon ion sputtering and annealing in order to reduce the crystal and improve conductivity. A sample prepared in this manner displays a certain degree of non-stoichiometry that takes the form of point defects, including bridging oxygen vacancies at the surface and interstitial titanium species [8-10]. Such non-stoichiometric surfaces display a band gap state, which appears as a feature at ~1 eV below the Fermi level (E_F) in ultraviolet photoelectron spectroscopy (UPS) [11-13] and as a ~1 eV loss feature in electron energy loss spectroscopy (EELS) [14]. Additionally, resonant photoelectron spectroscopy has confirmed the Ti *3d* nature of this state in rutile TiO_2 crystals [15].

First investigations into the origin of the band gap state of rutile TiO_2 were performed by Henrich *et al*. and involved the argon ion bombardment of the surface, followed by the exposure of the sample to oxygen. It was observed that the defects created upon bombardment induced a state in the band gap, and that the healing of the surface with oxygen resulted in the quenching of this state [13]. The observation that these defects were healed upon oxygen exposure lead to the conclusion that the band gap state stemmed from O_b vacancies. This theory is known as the O-vacancy model and was rationalised by the proposition that when O_b vacancies are created, two excess electrons associated with each vacancy are transferred to empty *3d* states of adjacent Ti_{5c} ions, forming two Ti^{3+} sites [16]. While the O-vacancy model has been widely accepted by the surface science community, the exact origin of the band gap state is still highly debated [11, 17-19] .

Theoretical calculations regarding the origin of the band gap state are also equivocal. Some studies provide evidence that substantiate the proposed O-vacancy model, such as those performed by Di Valentin *et al*. [20] and Papageorgiou *et al*. [21]. In the former, spin polarised hybrid DFT calculations predicted that both O_b vacancies and OH_b molecules give rise to localised Ti^{3+} states, at about 1 eV below the conduction band. However, another spin polarised

hybrid DFT calculation by Finazzi *et al*. suggests that Ti^{3+} interstitials can also contribute to the band gap state intensity [22].

The adsorption of molecules such as water and oxygen on the rutile TiO_2 surface is of great interest from the standpoint of investigating the origin of this substrate's catalytic activity. The interaction of oxygen with TiO_2 has attracted much attention due to its importance in a number of catalytic and photocatalytic processes, including water treatment and waste remediation, where oxygen is not only an important oxidizing reagent in the photooxidation processes, but also an electron scavenger that facilitates these reactions [23]. The interest in water as an adsorbate arises from the key role it plays in numerous photocatalytic applications of TiO_2, for example the oxidation of organic pollutants and hydrogen production via water splitting [24].

4.1.1 Oxygen Adsorption on Rutile TiO_2(110)

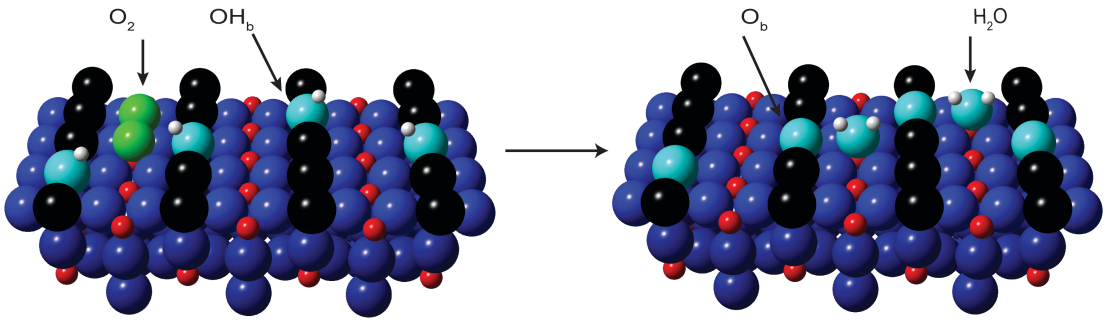

Figure 4.2 – Ball model portraying the overall reaction mechanism for O_2 on a hydroxylated rutile TiO_2(110) surface, whereby the reaction between OH_b and O_2 results in the formation of H_2O and O_b. Green, blue and red spheres denote O, lattice O and Ti_{5c} atoms, respectively. The black spheres are O_b atoms, which lie in the [001] azimuth of the substrate. The light blue spheres denote OH_b (left) or O_b (right). The small white spheres represent hydrogen atoms.

Figure 4.2 illustrates the overall reaction mechanism for oxygen adsorption on the hydroxylated TiO_2(110) surface, which is initiated by the removal of capping hydrogen atoms from OH_b groups and results in the formation of water molecules, as shown in equation 4.1:

$$4OH_b + O_2 \rightarrow 4O_b + 2H_2O \quad (4.1)$$

The intermediate steps of the overall reaction mechanism that lead to the formation of water molecules involve several reactions as shown in the ball model diagram of figure 4.3 and in equations 4.2 – 4.5:

$$OH_b + O_2 \rightarrow O_b + HO_2 \quad (4.2)$$

$$OH_b + O_{ad} \rightarrow OH_t + O_b \quad (4.3)$$

$$OH_b + HO_2 \rightarrow O_b + O_{ad} + H_2O(g) \quad (4.4)$$

$$OH_b + OH_t \rightarrow O_b + H_2O(g) \quad (4.5)$$

where O_{ad} represents oxygen adatoms and OH_t terminal hydroxyls [25]. The exposure of the TiO_2(110) surface to a pressure of oxygen that exceeds the minimum amount necessary to remove capping H results in the formation of further reaction products; the majority species (80%) are assigned to OH_t and the minority species are yet to be identified [23, 24, 26]. There are two reported channels for the dissociation of O_2 molecules, either at O_b vacancies or Ti_{5c} troughs [19, 24, 25, 27-29]. In the former, one O atom fills the vacancy while the other is either deposited on a nearby Ti_{5c} site as an O_{ad} or is desorbed, as shown in equation 4.6:

$$O_2 \xrightarrow{O_b vacancy} O_b + O_{ad} \quad (4.6)$$

The second channel is unrelated to O_b vacancies, whereby an O_2 molecule dissociates at a Ti_{5c} site to form a pair of O_{ad} species, as indicated in equation 4.7:

$$O_2 \xrightarrow{Ti_{5c}} 2O_{ad} \quad (4.7)$$

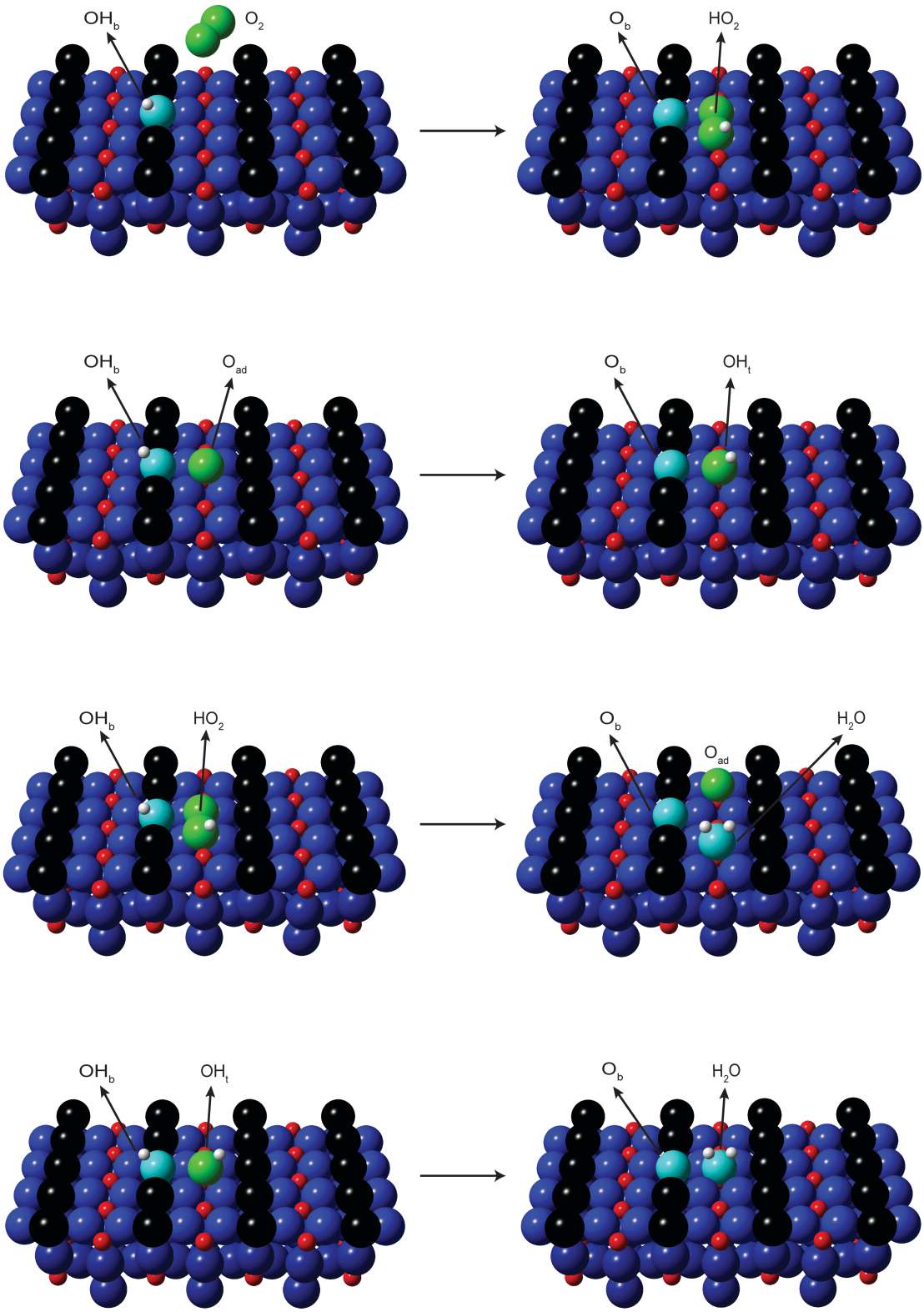

Figure 4.3 – Model of the four intermediate reactions that lead to the formation of H_2O. The blue, red and white spheres denote lattice O, Ti_{5c} and H, respectively. The black spheres are O_b atoms, which are oriented along the [001] azimuth.

4.1.2 Water Adsorption on Rutile TiO_2(110)

There is a general consensus that water dissociates on the non-stoichiometric rutile TiO_2(110) surface at O_b vacancies, forming two OH_b species according to the model displayed in figure 4.4. These hydroxyls then act as nucleation sites that anchor incoming water molecules, forming strongly bound hydroxyl-water complexes that continue to act as nucleation centres at elevated pressures, permitting further water adsorption [24,30-37]. This implies that a TiO_2(110) surface containing 5% monolayer (ML) of O_b vacancies yields approximately 10% ML of OH_b species.

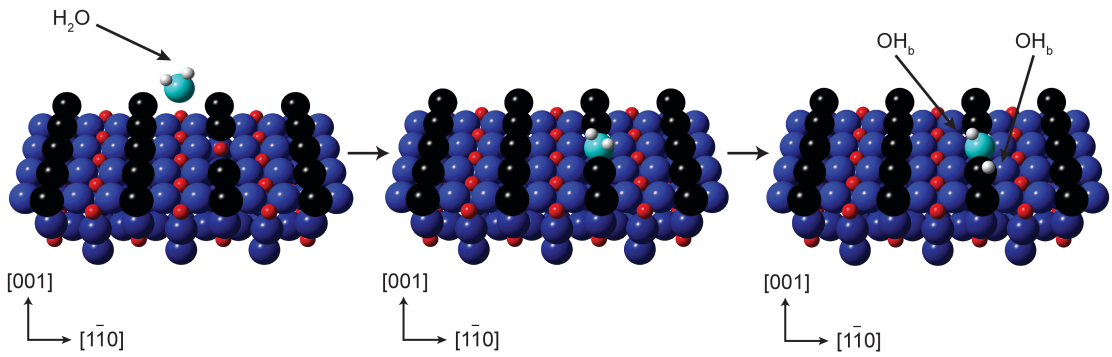

Figure 4.4 – Ball model illustration of dissociative water adsorption at a O_b vacancy on the non-stoichiometric rutile TiO_2(110) surface, where each water molecule leads to the formation of two OH_b. Dark blue and red spheres denote lattice O and Ti, respectively. The black spheres are O_b atoms, which run along the [001] direction of the substrate. The small white spheres represent hydrogen atoms.

Contrary to the non-stoichiometric rutile TiO_2(110) surface, the adsorption process for water in the absence of O_b vacancies is still a highly debated topic. One of the difficulties in obtaining definitive experimental data is that of developing an adequate preparation method to prepare defect free surfaces [24]. Further difficulties may also reside in the elusive nature of the dissociated state, either due to the fact that the dissociated state is too ephemeral, or because distinction between molecular water and the dissociated products is problematic. Recent photoelectron studies by Walle *et al*. [38] and Amft *et al*. [39] suggests that the adsorption of

water on the perfect TiO_2(110) surface is governed by a balance between molecular and dissociative adsorption that shifts towards molecular adsorption with increasing coverage, in accordance with numerous theoretical calculations [30,39-42]. Water adsorbs molecularly at low temperatures (~160 K), with dissociative adsorption occurring at O_b and Ti_{5c} sites, leading to the formation of one OH_t and one OH_b per water molecule, when the sample is heated to ~290 K for a coverage of up to 0.25 ML, as illustrated in figure 4.5.

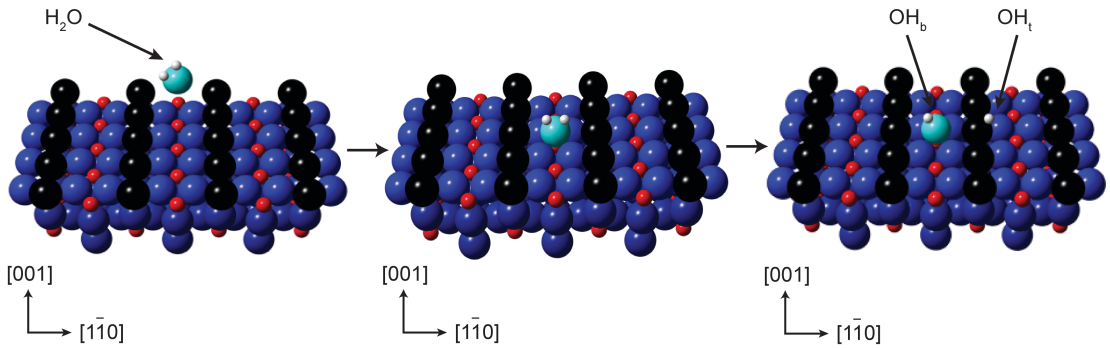

Figure 4.5 – Ball model illustration of dissociative water adsorption on a Ti_{5c} site on the stoichiometric rutile TiO_2(110) surface, where each water molecule leads to the formation of one OH_b and one OH_t. Dark blue and red spheres denote lattice O and Ti, respectively. The black spheres are O_b atoms, which run along the [001] direction of the substrate. The small white spheres represent hydrogen atoms.

A recent study by Martinez *et al*. has identified an additional pathway for the dissociation water at room temperature, the step edges of rutile TiO_2(110) [43-45]. On rutile TiO_2(110), the step edges run predominantly in the [001] and $[1\bar{1}1]$ directions. A stable reconstruction of the latter step edge, denoted $[1\bar{1}1]_R$, has been proposed and is characterised by one additional TiO_2 unit per step unit cell. The $[1\bar{1}1]_R$ step edges on the surfaces of vacuum annealed TiO_2(110) crystals appear reduced, with the O_b rows at the upper terraces terminating with O vacancies at the step edges, termed O_s. These O_s vacancies are active sites for the dissociation of water, similar to O_b vacancies on terraces.

4.2 Experimental Procedure

The experiments were performed on the NAPPES endstation of the Molecular Environmental Science beamline (11.0.2), at the Advanced Light Source (Lawrence Berkeley National Laboratory, California, USA). The details of the beamline and NAPPES endstation are described in depth in chapter 3.

The rutile TiO_2(110) single crystal was prepared by successive cycles of Argon ion sputtering (10 minutes, 5 mA, 1 keV) and annealing in UHV (15 minutes, 1000 K). This reduction procedure ensures sample conductivity and yields a slightly oxygen deficient surface with a well-ordered (1x1) periodicity, as characterised by LEED. The sample temperature was monitored throughout the experiment using a K-type (chromel-alumel) thermocouple.

The analysis chamber was flushed with ~0.2 Torr of water prior to introducing the rutile TiO_2(110) sample, with the purpose of displacing contaminants from the inner chamber walls during the pump-out. The water was contained within a glass vial, coupled to the gas line of the UHV system, and purified via several freeze-pump-thaw cycles. All gases used in these experiments were introduced into the analysis chamber through a high-precision leak valve. The pressure inside the chamber was measured using a pirani gauge in the low-pressure regime ($<10^{-4}$ Torr), and a baratron for higher pressures (10^{-4} – 10^{-1} Torr). The cleanliness of the sample was monitored throughout the experiment using X-ray photoelectron spectroscopy (XPS). The fitting of all XPS spectra was performed using the CasaXPS software.

To ensure the reliability and reproducibility of our results, the extent of the damage caused by prolonged beam exposure to the sample was assessed. This was achieved by performing a series of identical XPS scans before and after focussing the beam on an area of the sample for an extended period of time. After 20 minutes, the only perceivable change in the spectra was a small decrease in the photoelectron intensity. Nevertheless, a different area of the sample was

chosen for each scan to further minimise the probability of beam-induced damage to the TiO_2(110) surface.

The main objective of this experiment was to investigate the nature of the band gap state of rutile TiO_2(110) in the presence of water and oxygen, in addition to the effects of temperature. For simplicity, the experimental conditions are expressed in the text in terms of relative humidity (RH), as this combines two variables, temperature and pressure [46]. The RH is defined as $p/p_v(T)\times 100$, where p_v is the equilibrium vapor at a temperature T [34]. The coverage was calculated using the method described in Appendix A, and is stated in terms of monolayer (ML), where one ML of adsorbates is defined as one per primitive surface unit cell, i.e. a density of 5.2 x 10^{14} cm^{-2}.

4.3 Results and Discussion

4.3.1 Water

The purpose of the first segment of the experiment was to investigate the effect of water adsorption on the band gap state of rutile TiO_2(110). After the sample was prepared using the procedure described in section 4.2, the survey scan displayed in figure 4.6 was acquired to verify sample cleanliness. There are several noticeable features in the spectrum: the Ti and O core-level and Auger peaks, and a small Ar peak that can be attributed to remnants from the sample preparation procedure. No contaminants are observed in the spectrum, or they are below the detection threshold of the analyser. The preparation method described above in section 4.2 is expected to yield a TiO_2(110) surface with a certain degree on non-stoichiometry, as confirmed by the presence of the reduced state Ti^{3+} in the Ti *3p* photoelectron spectrum. A linear background was subtracted from the spectrum, and three Gaussian-Lorentzian (30:70) peaks were used to fit the data. The deconvolution of the Ti *3p* spectrum from the as-prepared

sample is displayed in figure 4.7, and reveals contributions from Ti^{4+} at 37.5 eV binding energy (BE), Ti^{3+} at 36.2 eV (BE), and a satellite peak at 38.7 eV (BE) [47,48].

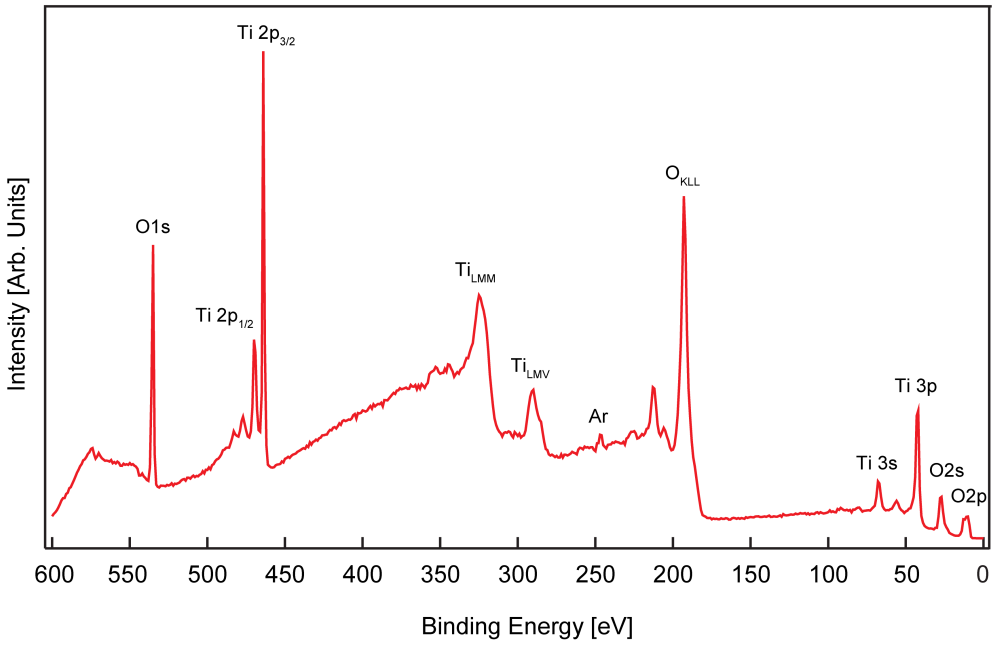

Figure 4.6 – X-ray photoelectron spectrum of the as-prepared rutile TiO_2(110) surface ($h\nu$ = 700 eV, E_{pass} = 10 eV, E_{step} = 0.5 eV).

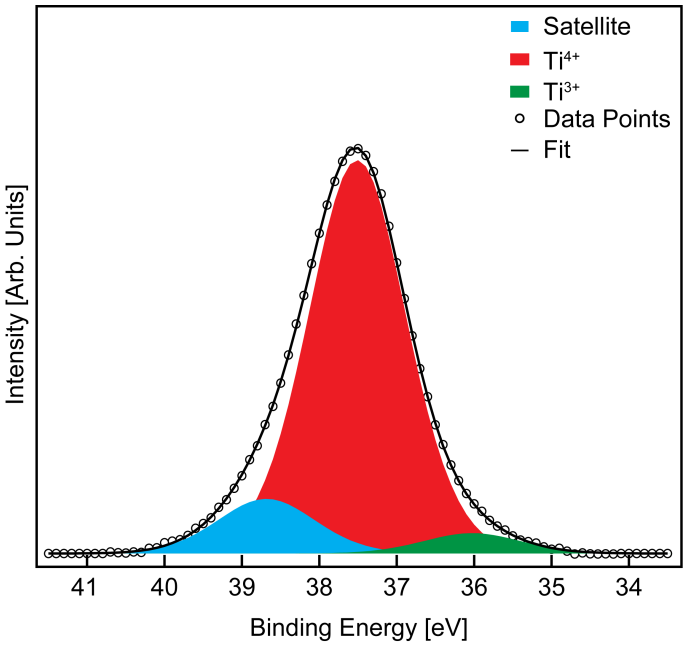

Figure 4.7 – X-ray photoelectron spectrum of the Ti *3p* region from an as-prepared rutile TiO_2(110) sample ($h\nu$ = 465.5 eV, E_{pass} = 10 eV, E_{step} = 0.1 eV). A linear background was subtracted and the Ti *3p* peak was fitted with three Gaussian-Lorentzian type curves (30:70) pertaining to contributions from bulk Ti^{4+}, reduced state Ti^{3+} and a satellite feature.

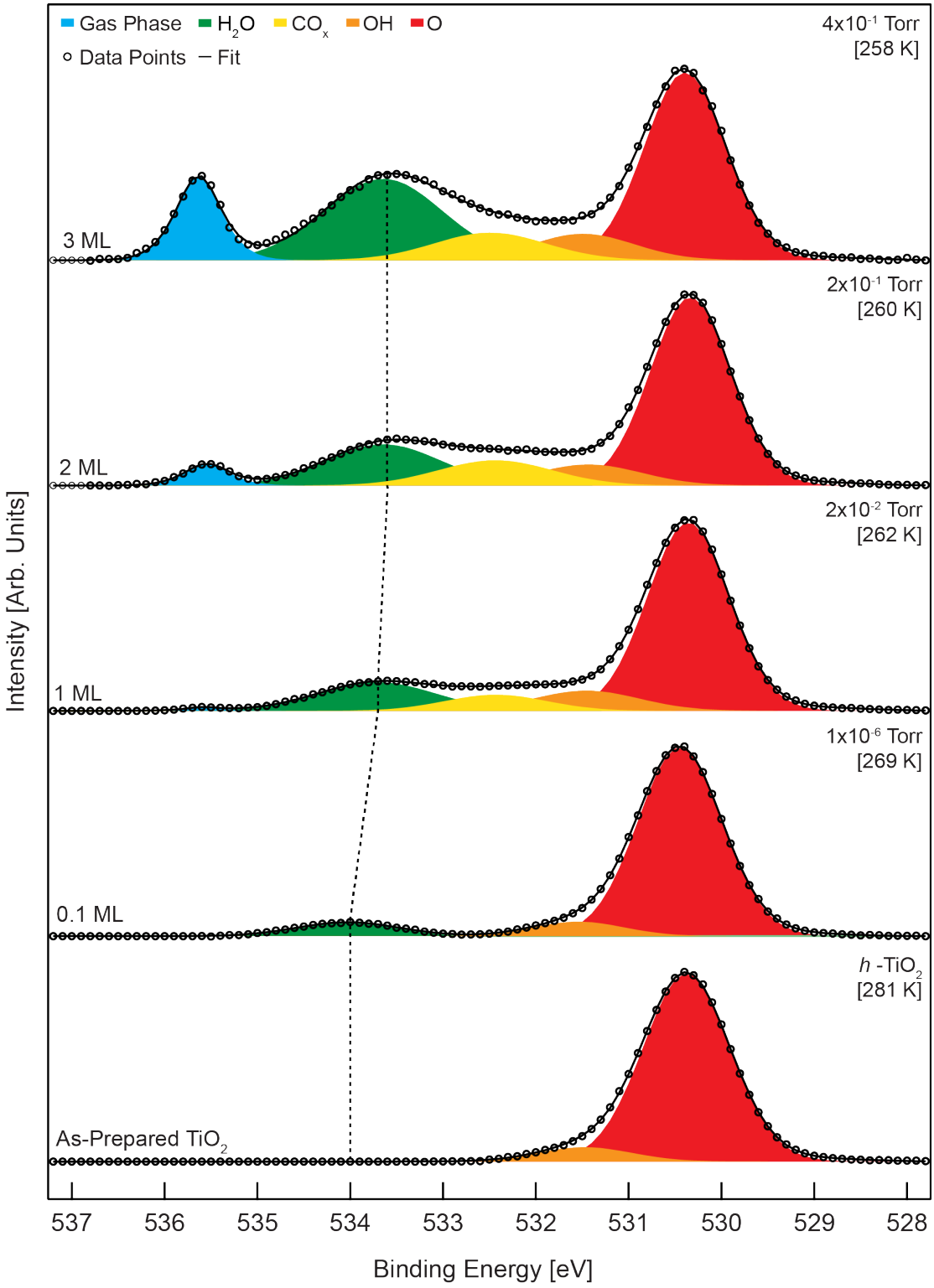

Figure 4.8 – X-ray photoelectron spectra of the O *1s* region of rutile TiO_2(110) ($h\nu$ = 700 eV, E_{pass} = 10 eV, E_{step} = 0.1 eV). The spectra have been normalised and aligned to the main O *1s* peak, and are displayed offset by constant vertical increments for clarity. The deconvolution of the spectra was performed using Gaussian-Lorentzian lineshapes (30:70), after a Shirley type background had been subtracted. The estimated water coverage (left) and relative humidity values (right) are also indicated. The method used to calculate the water layer thickness is described in Appendix A.

X-ray photoelectron spectroscopy offers a means of investigating the interaction of adsorbed atoms or molecules with a surface as a consequence of the features that these induce. As such, the adsorption of H_2O may be monitored through the analysis of the features that arise in the various XPS spectra acquired. In figure 4.8, a representative selection of O *1s* spectra are displayed, acquired at increasing pressures of H_2O; the coverage of H_2O is also indicated, expressed in terms of ML [34]. The O *1s* spectra are a clear indication of the progressive growth of a water overlayer on the TiO_2(110) surface, where different types of oxygen species, i.e. lattice O, OH, and H_2O, are distinguishable by their different binding energies.

The spectra were fitted using Gaussian-Lorentzian (30:70) lineshapes and a Shirley type background, in which the background intensity at any given binding energy is proportional to the intensity of the total peak area above the background in the lower binding energy peak range [49]. The subtraction of a Shirley background results in a quasi-symmetrical Gaussian-Lorentzian peak, which is ideal for use in quantitative analysis [50]. The spectrum of the as-prepared surface, acquired at a temperature of ~280 K, displays two peaks, one pertaining to OH (531.6 eV), and the other to lattice O (530.4 eV). The OH peak arises through mere exposure of the sample to the residual chamber gases, which leads to the hydroxylation of the surface, as described in section 4.1. The initial introduction of H_2O into the system, corresponding to a RH of $4x10^{-5}$ % (P= $1.3x10^{-6}$ Torr, T= 269 K), leads to the appearance of a new peak that is assigned to molecularly adsorbed H_2O (534 eV). In the spectra of the three highest partial pressures of H_2O, corresponding to RH values of ~1% (P= $2.0x10^{-2}$ Torr, T= 262 K), ~15% (P= $2.0x10^{-1}$ Torr, T= 260 K) and ~30% (P= $4.0x10^{-1}$ Torr, T= 258 K), two more peaks are observed. One of the peaks is ascribed to gas phase H_2O (535.6 eV), and the other to CO_x contamination (532.4 eV). The peak pertaining to molecular H_2O shifts towards lower binding energy with increasing H_2O partial pressure, which is attributed to changes in adsorption geometry and has been reported previously in the literature [34,51].

Contamination of the sample with carbon containing oxygen species is common in near ambient pressure studies [34,52]. The intensity of the CO_x peak increased with RH, and evacuation of H_2O from the system lead to a decrease in the intensity of this peak but not its eradication. The deconvolution of the C *1s* region is presented in figure 4.9 and includes components ascribed to oxygen containing carbon species, located on the high binding energy side of the main carbon peak (285 eV). Additional calculations indicate that at the maximum value of 30% RH, the sample surface contains around 0.7 ML of this contaminant [53].

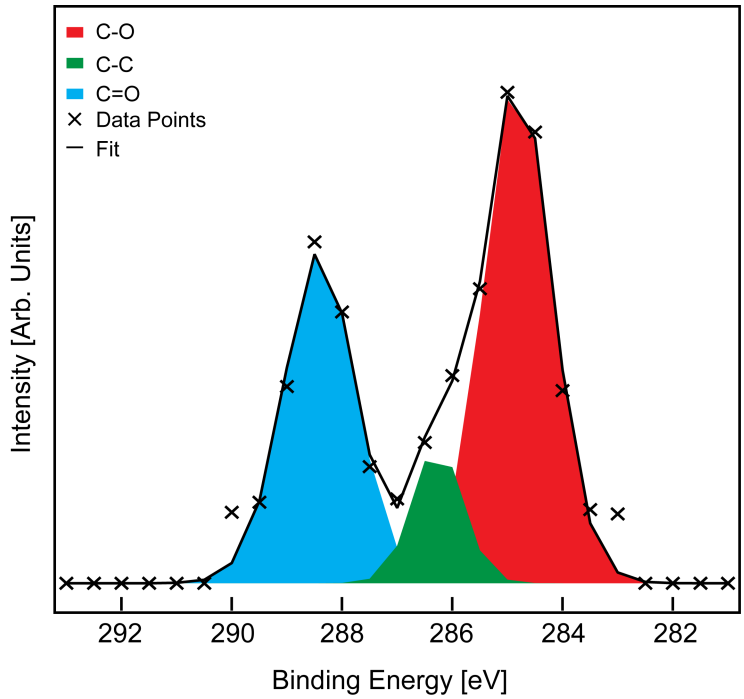

Figure 4.9 - X-ray photoelectron spectrum of the C *1s* region of rutile TiO_2(110) with a 1 ML overlayer of water, confirming the presence of oxygen containing carbon species at the surface ($h\nu$ = 490 eV, E_{pass} = 10 eV, E_{step} = 0.5 eV). The spectrum was fit with three Gaussian-Lorentzian (30:70) curves after a linear type background was subtracted.

The presence of water on the rutile TiO_2(110) is further corroborated by the appearance of the characteristic molecular orbitals of water $1b_1$, $3a_1$ and $1b_2$, visible in the valence band (VB) spectra of figure 4.10, acquired at an energy off-resonance with the Ti *3d* electron state. The $1b_1$ orbital is of nonbonding character and is situated around 7.5 eV below the Fermi level, whereas the $1b_2$ is a bonding orbital, located at about 13.2 eV. The $3a_1$ peak, at approximately 10.3 eV,

contains both bonding and non-bonding character, and is thought to be the orbital that interacts most strongly in bonding to the surface [12, 35, 54, 55]. Visualisation of these water-induced features in the photoelectron spectra is facilitated by the production of difference spectra, obtained via the subtraction of the as-prepared surface spectrum from those obtained after exposing the sample to water.

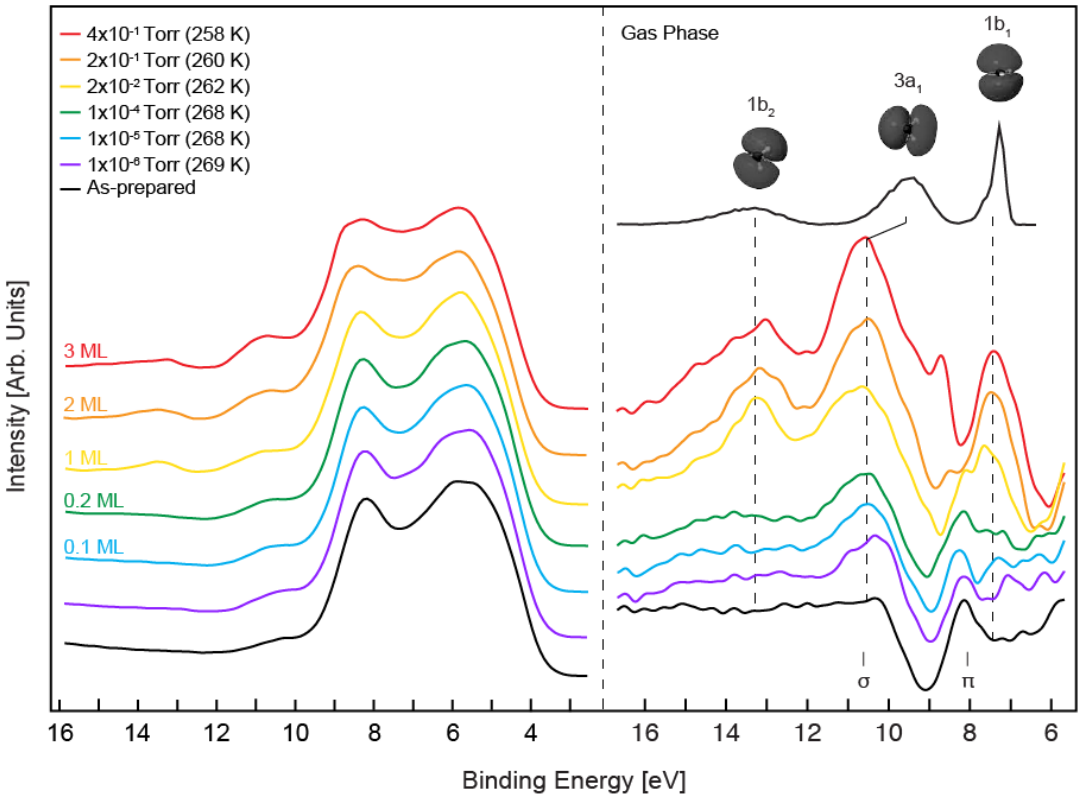

Figure 4.10 - X-ray photoelectron spectra of the valence band region of rutile TiO_2(110) aligned to the O *2s* core-level peak at 22.5 eV (BE), before and after water dosing (left). Difference spectra of the photoelectron spectra obtained by subtracting spectrum from the as-prepared sample from spectra recorded after exposing the surface to increasing amounts of water (right). A spectrum of the water gas phase, acquired by retracting the beam by 2.1 mm from the sample, is aligned with the $1b_1$ molecular orbital peak. The spectra were recorded at an energy off-resonance with the Ti *3d* electron state ($h\nu$ = 455 eV, E_{pass} = 10 eV, E_{step} = 0.1 eV) and are displayed vertically offset for clarity.

The use of photoelectron difference spectra as an analysis technique is very frequent, however this method is far from trivial. Prior to subtraction, the spectra must undergo a normalisation and alignment process, and the slightest error can result in the appearance of problematic

artefacts in the resultant difference spectra. In this particular case, the problems associated with normalisation arise mainly from the attenuation of the substrate signal by the water overlayer, which can be corrected by increasing the amplitude of the dosed spectra through multiplying each spectrum by an empirically determined factor. If both the clean and the dosed spectra contain a substrate feature that is unaffected by the adsorbate then it is often sensible to normalise the dosed spectrum to this feature. In this case, an unaffected feature present on the low binding energy side of the O *2s* core-level at approximately 16.7 eV was used for normalisation. A similar approach has been reported previously in the literature [12,34]. The normalisation procedure was also attempted using the O *2s* core-level peak, with very similar results. The spectra of figure 4.10 have also been corrected for variations in binding energy due to band bending arising from chemisorption of the adsorbates. The alignment of the binding energies was achieved through the interpolation of the spectra onto a fine mesh, enabling shifts as small as 0.01 eV.

The difference spectra of the off-resonance region are presented in the right image of figure 4.10. The gas phase spectrum of water is also displayed in the figure facilitating the identification of the adsorbate-induced structure. In order to align the gas phase spectrum with the $1b_1$ molecular orbital peak, the gas phase spectrum was shifted by 4.7 eV towards lower binding energy, which is in good agreement with the values reported in the literature [12,55]. The shift of the $3a_1$ molecular orbital peak from the position in the gas phase spectrum is due to the presence of chemisorbed water at the surface [54]. The $1b_1$ and $3a_1$ molecular orbital peaks display a slight broadening which may be assigned to the superposition of the σ and π hydroxyl orbitals, located at ~10.5 and ~8 eV respectively. Similarly, an underlying band gap state satellite at around 13.9 eV may also contribute to the width of the $1b_2$ feature. The survey spectra were examined in detail for evidence of similar peaks, and confirmation of their existence is presented in figure 4.11. The origin of these satellites has been previously assigned to O ($2p_{e_g}$) – Ti ($3d_{e_g}$) charge transfer [47, 56, 57].

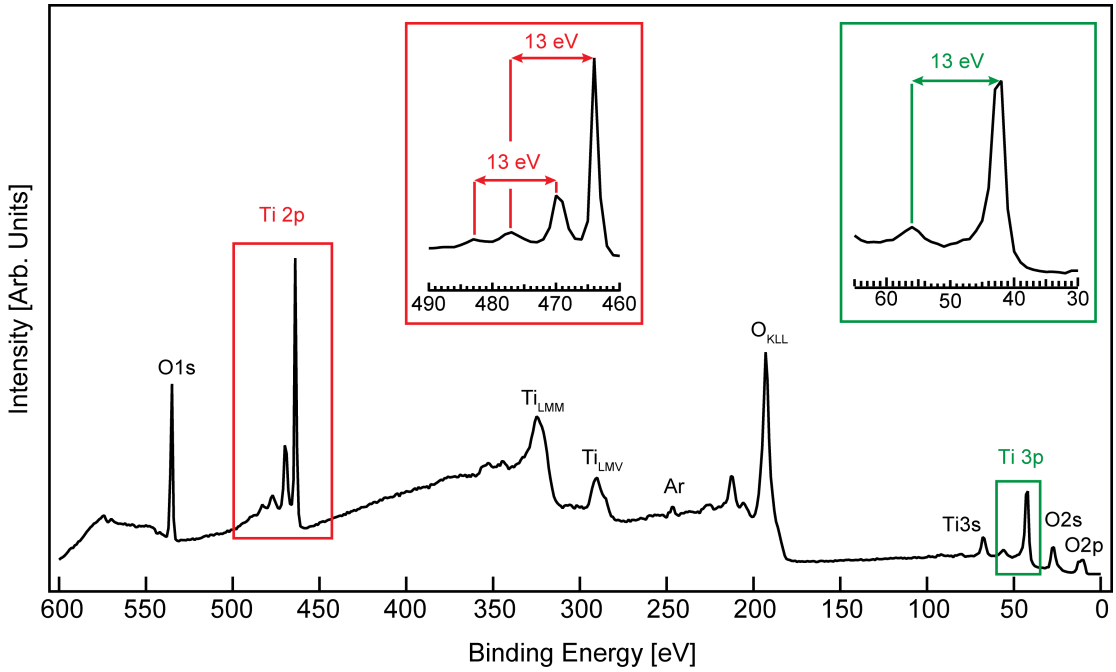

Figure 4.11 - X-ray photoelectron spectrum of an as-prepared rutile TiO_2(110) sample, highlighting the existence of various satellite peaks, such as the Ti *2p* and Ti *3p* satellites, separated about 13 eV from the core-level peaks ($h\nu$ = 700 eV, E_{pass} = 10 eV, E_{step} = 0.5 eV).

The on-resonance valence band photoelectron data are displayed in figure 4.12, containing peaks pertaining to the O *2s* (~22.5 eV), Ti_{LVV} (~15 eV), valence band (~3 - 9 eV) and the band gap state. The band gap peak is located at approximately 0.9 eV below the Fermi level, and is of Ti *3d* character, thereby exhibiting resonant behaviour as the photon energy is swept through the Ti *2p* to unoccupied *3d* state resonance, as described in chapter 2 [15, 58, 59]. The spectra indicate that the interaction of the TiO_2(110) surface with water influences this region strongly, especially the valence band and the defect peak. The initial introduction of water into the system, equivalent to a RH of $4x10^{-5}$ %, results in a sharp decrease of the band gap peak intensity relative to that of the as-prepared surface. The intensity of this peak is only regained when the RH reaches 1%, which corresponds to a water coverage of about 1 ML [34]. As the RH inside the chamber is successively increased to the maximum value of 30 %, equal to a 3 ML water overlayer, the defect peak intensity is almost treble that of the as-prepared surface.

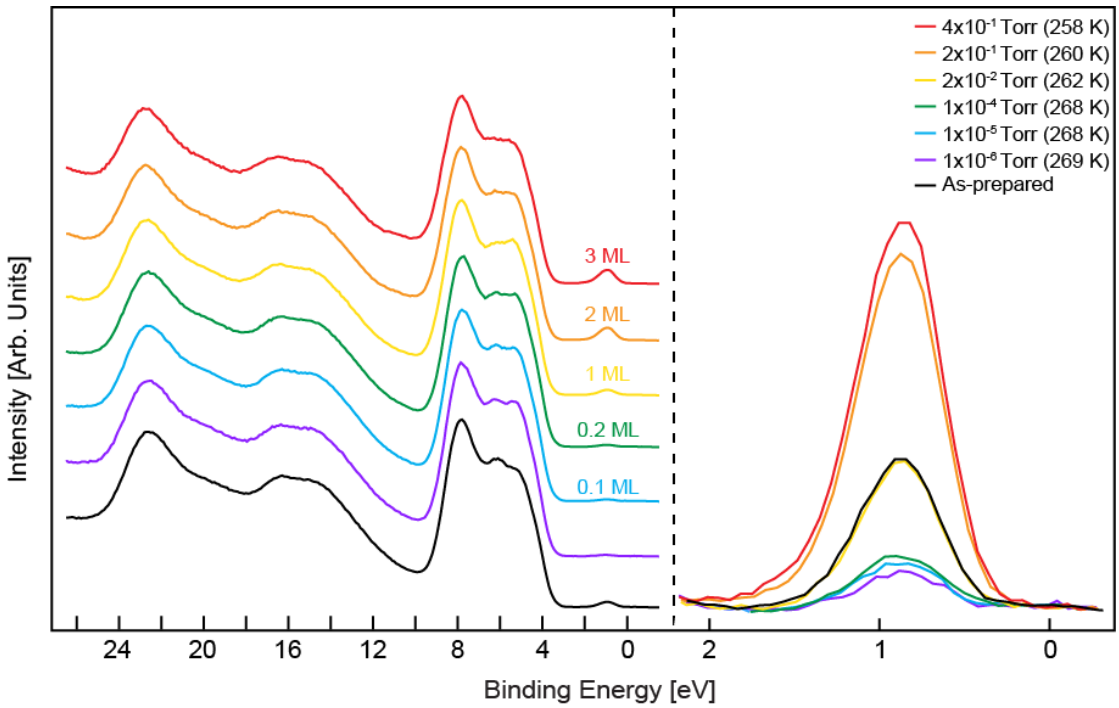

Figure 4.12 – X-ray photoelectron spectra of the valence band region of rutile TiO_2(110) before and after exposure to increasing values of water pressure, acquired on-resonance with the Ti *3d* electron state ($h\nu$ = 465.5 eV, E_{pass} = 10 eV, E_{step} = 0.1 eV). The spectra have been normalised to the O *2s* core-level peak at ~22.5 eV and are vertically offset for visualisation purposes (left). An amplified image of the rutile TiO_2(110) defect peak, located at around 0.9 eV, is also displayed (right). The method used to calculate the water layer thickness is described in Appendix A.

The current understanding is that the rutile TiO_2(110) band gap state is derived predominantly from O_b vacancies, with a minority contribution from defects such as Ti_{5c} interstitials and subsurface O vacancies [11,60]. In accordance to this, the band gap would not be expected to vary significantly when water was initially introduced up to a RH of 4×10^{-5} %, as this leads to the formation of hydroxyl species at the surface that are not deemed electronegative enough to withdraw charge from O_b vacancies or Ti_{5c} sites [61]. Therefore we assign the quenching of the defect peak to the possible co-adsorption of contaminants, e.g. oxygen, displaced from the inner chamber walls through water exposure. The transition from dissociative to molecular adsorption is thought to occur at a water coverage of around 0.25 ML. As the defect peak is observed to recover during the transition from 0.2 ML to 1 ML, we attribute this recovery to the dominance of H_2O molecules over OH species at the surface [39].

An additional experiment was performed to investigate the reversibility of the band gap state increase. This was achieved by initially recording a spectrum of an as-prepared sample (RH= $1x10^{-7}$ %), followed by another spectrum taken after the water had been introduced into the system (RH= 30 %). The chamber was then pumped down (RH= $4x10^{-5}$ %), and re-filled with water (RH= 15 %), with a spectrum recorded at both stages. The results, displayed in figure 4.13, show that the defect peak is intensified when the sample is exposed to water, and quenched in its absence. Furthermore, this process was observed to be completely reversible.

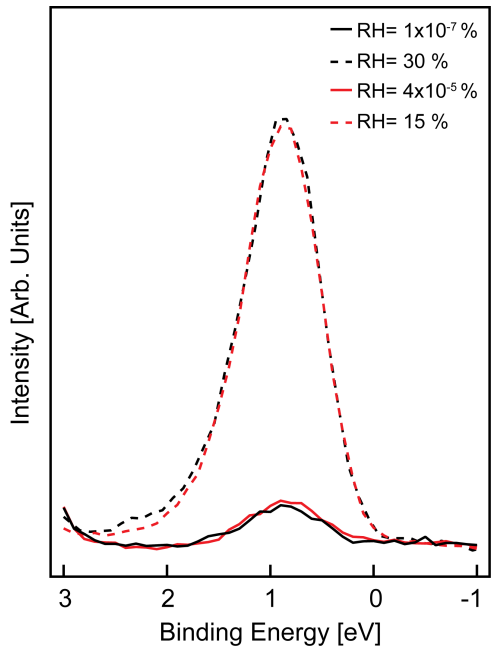

Figure 4.13 - X-ray photoelectron spectrum of the band gap state region of rutile TiO_2(110) ($h\nu$ = 465.5 eV, E_{pass} = 10 eV, E_{step} = 0.1 eV) acquired before (RH= $1x10^{-7}$ %) and after introducing water into the system (RH= 30 %). The chamber was then pumped down to a RH of around $4x10^{-5}$ % and refilled with water up to a RH of approximately 15%. The spectra have been normalised to the O *2s* core-level peak at ~22.5 eV (BE).

4.3.2 Oxygen

A series of experiments were performed in order to further our understanding of the effects of oxygen adsorption on the band gap state of rutile TiO_2(110). In the first experiment, approximately 0.2 Torr of ultra-pure water was administered into the system prior to the

gradual inlet of oxygen, up to a maximum oxygen partial pressure of ~0.4 Torr. The sample temperature was held at approximately 260 K, which provided the adequate conditions for the formation of water layers at the surface, as evidenced by the presence of the molecular water peak in the core-level O *1s* spectrum. The introduction of oxygen into the system resulted in an increase of this peak, which is a confirmation that water is indeed a reaction product of oxygen adsorption on the TiO_2(110) surface. Concerning the valence band region of the rutile TiO_2(110) sample, the introduction of roughly 0.1 Torr and 0.4 Torr of oxygen resulted in the quenching of the defect peak by ~10 % and ~40% respectively, as shown in figure 4.14.

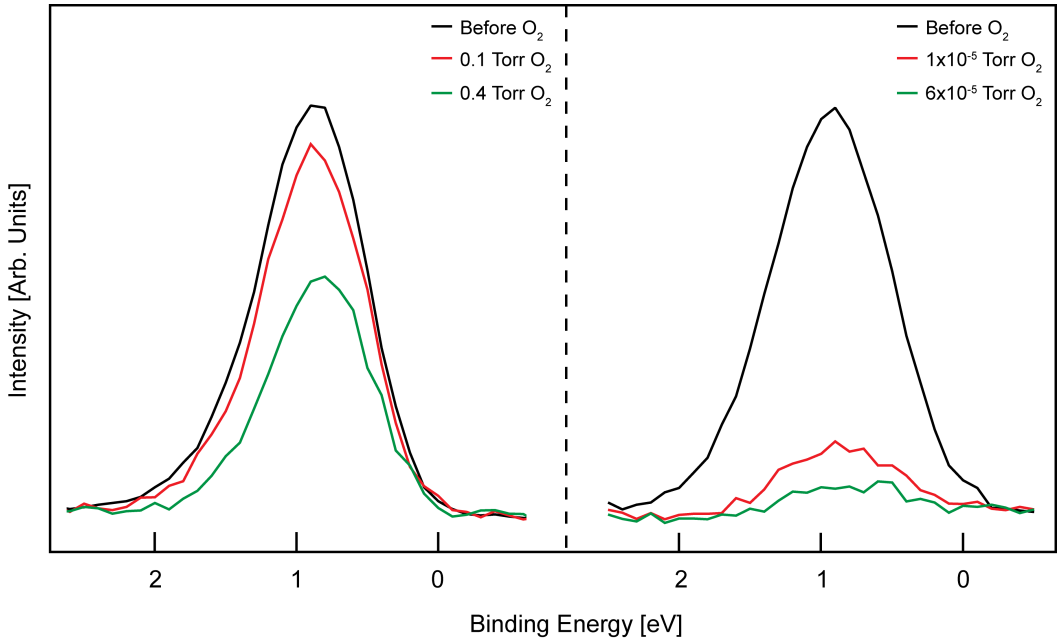

Figure 4.14 – X-ray photoelectron spectra of the band gap state of rutile TiO_2(110) acquired before and after oxygen exposure from a water covered surface (left) and a "clean" surface (right). A larger decrease of the defect peak intensity is observed for the "clean" surface as compared to the water-covered surface. The spectra were acquired using $h\nu$ = 465.5 eV, E_{pass} = 10 eV, and E_{step} = 0.1 eV.

In high relative humidity environments water molecules are hydrogen bonded to OH groups, consequently blocking the access of oxygen molecules to these OH groups and to scavenge the electrons associated with O_b vacancies. Nevertheless, water molecules are continuously adsorbed and desorbed from the surface, providing O_2 partial access to the surface and to the OH species. Therefore the electron scavenging reaction does indeed occur, albeit many

attempts by impinging O_2 molecules are unsuccessful when they encounter a water molecule hydrogen-bonded to the OH groups located at electron trap sites [17,62]. This can explain why we observe only a small decrease of the defect peak intensity. Another plausible explanation is that part of the band gap state intensity is derived from sub-surface vacancies and that the water overlayer blocks their availability to react with the impinging oxygen molecules; this hypothesis could be tested by performing an X-ray photoelectron diffraction experiment. In the second experiment the sample temperature was raised to 575 K, which ensured the absence of water molecules at the surface, i.e. a "clean" surface [38]. Oxygen was then gradually introduced into the system up to a partial pressure of 1×10^{-5} Torr and 6×10^{-5} Torr. Contrary to the water-covered surface, the introduction of oxygen into the system at this raised temperature resulted in a marked decrease of the defect peak, also shown in figure 4.14. This result can be explained along the lines of the previous experiment, where the O_2 molecules now have direct access to the O_b vacancies, OH groups and unoccupied Ti_{5c} sites on the surface, thus the scavenging process is more effective [17]. Note that it has been reported that complete removal of OH_b is not possible, therefore the complete extinction of the BGS is not possible [25,28,63].

4.3.3 Temperature

The effect of the temperature on the band gap state was examined for rutile TiO_2(110) that had been heated progressively from an initial temperature of ~265 K up to a temperature of ~480 K and ~575 K, following the evacuation of any gases from the system. As the temperature of the sample is raised, water molecules desorb from the surface and only hydroxyl species remain, as evidenced by the O *1s* and off-resonance valence band spectra presented in figure 4.15 and figure 4.16, respectively. The O*1s* spectrum acquired at ~480 K is displayed in figure 4.15, where the absence of water at the surface is substantiated by the nonexistence of a molecular water peak at ~533.5 eV. At the higher temperature of ~575 eV the spectrum composition is

identical, with only a small decrease of ~1% observed in the OH component. The CO_x component is reduced upon heating of the sample, but is not eliminated, as this would require the performance of a new preparation cycle.

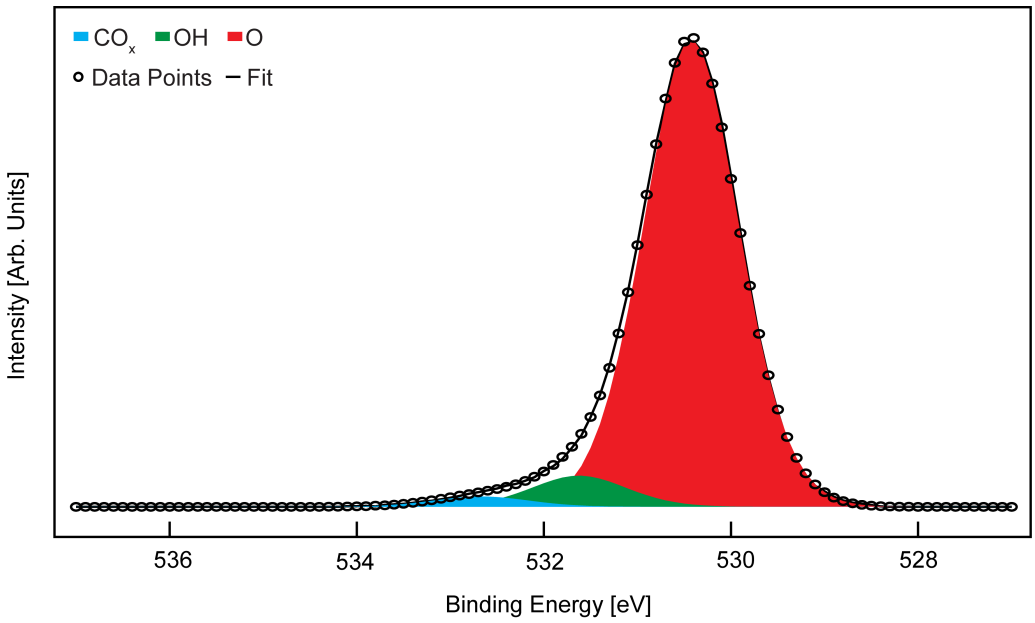

Figure 4.15 – Core-level O *1s* region photoelectron spectrum acquired at a temperature of 480 K ($h\nu$ = 700 eV, E_{pass} = 10 eV, E_{step} = 0.1 eV). The fitting was performed using three Gaussian-Lorentzian (30:70) type lineshapes, pertaining to CO_x, OH and bulk O contributions.

In the off-resonance spectra of the valence band region shown in figure 4.16, the disappearance of the characteristic $1b_1$, $1b_2$ and $3a_1$ molecular orbitals of water upon heating is observed, further corroborating the absence of water on the rutile TiO_2(110) surface. Again, the spectrum acquired at ~480 K and ~575 K are identical, therefore only the highest temperature and the as-prepared spectra are displayed. The on-resonance valence band spectra are displayed in figure 4.17. The main spectral changes befalling this region are observed in the band gap state peak, which is observed to increase in intensity as the sample temperature is raised. The Ti^{3+} component of the Ti *3p* core-level region also increases, which is a clear indication of the Ti *3d* nature of the band gap state. The increase of reduced Ti^{3+} species at the surface can be explained by the desorption of water molecules along with a large fraction of the hydroxyl species followed by the creation of O_b vacancies.

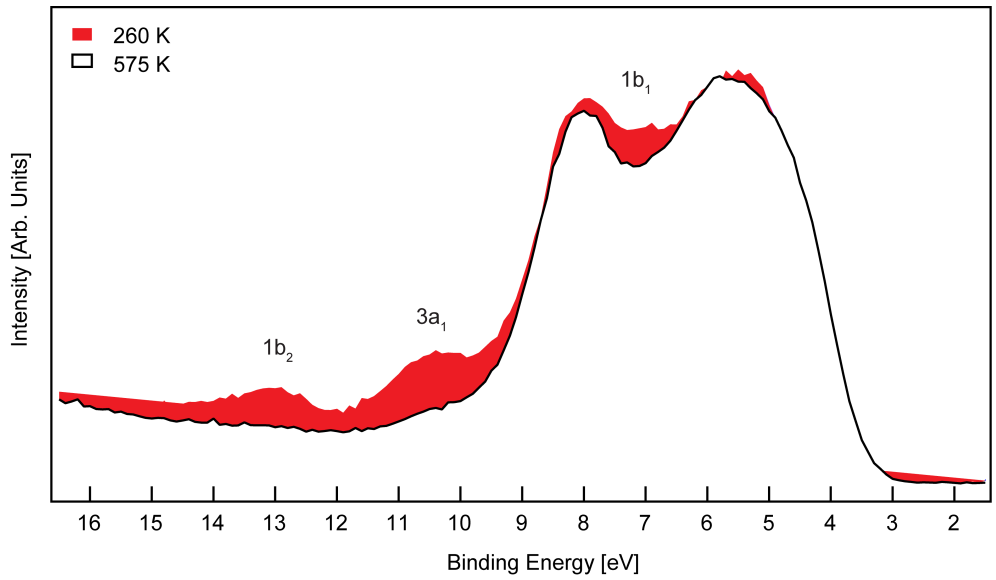

Figure 4.16 – X-ray photoelectron spectra of the valence band region of rutile TiO_2(110) acquired from an as-prepared sample at ~260 K and after heating to ~575 K, at an off-resonance energy ($h\nu$ = 455 eV, E_{pass} = 10 eV, E_{step} = 0.1 eV). The shaded area highlights the changes incurred by heating the sample to an elevated temperature, namely the loss of the features associated with the molecular orbitals of water centred at ~7.2 eV, ~10.3 eV and ~13 eV.

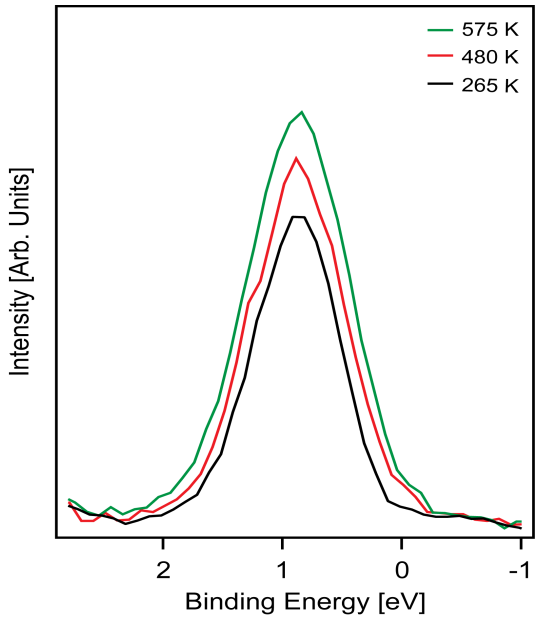

Figure 4.17 – X-ray photoelectron spectroscopy spectra of the band gap state region of rutile TiO_2(110) ($h\nu$ = 465.5 eV, E_{pass} = 10 eV, E_{step} = 0.1 eV). The intensity of the defect peak is observed to increase upon heating of the sample from ~265 K to ~480 K and ~575 K, indicating an increase of reduced Ti species at the surface.

4.4 Summary and Conclusions

The adsorption of water and oxygen, and the effect of temperature on rutile TiO_2(110) have been investigated using near ambient pressure photoelectron spectroscopy. Photoelectron spectra of the Ti *3p*, O *1s*, and valence band region, both on- and off-resonance with the Ti *3d* electron state, were acquired using photon energies of 455 eV, 700 eV, 465.5 eV, and 455 eV, respectively. Additionally, survey spectra were acquired throughout the course of the experiment to monitor contamination levels from carbon containing species.

The formation of a water overlayer on the as-prepared rutile TiO_2(110) surface resulted in the appearance of characteristic water peaks in the O *1s* and off-resonance valence band spectra. A peak pertaining to molecular water (~533.5 eV BE) is observed in the O *1s* region, and peaks ascribed to the $1b_1$ (~7.5 eV BE), $3a_1$ (~10.3 eV BE), and $1b_2$ (~13.2 eV BE) molecular orbitals of water develop in the off-resonance valence band region. The on-resonance valence band spectra also display changes upon water adsorption. Most intriguingly the band gap peak (~0.9 eV BE) is initially quenched upon the introduction of water in to the system, however when 1 ML coverage is reached it recovers, and at 3 ML the intensity is more than double the initial value. The current understanding cannot adequately explain the observed decrease of the band gap state intensity, as hydroxyl species are not deemed sufficiently electronegative to withdraw excess charge from the titania surface. As such, we postulate that this suppression may be due to the adsorption of contaminants that are dislodged from the inner chamber walls by the water, e.g. oxygen, which are capable of withdrawing charge from the Ti *3d* state. Charge transfer from the water molecules in the second and third layers into Ti *3d* states has been ruled out according to theoretical calculations performed on this system. Instead it has been suggested that the migration of Ti interstitials to the surface may be responsible. It was also observed that the variations of the intensity of the band gap state due to water adsorption are completely reversible.

The exposure of the rutile TiO_2(110) sample to oxygen resulted in the quenching of the defect peak. This result can be explained by the removal of the capping hydrogen from the hydroxyl species present at the surface, which leads to the formation of electron scavenging bridging oxygen atoms. Changes in the O *1s* spectra were also observed, namely the increase of the molecular water peak (~533.5 eV) owing to water being a reaction product of oxygen with hydroxyls, as described in the introduction section of this chapter.

The effect of temperature on the rutile TiO_2(110) sample was also investigated by heating the sample successively from ~265 K up to ~480 K and a maximum temperature of ~575 K. The O *1s* and off-resonance valence band spectra recorded at a temperature of ~480 K and ~575 K indicate the absence of water molecules and the presence of hydroxyls species at the surface. In addition, these elevated temperatures also result in the desorption of OH_b and in the formation of O_b vacancies, which adequately justifies the observed increase in the Ti *3d* band gap state [33,64,65].

A large amount of work is clearly still needed in order to gain a complete understanding of the band gap state of rutile TiO_2(110). We have made many attempts to reproduce the results regarding water adsorption on this surface, however due to instrumentation limitations of other systems, the same conditions were not achievable. To build on the work presented in this chapter, it would also be of interest to observe the effects of carbon containing oxygen species on band gap state of this substrate, as these are present in many catalytic systems. Future efforts should be focused on obtaining theoretical models in order to gain a better understanding of the interaction of water and other gases with the TiO_2(110) surface at an atomic level. Finally, it would also be interesting to repeat this experiment with an anatase TiO_2 substrate, as this is known to be catalytically more active that the rutile polymorph of titania.

References

[1] A. Fujishima, X. Zhang, D.A. Tryk, Surf Sci Rep 63 (2008) 515.

[2] Q. Mu, Y. Li, H. Wang, Q. Zhang, Journal of Colloid and Interface Science 365 (2012) 308.

[3] S. So, K. Lee, P. Schmuki, Phys. Status Solidi RRL 6 (2012) 169.

[4] J.P. Hewitt, Cosmetics and Toiletries (1999).

[5] Q. Xie, D. Deduytsche, M. Schaekers, M. Caymax, A. Delabie, X.-P. Qu, C. Detavernier, Appl. Phys. Lett. 97 (2010) 112905.

[6] D. Buso, M. Post, C. Cantalini, P. Mulvaney, A. Martucci, Adv. Funct. Mater. 18 (2008) 3843.

[7] A. Fujishima, K. Honda, Nature 238 (1972) 37.

[8] U. Diebold, Surf Sci Rep 48 (2003) 53.

[9] C. Lun Pang, R. Lindsay, G. Thornton, Chem. Soc. Rev. 37 (2008) 2328.

[10] M.A. Henderson, Surf Sci 419 (1999) 174.

[11] C.M. Yim, C.L. Pang, G. Thornton, Phys. Rev. Lett. 104 (2010) 036806.

[12] R.L. Kurtz, R. Stock-Bauer, T.E. Msdey, E. Román, Surf Sci (1989).

[13] V. Henrich, G. Dresselhaus, H. Zeiger, Phys. Rev. Lett. 36 (1976) 1335.

[14] W.S. Epling, C.H.F. Peden, M.A. Henderson, U. Diebold, Surf Sci 412-413 (1998) 333.

[15] A. Thomas, W. Flavell, A. Mallick, A. Kumarasinghe, D. Tsoutsou, N. Khan, C.

Chatwin, S. Rayner, G. Smith, R. Stockbauer, S. Warren, T. Johal, S. Patel, D. Holland, A. Taleb, F. Wiame, Phys. Rev. B 75 (2007) 035105.

[16] N.A. Deskins, R. Rousseau, M. Dupuis, J Phys Chem C 114 (2010) 5891.

[17] S. Wendt, P.T. Sprunger, E. Lira, G.K.H. Madsen, Z. Li, J.O. Hansen, J. Matthiesen, A. Blekinge-Rasmussen, E. Laegsgaard, B. Hammer, F. Besenbacher, Science 320 (2008) 1755.

[18] L.E. Walle, A. Borg, P. Uvdal, A. Sandell, Phys. Rev. B 86 (2012) 205415.

[19] N.G. Petrik, Z. Zhang, Y. Du, Z. Dohnálek, I. Lyubinetsky, G.A. Kimmel, J Phys Chem C 113 (2009) 12407.

[20] C. Di Valentin, G. Pacchioni, A. Selloni, Phys. Rev. Lett. 97 (2006) 166803.

[21] A.C.A. Papageorgiou, N.S.N. Beglitis, C.L.C. Pang, G.G. Teobaldi, G.G. Cabailh, Q.Q. Chen, A.J.A. Fisher, W.A.W. Hofer, G.G. Thornton, Proc Natl Acad Sci U S A 107 (2010) 2391.

[22] E. Finazzi, C. Di Valentin, G. Pacchioni, J Phys Chem C 113 (2009) 3382.

[23] Y. Du, N.A. Deskins, Z. Zhang, Z. Dohnálek, M. Dupuis, I. Lyubinetsky, J Phys Chem C 113 (2009) 666.

[24] C.L. Pang, R. Lindsay, G. Thornton, Chem. Rev. (2013) 130515130929008.

[25] Z. Zhang, Y. Du, N.G. Petrik, G.A. Kimmel, I. Lyubinetsky, Z. Dohnálek, J Phys Chem C 113 (2009) 1908.

[26] Y. Du, N.A. Deskins, Z. Zhang, Z. Dohnálek, M. Dupuis, I. Lyubinetsky, Phys. Chem. Chem. Phys. 12 (2010) 6337.

[27] Y. Du, Z. Dohnalek, I. Lyubinetsky, J Phys Chem C 112 (2008) 2649.

[28] M.A. Henderson, W.S. Epling, C.L. Perkins, C.H.F. Peden, U. Diebold, J. Phys. Chem.

B 103 (1999) 5328.

[29] E. Lira, P. Huo, J.Ø. Hansen, F. Rieboldt, R. Bechstein, Y. Wei, R. Streber, S. Porsgaard, Z. Li, E. Lægsgaard, S. Wendt, F. Besenbacher, Catalysis Today 182 (2012) 25.

[30] P.J.D. Lindan, N.M. Harrison, Phys. Rev. Lett. 80 (1998) 762.

[31] S. Wendt, J. Matthiesen, R. Schaub, E. Vestergaard, E. Laegsgaard, F. Besenbacher, B. Hammer, Phys. Rev. Lett. 96 (2006) 066107.

[32] G. Teobaldi, W.A. Hofer, O. Bikondoa, C.L. Pang, G. Cabailh, G. Thornton, Chemical Physics Letters 437 (2007) 73.

[33] M.B. Hugenschmidt, L. Gamble, C.T. Campbell, Surf Sci 302 (1994) 329.

[34] G. Ketteler, S. Yamamoto, H. Bluhm, K. Andersson, D.E. Starr, D.F. Ogletree, H. Ogasawara, A. Nilsson, M. Salmeron, J Phys Chem C 111 (2007) 8278.

[35] M. Henderson, Surf Sci Rep 46 (2002) 1.

[36] R. Schaub, P. Thostrup, N. Lopez, E. Laegsgaard, I. STENSGAARD, J.K. Nørskov, F. Besenbacher, Phys. Rev. Lett. 87 (2001) 266104.

[37] S. Yamamoto, H. Bluhm, K. Andersson, G. Ketteler, H. Ogasawara, M. Salmeron, A. Nilsson, J. Phys.: Condens. Matter 20 (2008) 184025.

[38] L.E. Walle, A. Borg, P. Uvdal, A. Sandell, Phys. Rev. B 80 (2009) 235436.

[39] M. Amft, L.E. Walle, D. Ragazzon, A. Borg, P. Uvdal, N.V. Skorodumova, A. Sandell, J Phys Chem C 117 (2013) 17078.

[40] P. Lindan, C. Zhang, Phys. Rev. B 72 (2005) 075439.

[41] W. Zhang, J. Yang, Y. Luo, S. Monti, V. Carravetta, J. Chem. Phys. 129 (2008) 064703.

[42] D.A. Duncan, F. Allegretti, D.P. Woodruff, Phys. Rev. B (2012).

[43] U. Martinez, L.B. Vilhelmsen, H.H. Kristoffersen, J. Stausholm-Møller, B. Hammer, Phys. Rev. B 84 (2011) 205434.

[44] U. Martinez, J.O. Hansen, E. Lira, H.H. Kristoffersen, P. Huo, R. Bechstein, E. Laegsgaard, F. Besenbacher, B. Hammer, S. Wendt, Phys. Rev. Lett. 109 (2012) 155501.

[45] H.H. Kristoffersen, J.O. Hansen, U. Martinez, Y.Y. Wei, J. Matthiesen, R. Streber, R. Bechstein, E. Laegsgaard, F. Besenbacher, B. Hammer, S. Wendt, Phys. Rev. Lett. 110 (2013) 146101.

[46] A.L. Buck, Journal of Applied Meteorology 20 (1981) 1527.

[47] P. Hardman, N. Prakash, C. Muryn, G. Raikar, A. Thomas, A. Prime, G. Thornton, R. Blake, Phys. Rev., B Condens. Matter 47 (1993) 16056.

[48] A. Howard, D. Clark, C. Mitchell, R.G. Egdell, V.R. Dhanak, Surf Sci 518 (2002) 210.

[49] D.A. Shirley, Phys. Rev. B 5 (1972) 4709.

[50] J.E. Castle, H. Chapman-Kpodo, A. Proctor, Journal of Electron Spectroscopy and Related Phenomena 106 (2000) 65.

[51] K. Andersson, G. Ketteler, H. Bluhm, S. Yamamoto, H. Ogasawara, L.G.M. Pettersson, M. Salmeron, A. Nilsson, J Phys Chem C 111 (2007) 14493.

[52] L.E. Walle, A. Borg, E.M.J. Johansson, S. Plogmaker, H. Rensmo, P. Uvdal, A. Sandell, The Journal of Physical Chemistry C 115 (2011) 9545.

[53] P.J. Cumpson, M.P. Seah, Surf. Interface Anal. 25 (1997) 430.

[54] I. Brookes, C. Muryn, G. Thornton, Phys. Rev. Lett. 87 (2001) 266103.

[55] P.A. Thiel, T.E. Madey, Surf Sci Rep 7 (1987) 211.

[56] Y. Tezuka, S. Shin, T. Uozumi, A. KOTANI, Journal of the Physical Society of Japan 66 (1997) 3153.

[57] M. Scrocco, Chemical Physics Letters 61 (1979) 453.

[58] T. Caruso, C. Lenardi, R.G. Agostino, M. Amati, G. Bongiorno, T. Mazza, A. Policicchio, V. Formoso, E. Maccallini, E. Colavita, G. Chiarello, P. Finetti, F. Šutara, T. Skala, P. Piseri, K.C. Prince, P. Milani, J. Chem. Phys. 128 (2008) 094704.

[59] U. Diebold, H.-S. Tao, N. Shinn, T. Madey, Phys. Rev. B 50 (1994) 14474.

[60] K.W. Goodman, V.E. Henrich, Phys. Rev., B Condens. Matter 50 (1994) 10450.

[61] Z.-T. Wang, J.C. Garcia, N.A. Deskins, I. Lyubinetsky, Phys. Rev. B 92 (2015) 081402.

[62] M.A. Henderson, W.S. Epling, C.H.F. Peden, C.L. Perkins, J. Phys. Chem. B 107 (2003) 534.

[63] U. Diebold, S.-C. Li, M. Schmid, Annu. Rev. Phys. Chem. 61 (2010) 129.

[64] G. Lu, A. Linsebigler, J.T. Yates Jr, J. Phys. Chem. 98 (1994) 11733.

[65] Y. Namai, O. Matsuoka, J. Phys. Chem. B 109 (2005) 23948.

APPENDIX A

The thickness of the water layer on rutile TiO_2(110) can be estimated from the Ti *3p* photoemission signal, before and after the introduction of water vapour into the chamber according to Equation A1,

$$\frac{I_{\mathrm{Ti}}}{I_{0,\mathrm{Ti}}} = \exp\left(\frac{d_{\mathrm{w}}^{\mathrm{L}}}{\lambda_{\mathrm{w}}^{\mathrm{L}}\cos\theta}\right)\exp\left(-\frac{d_{\mathrm{w}}^{\mathrm{G}}}{\lambda_{\mathrm{w}}^{\mathrm{G}}}\right), \tag{A1}$$

where $I_{0,\mathrm{Ti}}$ is the Ti *3p* signal intensity for the as-prepared sample, I_{Ti} the Ti *3p* signal intensity for the water dosed sample, $\lambda_{\mathrm{w}}^{\mathrm{L}}$ the inelastic mean free path of an electron in liquid water, $\lambda_{\mathrm{w}}^{\mathrm{G}}$ the inelastic mean free path of an electron in gaseous water, θ the angle between the surface normal and the analyser axis (45°), $d_{\mathrm{w}}^{\mathrm{L}}$ the thickness of the liquid water layer, and $d_{\mathrm{w}}^{\mathrm{G}}$ the effective thickness of the water vapour that the electrons traverse before reaching the low vacuum conditions of the first differential pumping stage, which is approximately the distance between the sample and the aperture of the first differential pumping stage, i.e. ~200 μm [1]. The two terms on the right hand side can be combined under the assumption of a hypothetical liquid layer, i.e. without water vapour, and Equation A1 is simplified to,

$$\frac{I_{\mathrm{Ti}}}{I_{0,\mathrm{Ti}}} = \exp\left(-\frac{d_{\mathrm{w}}^{\mathrm{L_{eq}}}}{\lambda_{\mathrm{w}}^{\mathrm{L}}\cos\theta}\right) \tag{A2}$$

with

$$d_{\mathrm{w}}^{\mathrm{L_{eq}}} = d_{\mathrm{w}}^{\mathrm{L}} + d_{\mathrm{w}}^{\mathrm{G}}\frac{\lambda_{\mathrm{w}}^{\mathrm{L}}}{\lambda_{\mathrm{w}}^{\mathrm{G}}}\cos\theta. \tag{A3}$$

The ratio of the inelastic mean free paths for water vapour and liquid water is approximately equal to the inverse of the densities of the two. Let us know consider the highest partial pressure of water attempted in our experiment (0.4 Torr, 258 K), where a ratio of 1.7×10^{-6} is obtained, as shown below.

$$\frac{\lambda_{\mathrm{w}}^{\mathrm{L}}}{\lambda_{\mathrm{w}}^{\mathrm{G}}} \approx \frac{\rho_{\mathrm{w}}^{\mathrm{G}}}{\rho_{\mathrm{w}}^{\mathrm{L}}} = \frac{1.7\ \mathrm{g.m^{-3}}}{1000\ \mathrm{kg.m^{-3}}} = 1.7{\times}10^{-6}$$

The substitution of the constants† for their values in Equation A2 is displayed below,

$$d_{\mathrm{w}}^{\mathrm{Leq}} = -\ln\left(\frac{94844.4}{183940.8}\right)(2)(0.707)$$

which yields a value of ~1 nm for $d_{\mathrm{w}}^{\mathrm{Leq}}$. The thickness of the water overlayer may now be calculated by applying Equation A3,

$$d_{\mathrm{w}}^{\mathrm{L}} = d_{\mathrm{w}}^{\mathrm{Leq}} - (200\mu\mathrm{m})(1.7{\times}10^{-6})(0.707) = 0.75\ \mathrm{nm}.$$

Lastly, if we take the value of 1 ML of water to be equal to 0.25 nm, the maximum water layer thickness achieved in our experiment was equivalent to 3 ML.

† The inelastic mean free path of an electron in liquid water was calculated using the *NIST Inelastic Mean Free Path Database (version 1.2)*, for a photon energy of 465.5 eV.

References

[1] O. Karslıoğlu, S. Nemšák, I. Zegkinoglou, A. Shavorskiy, M. Hartl, F. Salmassi, E.M. Gullikson, M.L. Ng, C. Rameshan, B. Rude, D. Bianculli, A.A. Cordones, S. Axnanda, E.J. Crumlin, P.N. Ross, C.M. Schneider, Z. Hussain, Z. Liu, C.S. Fadley, H. Bluhm, Faraday Discuss. 180 (2015) 35.

CHAPTER 5

$\sqrt{3} \times \sqrt{3}$ $CeO_2(111)$ ULTRATHIN FILMS

Abstract

Ultrathin films of $CeO_2(111)$, or ceria, were grown on Pt(111) and Rh(111) substrates using the post-oxidation method that involves the oxidation of surface Pt/Ce or Rh/Ce alloys with molecular oxygen. This recipe resulted in the formation of high quality $CeO_2(111)$ islands, on which atomically resolved Scanning Tunnelling Microscopy (STM) images were obtained. The STM images were recorded in both filled and empty state modes, and a $\sqrt{3} \times \sqrt{3}$ surface reconstruction, with a number of defects and adsorbates, was observed. These films were further investigated using Auger Electron Spectroscopy (AES) and Low Energy Electron Diffraction (LEED). In addition, the behaviour and preferential adsorption sites of individual gold atoms at room temperature on ultrathin $CeO_2(111)$ films were investigated with STM. The atomic resolution images obtained of the ceria surface with gold adatoms atop suggest that the gold has no preferential adsorption site and is immobile on the ceria surface at room temperature.

5.1 Introduction

Ceria, cerium dioxide or CeO_2 is a rare earth oxide that serves a number of purposes in catalysis, including exhaust gas purification in automotive catalytic converters, the removal of organics from wastewater, as an additive for combustion catalysts and processes, in fuel cell technology, and as gas sensors, to name but a few [1]. The underlying property behind the outstanding performance of ceria in catalysis is its remarkable ability to store and release oxygen owing to the reversible redox ability of the Ce^{4+}/Ce^{3+} pair, as well as the promotion of noble metal activity [2,3]. This redox ability is linked to the high mobility of oxygen within the ceria lattice, which is reliant upon the defect structure of this oxide, especially oxygen vacancies that are key to the reactivity of this oxide and metal oxides in general. The degree of the oxygen ion mobility in the ceria lattice is associated with the size, dispersion and abundance of oxygen vacancy defects [4]. In addition, these vacancies have also been thought to be important in the binding of metal nanoparticles to the metal oxide surface [5-8]. The (111) surface of CeO_2 is the thermodynamically most stable and is thought to be a very commonly exposed surface in commercial catalysts, thus this was the chosen surface for the work presented in this chapter [4].

Bulk gold is chemically inert and is generally regarded as a poor catalyst. However, single-atoms and small clusters of gold have been demonstrated to be highly active for a number of catalytic reactions, even at low temperatures. In particular gold nanoparticles supported on ceria acts as a highly active catalyst for the low temperature water-gas-shift reaction, widely used for hydrogen production whereby a reaction between H_2O and CO produces H and CO_2 [5]. There have been numerous theoretical [6,7,9,10] and experimental [9,11-16] surface science studies investigating the $Au/CeO_2(111)$ system, however the precise origin of the catalytic activity of gold still remains a highly debated topic. Nonetheless, there is a general consensus that the dimension and shape of the nanoparticles, along with the surface properties of the oxide support, are key underlying factors [17,18].

Scanning tunnelling microscopy (STM) is a very valuable technique in surface science studies, such as the Au/CeO_2(111) investigation reported here, as it allows for the direct imaging of individual point defects and adsorbates with atomic resolution. Stoichiometric CeO_2 exhibits a rather large band gap (~6 eV), thus generating experimental constraints regarding the application of electron-based techniques such as STM due to the occurrence of sample charging. To overcome this limitation, the STM study must either be performed at high temperatures (>575 K) or an ultrathin metal oxide film must be grown on a conducting substrate if the study is to be carried out at room temperature or lower. A number of metal supports have proved successful in the growth of CeO_2(111), for example Rh(111) [19-21], Cu(111) [22,23], Re(0001) [24,25], and Pt(111) [26-29]. Studies have shown that the properties of ultrathin ceria films mimic those of the native bulk oxide very closely, including the existence of point defects such as surface and sub-surface oxygen vacancies.

The starting point for this study is the preparation of an ultrathin ceria film on a Pt(111) substrate, and later on Rh(111), via a post-oxidative method. The prepared CeO_2(111) film is then analysed by LEED and AES, and is imaged using STM. Subsequently one of the ceria islands is selected and mapped, whereby atomically resolved images of the entire island surface are acquired and characteristic point defects are registered. The comparison of images of the same area of the ceria surface, acquired before and after the *in situ* dosing of gold via physical vapour deposition (PVD), allows the identification of the adsorption sites of the Au adatoms and the analysis of their behaviour.

5.2 Experimental Procedure

The experiments were carried out on a commercial *Omicron* VT-STM operated at room temperature. The STM is situated in an ultra high vacuum (UHV) system with a base pressure of 1×10^{-10} mbar. STM images were recorded in constant current mode with either W or PtIr

(*Unisoku Scientific Instruments*) tips. The tungsten tips were prepared by electrochemically etching W wire (*Advent*) in 2M NaOH solution, followed by degassing at ~500 K in UHV, whereas the PtIr tips were commercially machined. The conditioning of the tip apex was achieved by applying voltage pulses and high bias scans, allowing for the stable tunnelling essential for the attainment of atomically resolved images.

The Pt(111) and Rh(111) crystals were prepared by multiple cycles of Argon ion sputtering (1.5 keV, 10 min, 10 μA) and annealing at ~1100 K in UHV until a well-ordered (1×1) LEED pattern was observed and impurities were below the detection level in AES. In the event of minor carbon contamination, cycles of annealing at ~1000 K in 1×10^{-6} mbar O_2 were also performed.

The literature on this subject details two different approaches for producing high-quality ceria ultrathin films, either by post-oxidation [26] or reactive deposition [30]. In the post-oxidation method used in the experiments, cerium metal (*Alfa Aesar*, 99.9%) was evaporated onto a clean Pt(111) or Rh(111) substrate at room temperature in UHV via physical vapour deposition (PVD) from an electron beam evaporator, and subsequently annealed in UHV for about 3 min, leading to the formation of Pt_xCe or Rh_xCe_y surface alloys [19,31]. This was followed by a further anneal at ~1050 K in a partial pressure of 5×10^{-6} mbar O_2 for a duration of 10 to 60 minutes, which resulted in the oxidation of these alloys and ultimately a well-ordered CeO_2(111) film. Following this, the ceria-dosed sample was allowed to cool for 10 to 30 min in the same atmosphere of O_2. The reactive deposition method involved the deposition of the cerium metal via PVD in 1×10^{-6} mbar O_2, while the Pt(111) or Rh(111) substrate was held at a temperature of ~1000 K. The temperatures and durations of the annealing cycles of the aforementioned procedures were varied to determine the optimal growth conditions for the ceria ultrathin films. The temperatures were monitored using a *Minolta* infrared pyrometer.

The deposition methods attempted both yielded high-quality ceria ultrathin films with (1.37 × 1.37) LEED patterns relative to Pt(111)(1×1) and Rh(111)(1×1). STM images show that these ceria films adopt the form of large, atomically flat islands of CeO_2(111), as opposed to a continuous film. In this work, one ceria monolayer (ML) is defined as one O-Ce-O trilayer unit with a thickness of 0.31 nm, and all coverages are calculated using the film thickness and the island area measured by STM. Gold (Advent RM, 99.9%) was deposited onto these ultrathin CeO_2(111) films at room temperature via PVD from a commercial evaporator (Compact Vapour Source, J. Taylor & C. Nicklin). The doser was calibrated using STM images of the Au covered Pt(111) surface, and the purity of the deposited gold was verified by AES. The coverage of the gold nanoparticles is defined in terms of that of the Au(111) surface, by which one ML corresponds to 1.4×10^{-15} atoms cm^{-2} [11].

5.3 Results and Discussion

5.3.1 Pt(111) and Rh(111) Substrate

STM scans of the Rh(111) and Pt(111) substrates show that the preparation method chosen for the crystals yields surfaces composed of atomically flat (111) terraces separated by well-defined monatomic steps, and a sharp (1×1) LEED pattern, as displayed in Figure 5.1. A line scan analysis of the STM images reveals a step height of ~0.23 nm for Pt(111) and ~0.22 nm for Rh(111), which is good agreement with the values reported in the literature [32,33]. In addition to flat terraces, sometimes hill-like structures and screw dislocations are observed on both the Rh(111) and Pt(111) substrates, such as the STM image of the clean Rh(111) surface presented in Figure 5.1. A recent study has identified these step-edges and screw dislocations as the preferential nucleation sites for the ceria film growth [34].

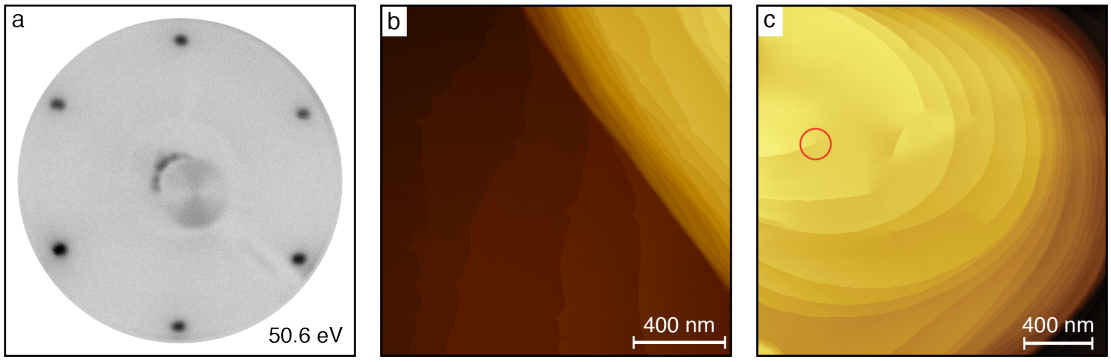

Figure 5.1 – STM images and a LEED pattern of clean Pt(111) and Rh(111) surfaces. a) Pt(111) (1×1) LEED image acquired at an energy of 50.6 eV, b) STM image of the clean Pt(111) terraces (1500 × 1500 nm^2, V_s = +2.2 V, I_t = 0.1 nA), and c) STM image of a hill feature on clean Rh(111) where multiple screw dislocations are visible, one of which is marked with a red circle (2000 × 2000 nm^2, V_s = +0.5 V, I_t = 0.2 nA).

5.3.2 CeO_2(111) Ultrathin Films on Pt(111) and Rh(111)

As described in the experimental section of this chapter, the ultrathin ceria films are grown using a post-oxidative method that involves the oxidation of intermediate Pt_xCe or Rh_xCe_y alloys. A typical LEED pattern of such alloys is exhibited in figure 5.2, where the typical (2 × 2) and (2 × 2)R30° spots are clearly visible [20]. Although it is not possible to monitor the oxidation state of the alloys *in situ*, examination of the STM images allows a number of conclusions to be drawn. In STM, these alloy phases are identifiable by their characteristic Moiré patterns. Figure 5.2 also displays three distinct phases, labelled as I, II and III. By comparison of these results with those reported in the literature phase I can be assigned to an alloy composed of Pt_5Ce layers terminated by a layer of Pt_2Ce, phase II to an alloy also composed of Pt_5Ce layers but with a contracted and ~30° rotated terminating Pt_2Ce overlayer, and phase III to an Pt terminated Pt_5Ce alloy [35,36].

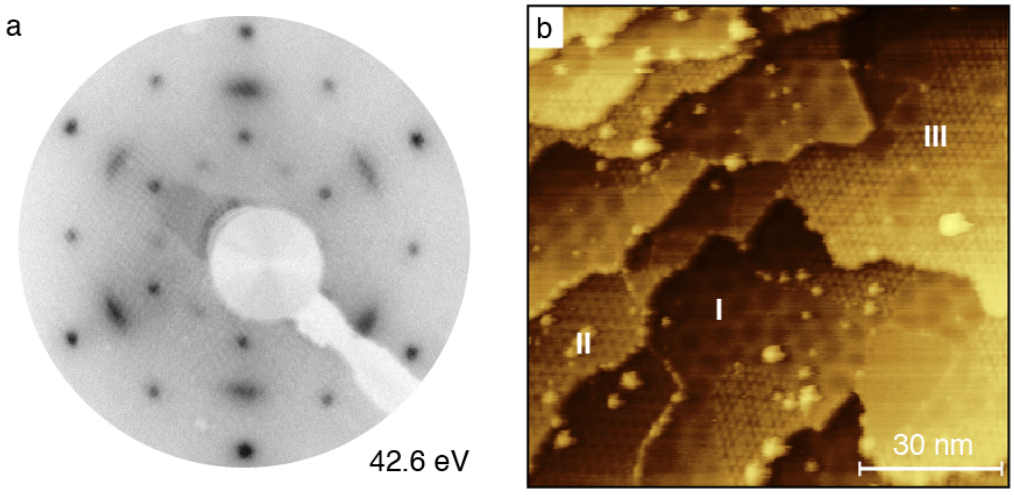

Figure 5.2 – STM and LEED images of Pt_xCe surface alloys formed by annealing the ceria metal on a Pt(111) substrate in UHV. a) Image of a Pt_xCe alloy LEED pattern acquired at an energy of 42.6 eV, b) Image showing three different surface alloy moiré patterns, labelled as I, II or III, composed of Pt_5Ce layers with either a Pt_2Ce, rotated Pt_2Ce, or Pt overlayer, respectively (100 × 100 nm^2, V_s = +1.70 V, I_t = 0.10 nA).

The subsequent annealing of the Pt_xCe and Rh_xCe_y surface alloys in partial pressure of molecular oxygen resulted in the formation of ceria ultrathin films with a characteristic LEED pattern displaying a low background and sharp reflexes pertaining to either the Rh(111)(1× 1) or Pt(111)(1 × 1) substrate and the CeO_2(111)(1.4 × 1.4) film, such as the one displayed in figure 5.3. In this particular image the LEED pattern pertaining to the $\sqrt{3} \times \sqrt{3}$ ceria lattice is also observed, however its presence is time-dependant as it is observed to degrade very quickly with electron bombardment by the LEED beam. It is important to note that 1:1.4 is the ideal ratio of the lattice spacings, i.e. the single crystal parameters, however the ratio of the ceria thin films reported in fact varies between 1:1.37 and 1:1.39. This deviation from the ideal ratio of the lattice spacings is a consequence of the large lattice mismatch between the Pt(111) or Rh(111) substrate and the CeO_2(111) film, which gives rise to a strain-induced contraction of the ceria film lattice in relation to the single crystal [37].

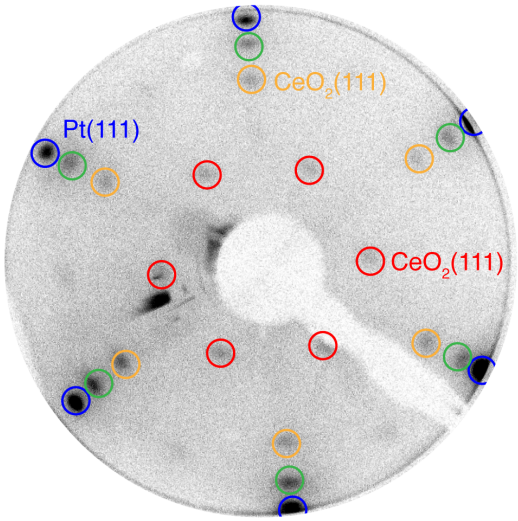

Figure 5.3 – Low energy electron diffraction pattern of a ceria ultrathin film grown on a Pt(111) substrate, displaying a low intensity background and sharp reflexes from Pt(111)(1 × 1), CeO_2(111)(1.4 × 1.4), $CeO_2(\sqrt{3} \times \sqrt{3})$, and a double diffraction spot, highlighted by blue, yellow, red and green circles, respectively. This LEED image was acquired at an energy of 39.1 eV.

A selection of large-area STM images of ceria ultrathin films grown via the post oxidation of intermediate Pt_xCe and Rh_xCe_y surface alloys are shown in figure 5.4 and figure 5.5, respectively. The STM images in these figures show the variety of different ceria films that can be obtained by simply varying preparation factors, such as oxidation temperature. It was observed that when the anneal time was insufficient, the resultant CeO_2(111) thin films were more film-like (Figure 5.4a and Figure 5.5a-c), as opposed to longer anneal times that yielded defined 3D ceria islands, adhering to a Volmer–Weber growth mode [38], which preferentially nucleate at step edges (Figure 5.4b-d and Figure 5.5d). The oxide islands are oxygen terminated and their apparent thickness is between 0.3 nm to 1.2 nm, consistent with one to four O-Ce-O trilayers, respectively. Auger electron spectroscopy was used to verify the cleanliness of the ceria films, typical spectra are also displayed in Figure 5.4e and Figure 5.5e, pertaining to CeO_2(111) on Pt(111) and Rh(111), respectively. The spectra are plotted in derivative mode using RFA detection, and peaks pertaining to the substrate (Rh MNN or Pt LMM) and ceria thin film (Ce LMM and O KLL) are clearly visible. AES can also be used to estimate film-thickness, however due to the poor signal-to-noise ratio, this was not possible in this case [39].

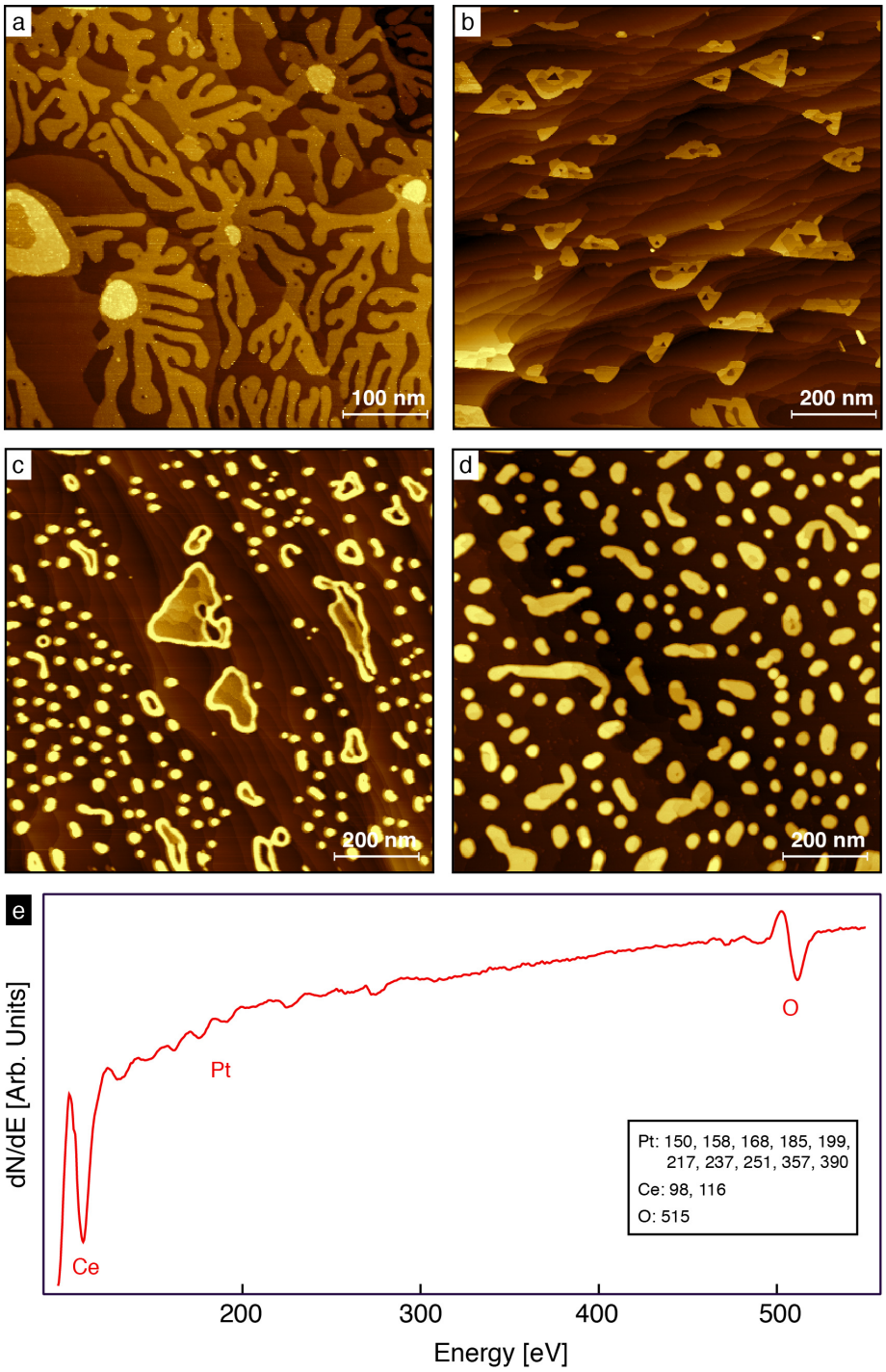

Figure 5.4 – STM images of ultrathin $CeO_2(111)$ films prepared by the post oxidation of Pt_xCe surface alloys in molecular oxygen. STM image of a) the initial ceria island formation (500 × 500 nm^2, V_s = -3.2 V, I_t = 0.05 nA), b) the ceria film obtained after the post-oxidation of the film shown in image a) (500 × 500 nm^2, V_s = -3.2 V, I_t = 0.05 nA), and c) the ceria film obtained after a further post-oxidation of the film shown in image b) (1000 × 1000 nm^2, V_s = -3.5 V, I_t = 0.05 nA). The $CeO_2(111)$ islands can appear with geometric shapes, such as in b), or more rounded, as is the case of the film displayed in d) (1000 × 1000 nm^2, V_s = -4.0 V, I_t = 0.05 nA). e) Typical derivative Auger electron spectrum of a $CeO_2(111)$ film on a Pt(111) substrate.

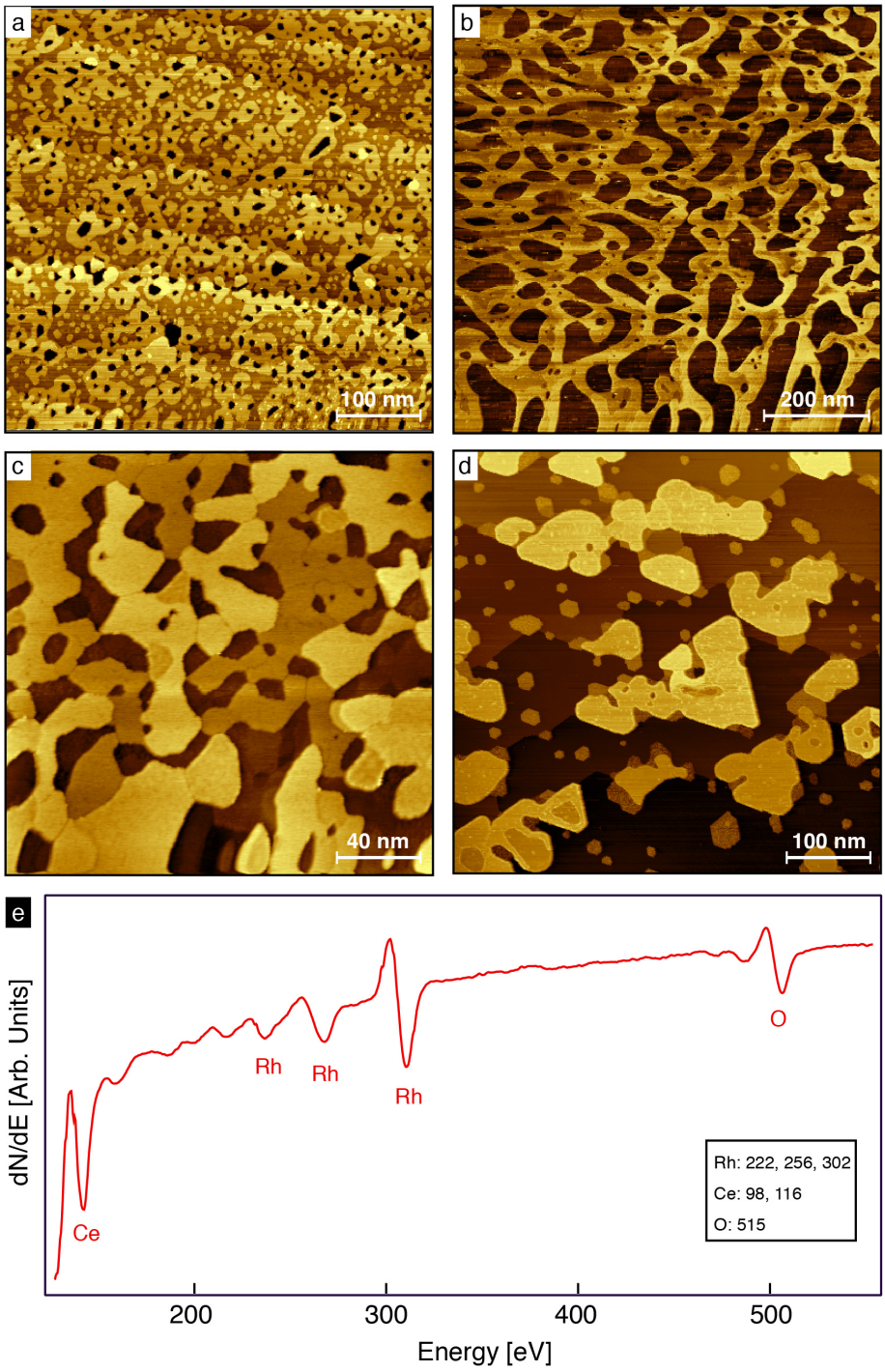

Figure 5.5 – STM images of ultrathin $CeO_2(111)$ films prepared by the post oxidation of intermediate Rh_xCe_y surface alloys in molecular oxygen. STM image of a) the initial growth stage of a ceria film (500 × 500 nm^2, V_s = -3.2 V, I_t = 0.05 nA), b) the film displayed in a) after a further anneal in a partial pressure of oxygen (500 × 500 nm^2, V_s = -3.2 V, I_t = 0.10 nA), c) the early formation of $CeO_2(111)$ islands (200 × 200 nm^2, V_s = -3.2 V, I_t = 0.10 nA), and d) fully-formed islands of ceria on a Rh(111) substrate (500 × 500 nm^2, V_s = -3.2 V, I_t = 0.05 nA). e) Typical derivative Auger electron spectrum of a $CeO_2(111)$ film on Rh(111).

5.3.3 CeO_2(111) Defect and Adsorbate Structure

The study of the surface defect structure of CeO_2(111) is essential for the understanding the interaction mechanism of this oxide with adsorbate molecules and metal adatoms, such as gold. figure 5.6a shows an STM image displaying a 0.6 nm thick CeO_2(111) island grown via the post-oxidation method that exhibits dark lines atop the island.

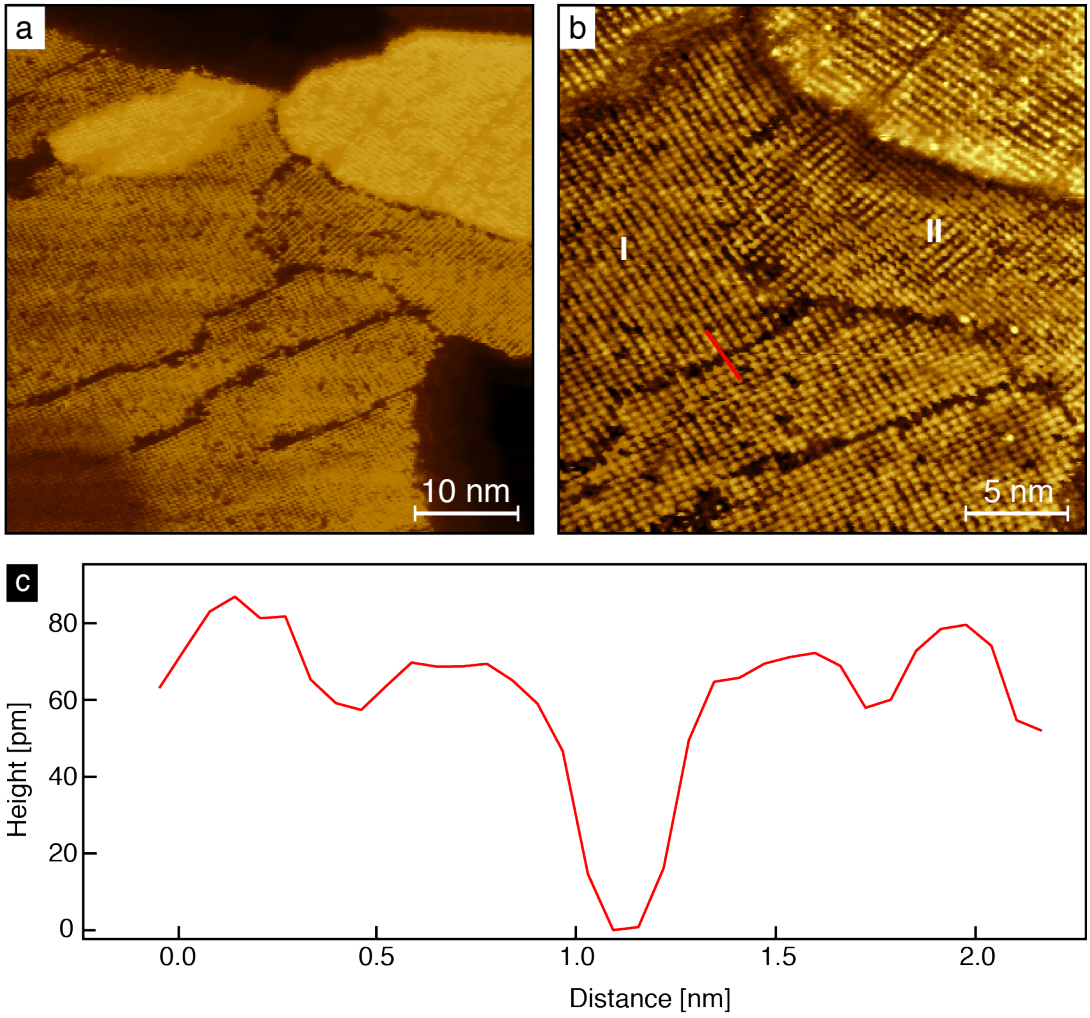

Figure 5.6 – STM images and line profile of a domain boundary feature observed on ceria ultrathin films grown on Rh(111). a) STM image (50 × 50 nm^2, V_s = -3.2 V, I_t = 0.05 nA) of a portion of a disordered CeO_2(111) island with multiple dark features evident at the surface, b) atomically resolved STM image (500 × 500 nm^2, -3.2 V, 0.05 nA) of the centre section of image a) with the domain boundaries clearly visible, and c) line profile across the highlighted domain boundary of image b.

Closer inspection of these features is possible in the atomically resolved image presented in figure 5.6b. A line profile (red line) across one of the dark lines indicates that this feature is approximately 0.5 nm wide and 60 pm deep.

This high resolution image also allows us to observe two distinct domains with different orientations, labelled I and II, which display a rotation of their lattices of about 90° with respect to each other. Such depressions can be assigned to domain boundaries that result from the large lattice mismatch between the ceria film and the Rh(111) substrate and have been reported in the literature for CeO_2(111) films on various metal substrates, including Rh(111) [40], Ru(0001) [41], and Pt(111) [42]. An alternative explanation is that these depressions originate from the coalescence of various islands of ceria, which is promoted by the post-oxidation of the intermediate Rh_xCe_y surface alloys. Figures 5.6a and 5.6b were both acquired at a negative sample bias, which allows tunnelling from the occupied states of the ceria into the tip. These filled states are dominated by contributions from O *2p* orbitals and therefore the surface oxygen atoms appear with a bright contrast [43].

Figure 5.7a displays a large-area STM image of a 1.5 MLE ceria ultrathin film with the underlying Pt(111) substrate still visible in between the CeO_2(111) islands, which appear as discrete quasi-hexagonal islands that are evenly distributed across the substrate and are found to nucleate preferentially along the Pt(111) step edges. The apparent height of these islands is about 2.1 nm, corresponding to a thickness of seven O-Ce-O trilayers, and display lateral dimensions ranging from 20 to 140 nm. Figure 5.7b displays an atomically resolved, filled-states STM image of the ceria island circled in figure 5.7a. A hexagonal lattice with an interatomic spacing of ~0.6 nm after calibration is observed, which is consistent with the ideal parameters for $\sqrt{3} \times \sqrt{3}$ CeO_2(111) [44]. The dark features on the ceria surface, which occupy the positions of the oxygen atoms, are assigned to surface oxygen vacancies O_{vac} [45]. The O_{vac} occur in various formations, such as individual, trimer and line defects. These defects have been

reported in previous studies conducted on both ceria ultrathin films [41,46] and the single crystal surface [43,47-50].

The appearance of the O_{vac} in our images differs slightly to that observed in high-temperature STM [43,49] and room-temperature NC-AFM [51] studies of the single crystal CeO_2(111) surface. In these studies, the surface O_{vac} also appear as dark features, which occupy an oxygen site in the filled-states images except with a slight outwards relaxation of the surrounding six oxygen atoms. No such outwards relaxation is observed on the ceria islands studied in this work. This phenomenon may be due to an electronic effect inherent to the ceria ultrathin film as compared to the bulk crystal or an experimental tip-related effect. The stability of the STM tip is crucial to obtaining high-quality atomically resolved images, and it was only after prolonged scans over an extended period of time that such imaging was possible.

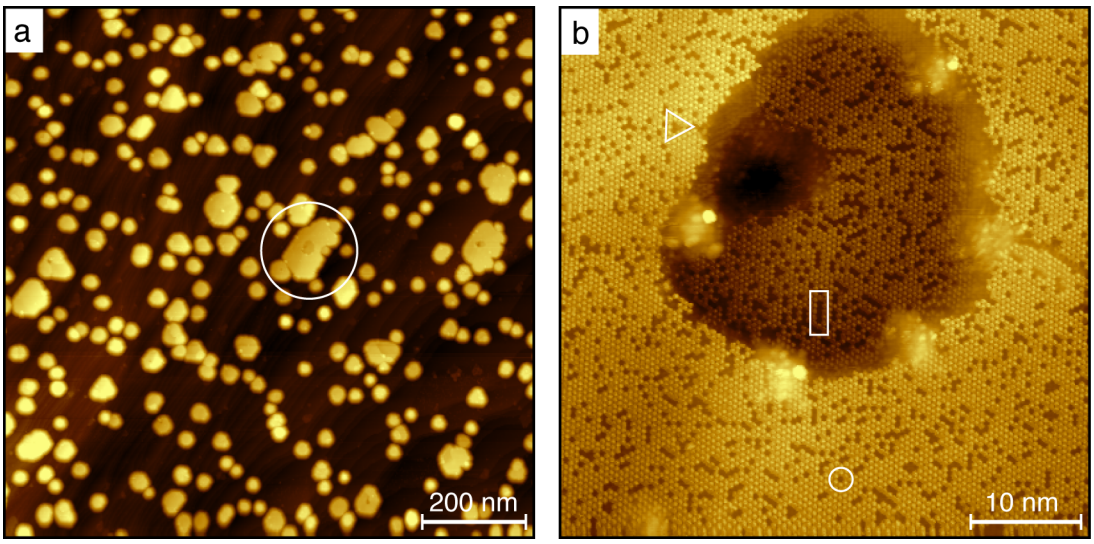

Figure 5.7 – STM images of $\sqrt{3} \times \sqrt{3}$ CeO_2(111) island grown on a Pt(111) substrate. a) Large-scale STM image (1000 × 1000 nm^2, -3.2 V, 0.05 nA) of a ceria ultrathin film with the Pt(111) substrate visible in between the CeO_2(111) island. b) Atomically resolved filled state STM image (47 × 47 nm^2, V_s = -3.2 V, I_t = 0.05 nA) of the circled island of image a), where oxygen atoms appear bright and oxygen vacancies dark. Examples of individual, trimer and line surface vacancies are highlighted in white.

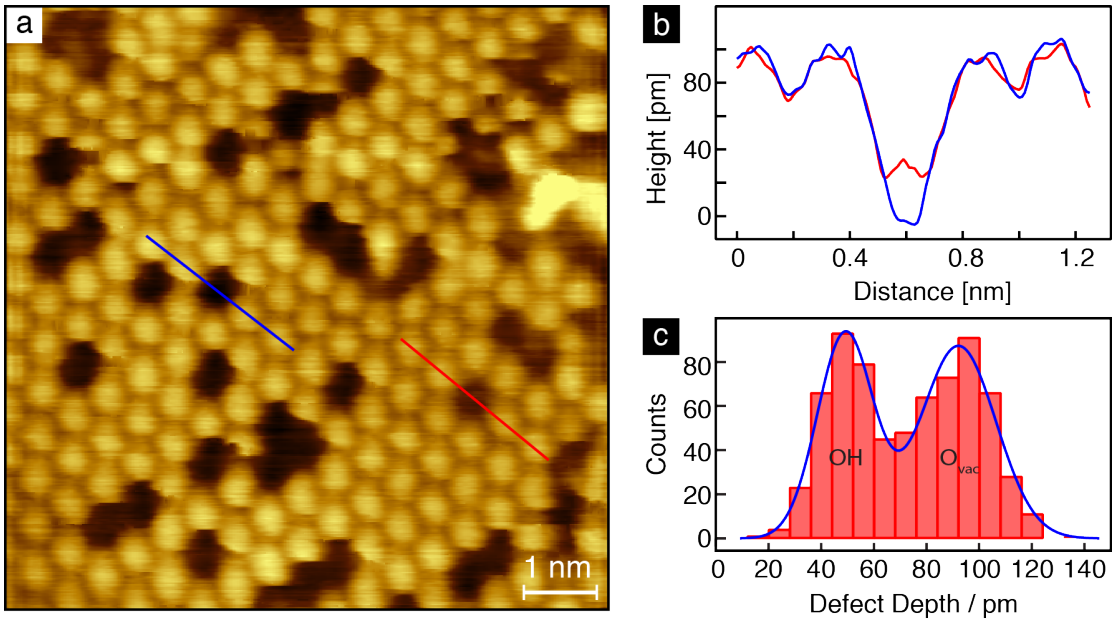

Figure 5.8 – a) Atomically resolved STM image (8 × 8 nm^2, V_s = -3.2 V, I_t = 0.02 nA) acquired atop a CeO_2(111) island grown on a Pt(111) substrate that exhibits surface O_{vac} of various depths. b) Line profile of the two surface O_{vac} highlighted in a). c) Histogram of the depths of the defects measured across numerous ceria islands.

Figure 5.8a exhibits an atomic resolution STM filled-states image of the surface of a $\sqrt{3} \times \sqrt{3}$ CeO_2(111) island on Pt(111). The surface of this island displays an abundance of defects, which are assigned to surface O_{vac}. Visually it is clear that not all the defects exhibit the same contrast, indicating that the depths of these defects are not uniform, as confirmed by the line profiles of figure 5.8b. After the extensive analysis of other STM images of ceria films, it was observed that these defects could be grouped into two types with depths of ~60 pm and ~100 pm. The histogram of Figure 5.8c shows the frequency of defect depths, measured for a total 692 defects from 9 different islands on 4 ceria films. The resultant bimodal distribution of the defect depths was fitted to two Gaussian peaks, which yielded mean depths for the two types of defects of 49 (±4) pm and 92 (±4) pm. The reduced ceria surface is predicted to facilitate the dissociation of water molecules at O_{vac} sites, resulting in the formation of OH species [52]. It is well known that the water is present in the background vacuum of the majority of UHV systems, thus it is plausible to assign the two types of defects to OH species and O_{vac} [29,53]. A similar occurrence

is observed on the rutile TiO_2(110) surface, where OH and O_{vac} are both imaged as bright protrusions at the surface, and are only distinguishable by their height difference [54].

5.4 STM Imaging Modes

In addition to the conventional contrast observed in the atomically resolved filled states images of figure 5.7 and figure 5.8, occasionally an alternative so-called honeycomb imaging mode is observed. Figure 5.9 displays successive scans of an identical section of a CeO_2(111) island obtained in both the conventional (figure 5.9a) and honeycomb (figure 5.9b) mode, which occurs spontaneously due to a change in the STM tip properties. A recent study also observed this honeycomb mode in empty state imaging, and proposed a model for the $\sqrt{3} \times \sqrt{3}$ CeO_2(111) structure, shown in figure 5.9c [55]. The overlay of the position of the cerium and oxygen atoms of this model onto the STM images presented in Figure 5.9 suggests that the depressions observed in the ceria lattice highlighted by black circles, which form a three lobed propeller shaped figure in the honeycomb mode displayed in figure 5.9b, are due to a simultaneous first layer O vacancy and a second layer Ce vacancy. The depression highlighted by a yellow circle also appears as a dark propeller-type shape in the honeycomb mode in figure 5.9b, located in between two successive oxygen rows in the normal imaging mode presented in Figure 5.9a, and is ascribed to a second layer Ce vacancy. Here, the white dots represent the O atoms in the first layer, the green dots represent the Ce atoms in the second layer white, and the light gray and dark gray dots represent the O atoms in the third and fourth layers, respectively. This honeycomb contrast mode has been reported previously in the literature for both single crystal CeO_2(111) and CeO_2(111) thin films [56,57], however the origin of this contrast mode is not fully understood at present. Nevertheless, by comparison to images of the ceria surface obtained using empty state imaging [55], it seems that in this honeycomb mode, the STM tip undergoes a spontaneous change to its properties that instigates the imaging of the second layer Ce atoms, and not the surface O atoms as is intended in the filled-state imaging mode.

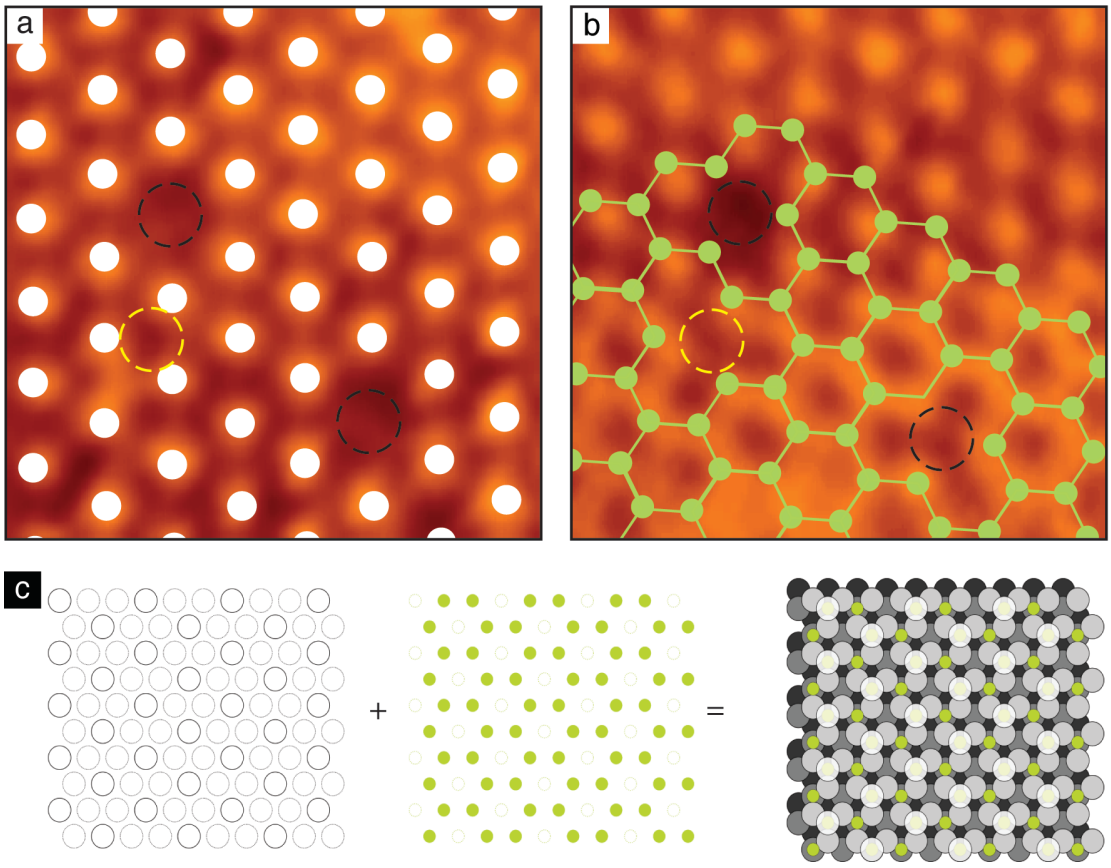

Figure 5.9 - Atomic resolution filled-states STM images (2.4 × 2.2 nm^2, V_s = -3.2 V, I_t = 0.05 nA) of defects at the surface of a ceria film obtained in a) the conventional imaging mode, and b) the honeycomb mode. c) Models of the $(\sqrt{3} \times \sqrt{3})$ $CeO_2(111)$, with the first layer oxygen atoms in white, the second layer cerium atoms green, and the third and forth layer oxygen atoms in light and dark gray, respectively.

5.5 Gold on $CeO_2(111)$ Ultrathin Films on Pt(111) and Rh(111) Substrates

Figure 5.10 displays an identical region of a $CeO_2(111)$ island before and after dosing approximately 0.01 ML of gold onto the surface *in situ*, at room temperature. The coverage of gold is defined in terms of that of the Au (111) surface, by which one monolayer (ML) corresponds to 1.4×10^{-15} atoms cm^{-2} [11]. After Au was dosed, the positions of the gold atoms were extrapolated to the image of the pristine surface and appear highlighted in figure 5.10 by white circles. These Au atoms appear as bright features in figure 5.10b, and are approximately 0.2 nm tall, indicative of regularly bound Au whereas atoms occupying a O_{vac} barely protrude from the $CeO_2(111)$ surface [9]. A comparison of their positions in figure 5.10b with figure 5.10a shows that there is no apparent preference for nucleation at surface O_{vac}, which appear as

depressions on this surface. This is somewhat surprising as DFT calculations suggest O_{vac} as thermodynamically favoured sites for Au adsorption [58]. However a more recent STM and DFT study addresses this apparent discrepancy by proposing that the large diffusion barriers (~1.0 eV) around the O_{vac} sites prevent the Au atoms from reaching them at room temperature [9]. It is noted that there are already a number of bright features on top of the surface, which we assign to water molecules from the background vacuum. Due to the low coverage of gold involved in this study, no visible change of the CeO_2(111)/Pt(111) LEED pattern was discernable, and in AES measurements the Au LMM and KLL peaks are superimposed on those pertaining to the Pt(111) substrate.

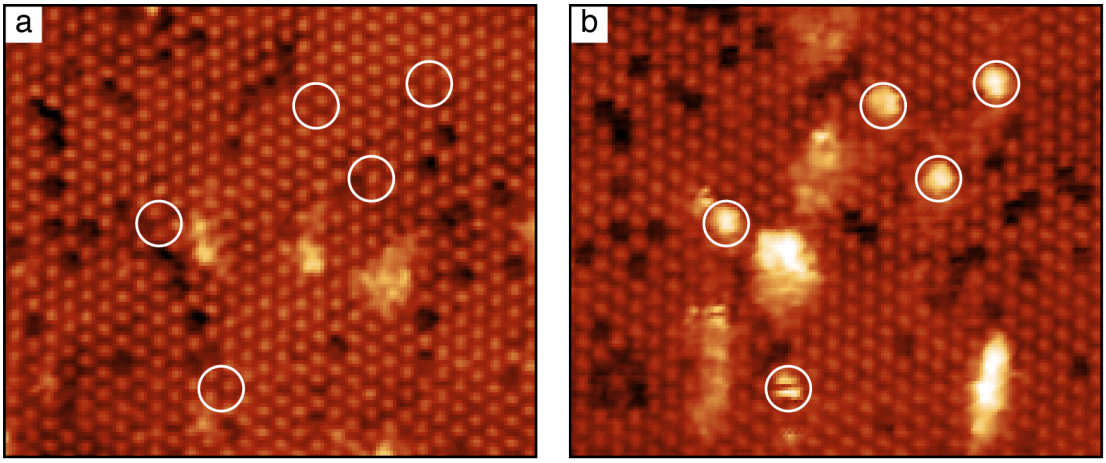

Figure 5.10 – Atomically resolved STM image of an identical surface region of CeO_2(111) acquired a) before (10.5 × 8.0 nm^2, V_s = -3.2 V, I_t = 0.10 nA), and b) after dosing Au (10.5 × 8.0 nm^2, V_s = -3.2 V, I_t = 0.10 nA). The Au atoms and their binding sites on the pristine surface are highlighted by circles. The Au surface coverage is estimated to be 0.01 ML. The oxygen vacancies are imaged as dark depressions on the ceria surface and their density is approximately 0.3 nm^{-2}.

Scanning on this type of surface is challenging as the Au atoms interact heavily with the tip, consequently tip convolution artefacts were extremely common, resulting in the distortion of the appearance of the gold atoms. In an attempt to improve the quality of imaging, steps were taken to minimise the interactions between the gold adatoms and the tip, i.e. testing various tunnelling currents in order to distance the tip from the surface and lowering the scanning speed and performing voltage pulses with the tip.

5.6 Summary and Conclusions

Scanning tunnelling microscopy has been employed to study the growth and defect structure of $\sqrt{3}\times\sqrt{3}$ $CeO_2(111)$ ultrathin films on Pt(111) and Rh(111), two important model catalytic system. The ceria films were prepared by a post-oxidation method in molecular oxygen, and characterised with STM, LEED and AES. This procedure resulted in the formation of isolated ceria islands, as opposed to a continuous film, on both the Pt(111) and Rh(111) substrates. The surface of these islands was composed of atomically flat terraces, which is crucial for obtaining sharp, atomically resolved STM images. STM images of ceria surface displayed numerous types of arrangements of surface vacancies, and an overall $\sqrt{3} \times \sqrt{3}$ reconstruction. Closer inspection of these vacancies in both the normal and honeycomb imaging modes indicated the presence of two types of defects, owing to either the simultaneous removal of a second layer Ce atoms and a first layer O atom, or solely due to a second layer Ce atom. A low coverage of gold (0.01 ML) was deposited *in situ* onto the films at room temperature and the results indicated that the gold atoms displayed no preference regarding adsorption sites, which contradicts an earlier DFT study where surface oxygen vacancies (O_{vac}) were proposed as the thermodynamically preferred adsorption site [58]. A recent combined DFT and STM study investigated the kinetic effects that govern Au adsorption on $CeO_2(111)$ by calculating the energy barriers that occur during Au adatom diffusion into surface Ov_{ac}; it found that the adsorption of gold atoms at surface O vacancies is highly improbable due to the large diffusion barrier (~1.0 eV) of O_{vac}, which inhibit the occupation of these defect sites by the gold atoms at room temperature, explaining why a thermodynamic picture may deviate from experimental findings, thus supporting the findings of the Au adsorption experiment detailed in this chapter [9].

References

[1] A. Trovarelli and P. Fornasiero, (2002).

[2] S. Bernal, J. J. Calvino, M. A. Cauqui, J. M. Gatica, C. Larese, J. A. Pérez Omil, and J. M. Pintado, Catalysis Today **50**, 175 (1999).

[3] D. R. Mullins, S. H. Overbury, and D. R. Huntley, Surf Sci (1998).

[4] M. Kovacevic, B. L. Mojet, J. G. van Ommen, and L. Lefferts, Catal Lett **146**, 770 (2016).

[5] Q. Fu, Science **301**, 935 (2003).

[6] Z.-P. Liu, S. Jenkins, and D. King, Phys. Rev. Lett. **94**, (2005).

[7] C. Zhang, A. Michaelides, D. A. King, and S. J. Jenkins, J Phys Chem C **113**, 6411 (2009).

[8] J. A. Rodriguez, X. Wang, P. Liu, W. Wen, J. C. Hanson, J. Hrbek, M. Perez, and J. Evans, Top Catal **44**, 73 (2007).

[9] P. G. Lustemberg, Y. Pan, B. J. Shaw, D. Grinter, C. Pang, G. Thornton, R. Perez, M. V. Ganduglia-Pirovano, and N. Nilius, Phys. Rev. Lett. **116**, 236101 (2016).

[10] M. M. Branda, N. C. Hernández, J. F. Sanz, and F. Illas, J Phys Chem C **114**, 1934 (2010).

[11] M. Baron, O. Bondarchuk, D. Stacchiola, S. Shaikhutdinov, and H. J. Freund, J Phys Chem C **113**, 6042 (2009).

[12] J. Guzman, S. Carrettin, J. C. Fierro-Gonzalez, Y. Hao, B. C. Gates, and A. Corma, Angew. Chem. Int. Ed. Engl. **44**, 4778 (2005).

[13] M. C. Kung, R. J. Davis, and H. H. Kung, J Phys Chem C **111**, 11767 (2007).

[14] P. Liu and J. A. Rodriguez, J. Chem. Phys. **126**, 164705 (2007).

[15] M. Škoda, M. Cabala, I. Matolínová, K. C. Prince, T. Skala, F. Šutara, K. Veltruská, and V. Matolín, J. Chem. Phys. **130**, 034703 (2009).

[16] D. C. Grinter, C. Muryn, B. Santos, B.-J. Shaw, T. O. Menteş, A. Locatelli, and G. Thornton, J Phys Chem C **118**, 19194 (2014).

[17] M. Chen and D. W. Goodman, Acc. Chem. Res. **39**, 739 (2006).

[18] M. Chen, Y. Cai, Z. Yan, and D. W. Goodman, J. Am. Chem. Soc. **128**, 6341 (2006).

[19] D. C. Grinter, C. L. Pang, C. A. Muryn, F. Maccherozzi, S. S. Dhesi, and G. Thornton, Journal of Electron Spectroscopy and Related Phenomena (2014).

[20] S. Eck, C. Castellarin-Cudia, S. Surnev, M. G. Ramsey, and F. P. Netzer, Surf Sci **520**, 173 (2002).

[21] E. L. Wilson, Q. Chen, W. A. Brown, and G. Thornton, J Phys Chem C **111**, 14215 (2007).

[22] V. Matolín, J. Libra, I. Matolínová, V. Nehasil, L. Sedláček, and F. Šutara, Applied

Surface Science **254**, 153 (2007).

[23] T. Staudt, Y. Lykhach, L. Hammer, M. A. Schneider, V. Matolín, and J. Libuda, Surf Sci **603**, 3382 (2009).

[24] W. Xiao, Q. Guo, and E. G. Wang, Chemical Physics Letters (2003).

[25] D. C. Grinter, C. M. Yim, C. L. Pang, B. Santos, T. O. Mentes¸, A. Locatelli, and G. Thornton, J Phys Chem C (2013).

[26] U. Berner and K. Schierbaum, Thin Solid Films **400**, 46 (2001).

[27] U. Berner and K.-D. Schierbaum, Phys. Rev. B **65**, 235404 (2002).

[28] E. L. Wilson, R. Grau-Crespo, C. L. Pang, G. Cabailh, Q. Chen, J. A. Purton, C. R. A. Catlow, W. A. Brown, N. H. de Leeuw, and G. Thornton, J Phys Chem C **112**, 10918 (2008).

[29] D. C. Grinter, R. Ithnin, C. L. Pang, and G. Thornton, J Phys Chem C **114**, 17036 (2010).

[30] J. L. Lu, H. J. Gao, S. Shaikhutdinov, and H. J. Freund, Surf Sci **600**, 5004 (2006).

[31] M. Juel, B. T. Samuelsen, M. Kildemo, and S. Raaen, Surf Sci (2007).

[32] H. Wolfschmidt, C. Baier, S. Gsell, M. Fischer, M. Schreck, and U. Stimming, Materials **3**, 4196 (2010).

[33] P. Grütter and U. Dürig, Phys. Rev., B Condens. Matter **49**, 2021 (1994).

[34] D. C. Grinter, C. Muryn, A. Sala, C.-M. Yim, C. L. Pang, T. O. Menteş, A. Locatelli, and G. Thornton, J Phys Chem C **120**, 11037 (2016).

[35] C. J. Baddeley, A. W. Stephenson, C. Hardacre, M. Tikhov, and R. M. Lambert, Phys. Rev. B **56**, 12589 (1997).

[36] J. M. Essen, C. Becker, and K. Wandelt, E-Journal of Surface Science and … (2009).

[37] K.-D. Schierbaum, Surf Sci **399**, 29 (1998).

[38] E. Bauer, **110**, 372 (1958).

[39] D. Briggs and M. P. Seah, *Practical Surface Analysis*, Second (John Willey & Sons, 1990).

[40] E. Napetschnig, M. Schmid, and P. Varga, Surf Sci **556**, 1 (2004).

[41] J. L. Lu, H. J. Gao, S. Shaikhutdinov, and H. J. Freund, Surf Sci **600**, 5004 (2006).

[42] P. Luches, F. Pagliuca, and S. Valeri, J Phys Chem C **115**, 10718 (2011).

[43] F. Esch, Science **309**, 752 (2005).

[44] U. Berner and K.-D. Schierbaum, Phys. Rev. B **65**, 235404 (2002).

[45] C. L. Pang, D. C. Grinter, J. Matharu, and G. Thornton, J Phys Chem C **117**, 25622 (2013).

[46] C. Castellarin-Cudia, S. Surnev, G. Schneider, R. Podlucky, M. G. Ramsey, and F. P. Netzer, Surf Sci **554**, L120 (2004).

[47] H. Nörenberg and G. Briggs, Surf Sci (1999).

[48] Y. Namai, K.-I. Fukui, and Y. Iwasawa, Catalysis Today **85**, 79 (2003).

[49] H. Nörenberg and G. A. D. Briggs, Phys. Rev. Lett. **79**, 4222 (1997).

[50] S. Gritschneder and M. Reichling, Nanotechnology **18**, 044024 (2007).

[51] S. Torbrügge, M. Reichling, A. Ishiyama, S. Morita, and Ó. Custance, Phys. Rev. Lett. **99**, (2007).

[52] M. B. Watkins, A. S. Foster, and A. L. Shluger, J Phys Chem C **111**, 15337 (2007).

[53] J. Kullgren, M. J. Wolf, C. W. M. Castleton, P. Mitev, W. J. Briels, and K. Hermansson, Phys. Rev. Lett. **112**, 156102 (2014).

[54] G. Teobaldi, W. A. Hofer, O. Bikondoa, C. L. Pang, G. Cabailh, and G. Thornton, Chemical Physics Letters **437**, 73 (2007).

[55] H. J. Yang, *in preparation*.

[56] S. Gritschneder and M. Reichling, J Phys Chem C **112**, 2045 (2008).

[57] J.-F. Jerratsch, X. Shao, N. Nilius, H.-J. Freund, C. Popa, M. Ganduglia-Pirovano, A. Burow, and J. Sauer, Phys. Rev. Lett. **106**, (2011).

[58] M. M. Branda, N. J. Castellani, R. Grau-Crespo, N. H. de Leeuw, N. C. Hernández, J. F. Sanz, K. M. Neyman, and F. Illas, J. Chem. Phys. **131**, 094702 (2009).

CHAPTER 6

IRON ON RUTILE TiO_2(110): A MAGNETIC, CHEMICAL AND TOPOGRAPHIC STUDY

Abstract

The growth and structure of iron nanowires supported on rutile TiO_2(110) has been investigated with low energy electron microscopy (LEEM), X-ray photoemission electron microscopy (XPEEM), scanning tunnelling microscopy (STM) and atomic force microscopy (AFM). The nanowires were grown by the deposition of iron onto the substrate, which was held at elevated temperatures. The magnetic domain structure was studied using X-ray magnetic circular dichroism (XMCD) and spin-polarised low energy electron microscopy (SPLEEM). The chemical analysis of the nanowires was performed via micro X-ray photoelectron spectroscopy (μ-XPS) and X-ray absorption spectroscopy (XAS). Our conclusions indicate that the orientation of the nanowires is dictated by the anisotropy of the substrate, i.e. the nanowires

grow along the [001] direction of the substrate. Moreover, at higher coverages of iron, the nanowires appear to be encapsulated by the titanium dioxide substrate, whereas at lower coverages, a (3 × 3) oxygen overlayer is observed. The various magnetic studies indicate that only the largest nanowires (10 nm × 1 nm × 20 nm) display any magnetic contrast.

6.1 Introduction

The discovery of the remarkable photocatalytic capabilities of titania (TiO_2) with regards to water splitting in the early 1970s prompted tremendous interest and research into this metal oxide [1]. Since then tremendous progress has been made in this field and the applications of TiO_2 have expanded into a variety of technological fields including gas sensing, heterogeneous catalysis, corrosion protection and electrical devices [2-8]. At present, rutile TiO_2(110) is the most studied single crystal titania surface and is thus considered the prototypical metal oxide surface for fundamental studies [9].

Metal nanoparticles on a metal oxide support have been studied extensively due to wide-ranging applications in a number of technologies [10-12]. In particular, directed self-assembling nanostructures show remarkable promise in the field of nanoscale electronics[13,14]. The decision to focus our attention on the Fe/TiO_2(110) system stems from its potential application as a component in electronic devices as Fe is capable of forming directed self-assembling nanostructures [15,16]. In addition, TiO_2(110) (1×1) possesses an anisotropic surface and a wide band gap, which facilitates the directed growth of nanostructures and ensures that the conducting nanostructures are electrically isolated. There are many reports in the literature of studies of self-assembled group VIII metals nanostructures on metal oxide supports [17,18].

The growth procedure used throughout our investigations is far from trivial and involves the deposition of Fe via physical vapour deposition (PVD) with the substrate held at an elevated temperature (~ 1070 K). Such high temperature depositions can result in the encapsulation of the nanostructures by the metal oxide support, which leads to the degradation of the chemical reactivity and can drastically alter the structure of the metal nanostructures [19-23]. Upon adsorption, a charge transfer from the metal adsorbate to the oxide can occur, resulting in the oxidation of the adsorbed metal atoms and the reduction of the oxide cations at the interface. The properties of oxide surfaces are dependent on the stoichiometry and some novel features

may appear when reduction takes place. Therefore, an understanding of the modification of adsorbed species and the substrate due to the interaction between the metal and the metal oxide substrate is fundamental for the design of new devices and other composite materials [24].

In this chapter the magnetic, chemical and topographic properties of Fe nanowires grown on rutile TiO_2(110)(1×1) are investigated with low-energy electron microscopy (LEEM), spin-polarised low-energy electron microscopy (SPLEEM), scanning tunnelling microscopy (STM), atomic force microscopy (AFM), low-energy electron diffraction (LEED), Auger electron spectroscopy (AES) and the following synchrotron radiation spectroscopies: X-ray photoelectron spectroscopy (μ-XPS), X-ray photoemission electron microscopy (XPEEM), X-ray magnetic circular dichroism (XMCD) and X-ray absorption spectroscopy (XAS).

6.2 Experimental Procedure

6.2.1 Spectroscopic Photoemission and Low Energy Electron Microscope

The synchrotron radiation spectroscopy and microscopy measurements were conducted on Beamline I06 of the Diamond Light Source in the United Kingdom. The endstation is comprised of two interconnected UHV chambers, one dedicated to sample preparation, and the other to spectroscopic measurements. The preparation chamber has a base pressure in the 10^{-9} mbar region, and is equipped with standard sample characterisation methods such as Auger electron spectroscopy (AES) and low energy electron diffraction (LEED) for surface characterisation, a sputter gun for sample cleaning, and an evaporator and quartz crystal monitor for metal deposition. The analysis chamber has a base pressure in the 10^{-10} mbar region, and is equipped with an *Elmitec* spectroscopic photoemission and low energy electron microscope (SPELEEM) capable of magnetic, topographic and chemical contrast. This versatile instrument is able to perform an array of techniques, including XMCD, XAS, μ-XPS, LEEM and XPEEM. The sample holder in the analysis chamber can be cooled down to a

temperature of 150 K using liquid nitrogen, and heated up to a temperature of 1800 K. A full description of the optical set-up of the beamline and the endstation can be found in chapter 3 of this thesis.

The rutile TiO_2(110) sample was prepared through cycles of Argon ion sputtering (10 min, 1.0 kV, 2.5μA) and annealing in UHV (10 min, 1000 K) until a sharp (1x1) LEED pattern was observed and contamination was below the detection level in AES. The sample temperature was monitored using both a pyrometer (*Minolta*) and a K-type thermocouple attached to the sample holder. Fe metal was deposited onto the TiO_2(110) substrate via physical vapour deposition (PVD) using an *Omicron EFM-3* electron-beam evaporator, which was equipped with a flux monitor, allowing for real-time deposition rate monitoring. A determining factor for the formation of nanowires as opposed to a thin-film is the sample temperature, which was maintained at ~1070 K during the Fe deposition. The presence of Fe on the substrate was initially confirmed by the presence of the characteristic Fe peaks in AES. The topography of the nanowires was observed using LEEM and AFM, the chemical composition of these features was determined using XPEEM, XAS and μ-XPS, and their magnetic properties of the wires was studied with XMCD and SPLEEM.

The μ-XPS spectra were acquired using photon energies of 820 eV and 650 eV for Fe *2p* and Ti *2p*, respectively; O *1s* spectra were acquired using both the aforementioned photon energies. The energy calibration of the spectra was performed relative to the value of the binding energy of the C *1s* peak presented in the literature (284.8 eV). The XAS spectra were recorded in total electron yield (TEY) mode, which in conjunction with the availability of circularly polarised light, allowed for a magnetic study of the Fe nanowires through XMCD, obtained by the difference spectrum of scans recorded with opposite photon helicity. The intensity of the XMCD signal is proportional to the dot product between the magnetisation direction and the helicity of the light, therefore these must be aligned to each other to some degree so that there are more possible transitions for one direction of light helicity than for the other. As such, the

sample position was varied between -90° to 90° to determine the optimum angle, i.e. the position corresponding to the parallel alignment of the magnetisation direction of the sample and the light helicity, which corresponds to a maximum in the XMCD image contrast. In addition, the dichroic signal is proportional to the degree of circular polarization of the x-rays. The polarization of the x-rays used in this experiment are ~99% [25].

6.2.2 Spin-Polarised Low Energy Electron Microscopy

The magnetic imaging experiments were carried out using a high-brightness and highly spin-polarised *Elmitec* LEEM located at the Osaka Electro-Communication University, Japan [26]. The SPLEEM instrument is composed of separate analysis and preparation chambers; the base pressure in the analysis chamber was lower than 2×10^{-8} mbar. The rutile TiO_2(110) samples was prepared in the usual manner, involving several cycles of Argon ion sputtering (20 min, 1.0 kV, 10 μA) and annealing in UHV (10 min, 1000 K) until a sharp (1×1) LEED pattern was observed. Fe was deposited onto the TiO_2(110) (1×1) substrate via physical vapour deposition using an *Omicron EFM-3* electron-beam evaporator, equipped with a flux monitor. The temperature of the sample during deposition was maintained between 1000 K and 1100 K, as elevated temperatures during deposition are essential for the formation of Fe nanowires; post-annealing of the Fe/TiO_2(110) system did not result in the formation of nanowires. The amount of Fe dosed on the samples ranged from 2 to 16 monolayers (ML); the evaporator was calibrated by monitoring the formation of a complete layer of Fe on a W(110) sample in situ using LEEM, while registering the elapsed time and the flux of Fe atoms. The temperature during annealing and Fe deposition was measured with an optical pyrometer (*Minolta*). In order for the topographic and magnetic information to be correlated, LEEM and SPLEEM images were obtained in parallel. SPLEEM images were acquired with orthogonal spin-polarisation directions along the [110], [$1\bar{1}0$], and [001] crystallographic orientation of the substrate after each Fe deposition; all SPLEEM images were acquired with a field of view of 6 μm.

6.2.3 Scanning Tunnelling Microscopy and Atomic Force Microscopy

The STM experiments were carried out at University College London using an *Omicron* variable temperature STM with a base pressure better than 5×10^{-10} mbar, operated in constant current mode at room temperature using electrochemically etched tungsten or mechanically fabricated platinum-iridium tips that were conditioned with voltage pulses to obtain stable atomic-resolution imaging. The STM images were obtained by tunnelling into empty states using positive bias voltages in the range of 0.5 - 2.0 V.

The rutile TiO_2(110) crystal (*Pi-Kem*) was mounted on a standard sample plate using spot-welded tantalum strips and prepared via multiple cycles of Argon ion sputtering (10 min, 1 keV, 10 μA) and annealing in UHV (10 min, 1000 K) until a sharp (1×1) LEED pattern was obtained and contamination was below the detection level of AES. The temperature during sample preparation and metal deposition was measured with an optical pyrometer (*Minolta*).

The Fe metal was deposited via physical vapour deposition (PVD) using an electron-beam evaporator while the TiO_2(110) sample was held at an elevated temperature (~ 1070 K) to ensure the formation of Fe nanowires. Analysis of the STM images of the metal dosed surfaces resulted in an estimated Fe coverage ranging from 2 to 9 ML.

The AFM experiments were performed in University College London and at Diamond Light Source (United Kingdom) using an in-air *Nanosurf Easyscan2* and *Veeco CP-II* AFM, respectively. The sole objective of these experiments was to determine the dimensions and the coverage of Fe nanowires on the various rutile TiO_2(110) samples from the aforementioned SPLEEM and SPELEEM experiments.

6.3 Results and Discussion

6.3.1 Scanning Tunnelling Microscopy and Atomic Force Microscopy

Scanning tunnelling microscopy was used to determine the optimum growth conditions for the Fe nanowires prior to carrying out the SPELEEM and SPLEEM experiments. The deposition of Fe at elevated temperatures was observed to result in the formation of two types of nanostructures, namely nanometre-size pseudohexagonal island and wires in the [001] direction of the substrate, as displayed in figure 6.1a and figure 6.1b. This is similar to the behaviour found for Pd [17].

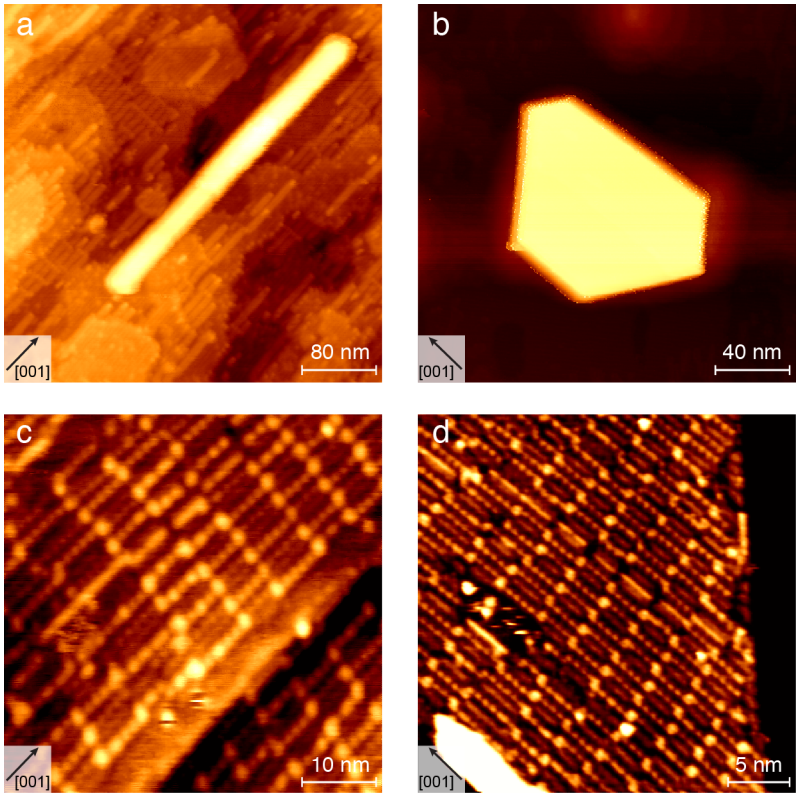

Figure 6.1 – Scanning tunnelling microscopy images of Fe nanostructures grown on rutile TiO_2(110) acquired at room temperature using a VT-STM. a) Fe nanowire structure ~40 × 4 nm and 1 nm tall (45 × 45 nm^2, V_s = +1.0V, I_t = 0.2nA), b) Fe pseudo-hexagonal structure ~8 nm tall (200 × 200 nm^2 V_s = +2.9 V, I_t = 0.07 nA), c) atomically resolved image of the surface of a) (25 × 25 nm^2 V_s = +2.7 V, I_t = 0.10 nA)), and d) atomically resolved image of the surface of b) (30 × 30 nm^2 V_s = +3.0 V, I_t = 0.14 nA).

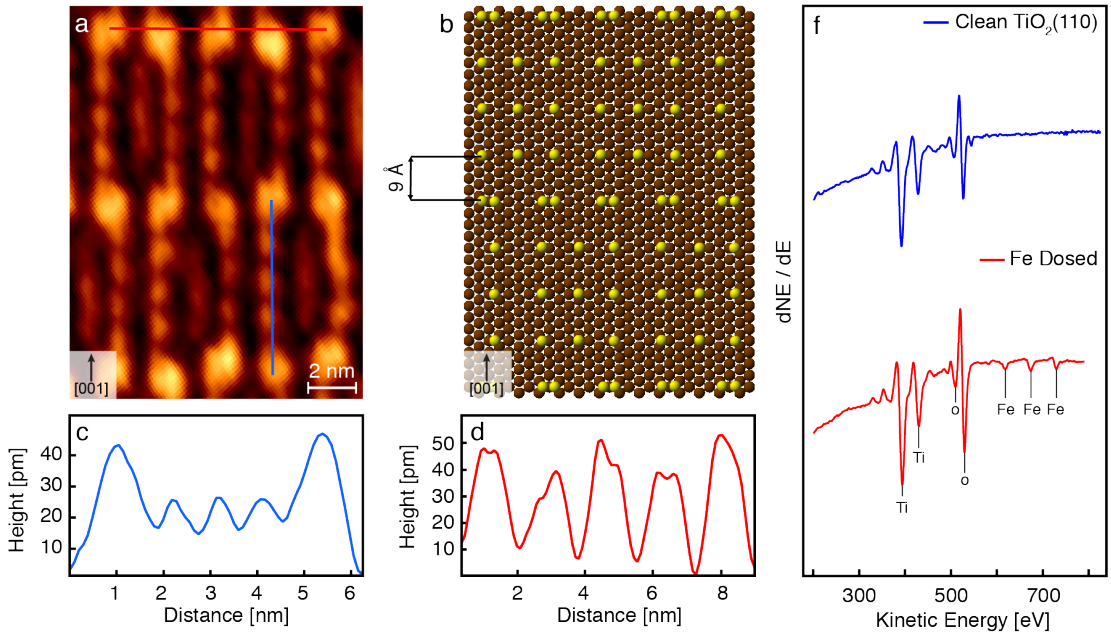

Figure 6.2 – Images of a) zoomed-in portion of the STM image of figure 6.1c with an across-row (red) and along-row (blue) line profile indicated, with the [001] azimuth of the TiO_2(110) substrate shown, b) illustrative ball-model of the Fe(110) surface (brown spheres) with a (16x5) - O overlayer (yellow spheres) [27-29], with the [001] Fe(110) azimuth shown, c) line profile along the rows, d) line profile across the rows, and e) Auger electron spectra of a clean TiO_2(110) surface (blue) and after dosing Fe (red).

The rutile TiO_2(110) surface has a two-fold symmetry and a 2.96 Å × 6.48 Å rectangular unit cell, with the short side along the surface bridging oxygen rows, in the [001] direction [30]. The lattice constant of iron is 2.87 Å, thus the lattice mismatch between the TiO_2(110) substrate and the Fe overlayer is about 3% in the [001] direction and 12% in the [1-10] direction [31]. Thus, the Fe(110)[001] direction presumably grows parallel to the [001] direction of the substrate due to the lattice matching. An atomically resolved image of the surface, presumably Fe(110), of the pseudohexagonal island of figure 6.1b is displayed in figure 6.1c. The surface is composed of parallel rows in the [001] direction, which are commensurate with [001] direction of the substrate, with three times the Fe lattice periodicity and a corrugation along the rows of ~0.9 Å. This surface has been identified as Fe(110)–(3×3)-O from resemblance with data from the adsorption of oxygen on Fe(110) [32,33]. Note that the surface structure of the nanowires was observed in STM to be identical to that of the pseudohexagonal islands. An expanded image of a section of the STM image of figure 6.1c is displayed in figure 6.2, along with the respective

line profiles and a tentative model of the Fe(110) surface with a (3×3) O overlayer, where the yellow spheres represent O atoms. As O was not introduced into the chamber during the course of the experiment, the presence of O on the surface of the nanostructures may be ascribed to the migration of oxygen species from the TiO_2(110) substrate, which is promoted by elevated temperatures, such as those used during the annealing step in the Fe nanostructure growth procedure [21,34,35].

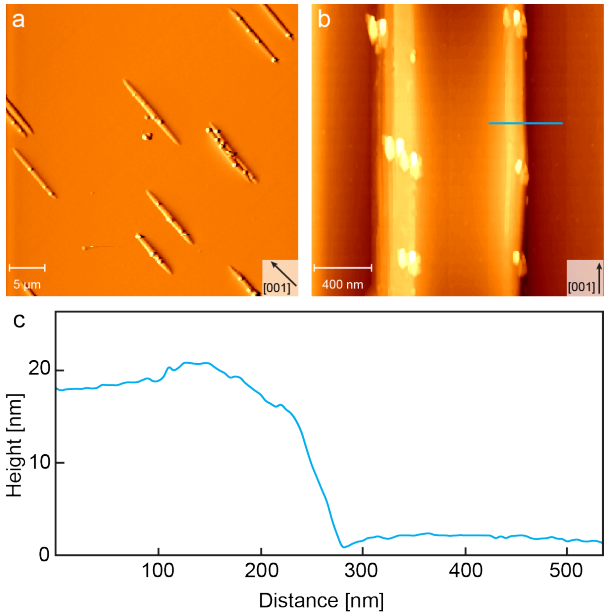

Figure 6.3 – Images of Fe nanowires grown on a rutile TiO_2(110) substrate acquired using a) atomic force microscopy (40 × 40 µm^2), and b) scanning tunnelling microscopy (2 × 2 µm^2, V_s = 2.0V, I_t = 0.1nA). Displayed below is a line profile of the height of the nanowire displayed in b). All images were acquired at room temperature.

The samples used in the SPELEEM experiments performed on beamline I06 of the Diamond Light Source (United Kingdom) were subsequently analysed using Atomic Force Microscopy (AFM) and Scanning Tunnelling Microscopy (STM) in order to determine the dimensions of the nanowires more accurately. Figure 6.3 displays a) a large scale AFM image of the nanowires (40 × 40 µm^2), b) a zoomed-in STM image of a nanowire (2 × 2 µm^2), and c) the respective line profile of the nanowire. According to these results the nanowires grown during the first experimental run at DLS were approximately 20 nm tall, 1 µm wide and up to 10 µm long. The nanowires produced on the second experimental run were measured to be around 14 nm in

height, 2 μm in width and up to 6 μm in length. The nanowires produced on both occasions were almost three orders of magnitude larger than those of the STM experiment performed at UCL. Although not visible, pseudohexagonal islands similar to those observed in STM may be present on the surface, however these will be beyond the resolution limit of the AFM.

6.3.2 Spectroscopic Photoemission and Low Energy Electron Microscope

The (110) surface of rutile TiO_2 has been the subject of many studies and has been well characterised by various spectroscopic and microscopic techniques. The un-reduced TiO_2(110) surface is terminated by a (1×1) configuration, consisting of alternate rows of bridging oxygen and five-fold coordinated titanium atoms, which run in the [001] direction. The sharp (1×1) LEED pattern of figure 6.4 was obtained after several Argon ion sputter (10 min, 1 kV, 2 μA) and UHV anneal cycles (~1000 K), and is indicative of a well-ordered TiO_2(110) (1×1) surface.

Fe atoms were deposited onto the clean TiO_2(110) surface at a sample temperature of ~1070 K and at a flux of 80 nA, for 10 minutes. Subsequently, the Auger electron spectrum displayed in figure 6.4 was acquired, which confirmed the presence of Fe on the surface via the appearance of the characteristic peaks at 598, 651 and 703 eV. The presence of a peak at 272 eV is an indication of adventitious carbon at the surface. Also displayed in figure 6.4 are the characteristic Ti and O KLL Auger peaks, which originate from the TiO_2(110) sample. The topography and chemical composition of the structures formed after Fe deposition in the first and second experimental runs was examined using LEEM and XPEEM, and a selection are displayed in figure 6.5 and 6.6, respectively. The deposition of Fe at elevated temperatures resulted in the formation of nanowires along the [001] direction due to the anisotropy of the TiO_2(110) (1×1) substrate; the dimensions of these features was observed to be very sensitive to the dosing settings and sample temperature. These self-assembling types of nanostructures have also been reported for other group VIII metals, such as Pd [17] and Rh [18]. Figure 6.5 displays both LEEM (a, b) and XPEEM (c, e, f) images of the nanowires grown during the first

experimental run. These nanowires were much larger than those grown for the STM experiment, measuring around 10 μm in length, and unexpectedly displayed small dot-like features, which will be discussed in more detail later. In addition to the nanowires, irregular shaped clusters were also observed on the surface, an example of such is displayed in figure 6.5 (f). This feature was identified through XAS as Ca, a common contaminant segregated from the bulk of rutile TiO_2(110) samples [36]. Upon this observation, a Ca L-edge XAS scan (E = 330-360 eV) was also performed on the nanowires and dots, however no evidence of Ca was found.

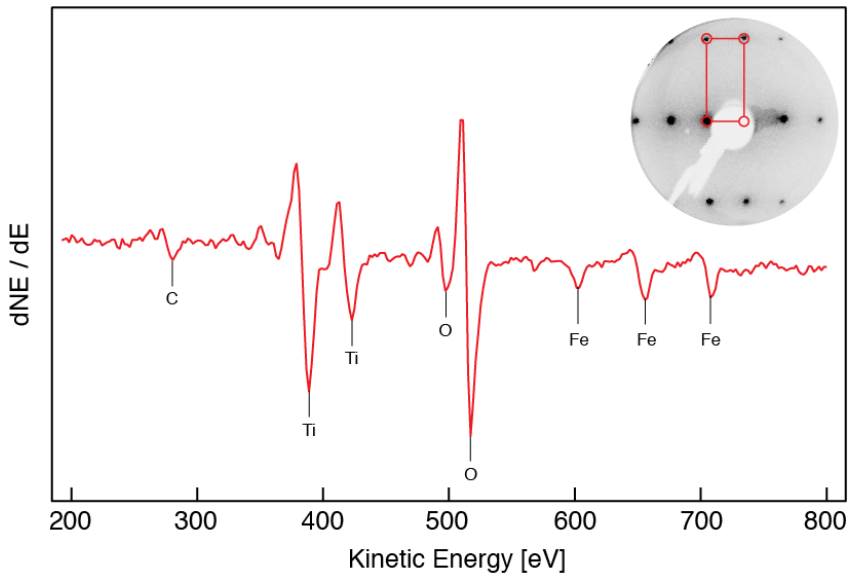

Figure 6.4 - Derivative Auger electron spectrum of a Fe dosed rutile TiO_2(110) sample used in the SPELEEM experiment confirming the presence of iron on the surface via the appearance of the characteristic Fe peaks at 598, 651 and 703 eV. Inset is a low energy electron diffraction pattern (E = 53.7 eV) of a clean rutile TiO_2(110) sample, acquired prior to the Fe deposition. The (1×1) periodicity of the sample is displayed by the red rectangle superimposed on the LEED image.

The nanowires formed during the second experimental run were slightly smaller in comparison and only some exhibited nanodots. A subsequent AFM study revealed that these nanowires were approximately 14 nm high, 2 μm wide, and 6 μm long, with a coverage of roughly 9 ML. An example of a nanowire containing a dot is displayed in figure 6.6 (d - f). Tuning of the incident photon energy to specific absorption edges, i.e. Fe L-edge (707.4 eV), Ti L-edge (462.2 eV) and Ca L-edge (350.8 eV), identified Ca in the composition of the nanodot.; XPS data also corroborated this finding.

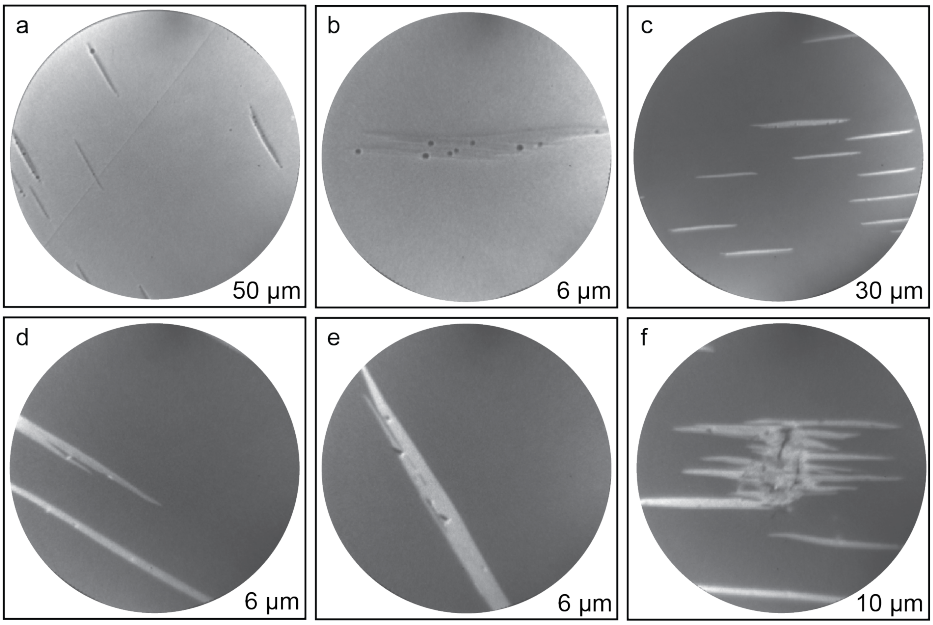

Figure 6.5 –Images of Fe nanowires grown on rutile TiO_2(110) acquired using the SPELEEM instrument during the first experimental run at Diamond Light Source. Images a) and b) were obtained using LEEM, while images c) to f) were taken using XPEEM with a photon energy of 706.5 eV.

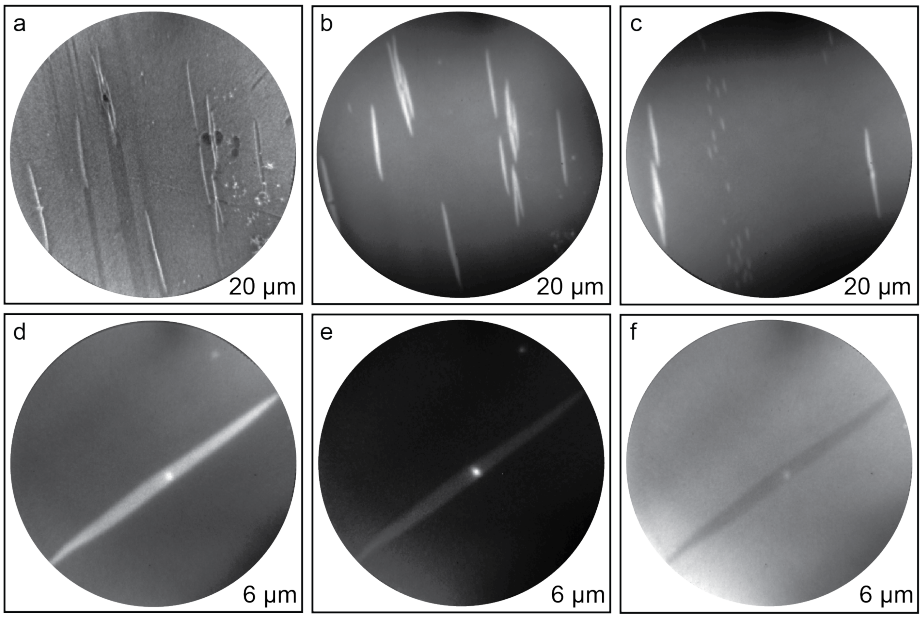

Figure 6.6 - Images of Fe nanowires grown on rutile TiO_2(110) acquired using the SPELEEM instrument during the second experimental run at Diamond Light Source. Image a) was obtained using LEEM in mirror mode, images b) to f) were taken using XPEEM with a photon energy of 707.4 eV (b-d), 350.8 eV (e), and 462.2 eV(f).

X-ray Photoelectron Spectroscopy (XPS)

In order to determine the exact chemical composition of the nanowires displayed in figure 6.7, μ-XPS data of the O *1s*, Ti *2p* and Fe $2p_{3/2}$ regions were recorded at Diamond Light Source (Didcot) and analysed using the *CasaXPS* software. The O *1s* and Fe $2p_{3/2}$ data were acquired using a photon energy of 820 eV, while an energy of 650 eV was used for the Ti *2p* data. The energy axis was calibrated using the value of 284.8 eV for the C *1s* peak reported in the literature [37]. The XPS spectrum displayed in each figure is the result of the addition of numerous spectra in order to achieve a better signal to noise ratio.

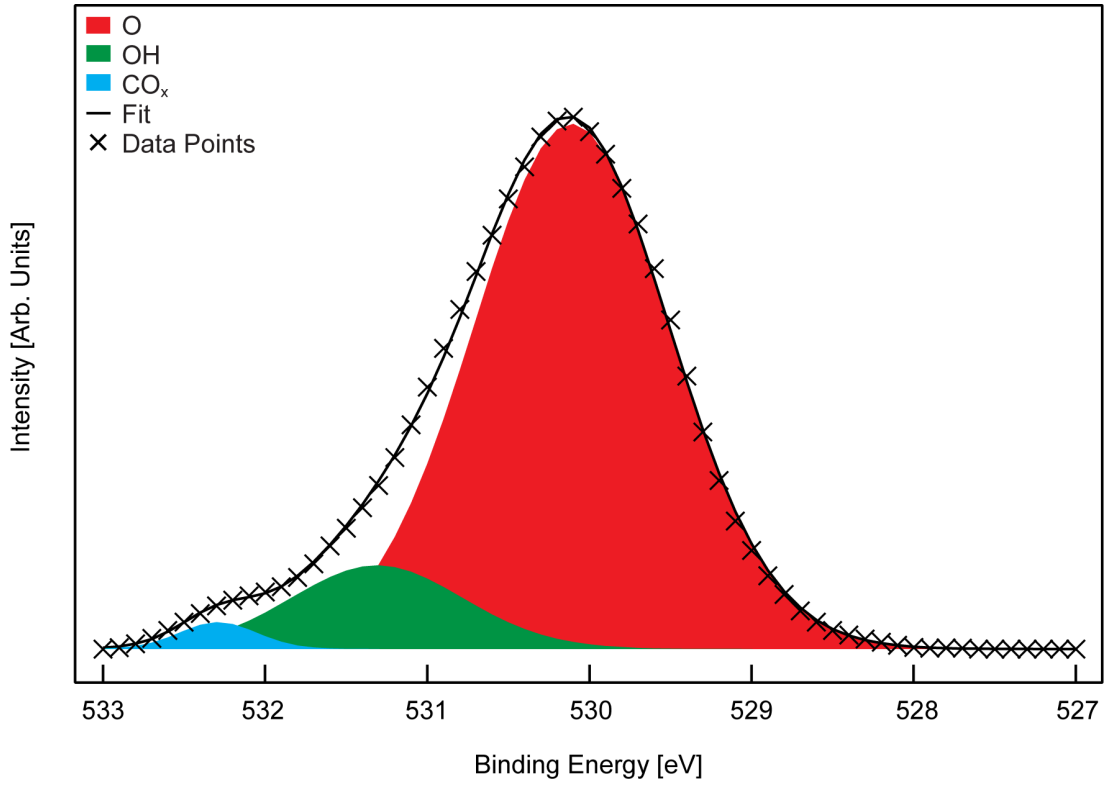

Figure 6.7 - X-ray photoelectron spectrum of the O *1s* region of the Fe nanowires grown on rutile TiO_2(110), acquired using a photon energy of 820 eV and a field of view of 6 μm. The deconvolution of the spectrum was performed using Gaussian-Lorentzian lineshapes (30:70), after a Shirley type background had been subtracted. The data were fit to three peaks pertaining to lattice O (red), surface OH (green), and CO_x contamination (blue).

The O *1s* region is displayed in figure 6.7, and displays contributions from O, OH and COx contamination at a binding energy of 530.1 eV, 531.4 eV and 532.3 eV, respectively [38]. The contributions were fitted using Gaussian-Lorentzian type lineshapes (30:70) after a Shirley type background was subtracted. The OH contribution can be assigned to the reaction of O vacancies with residual water and the COx to adventitious carbon at the sample surface.

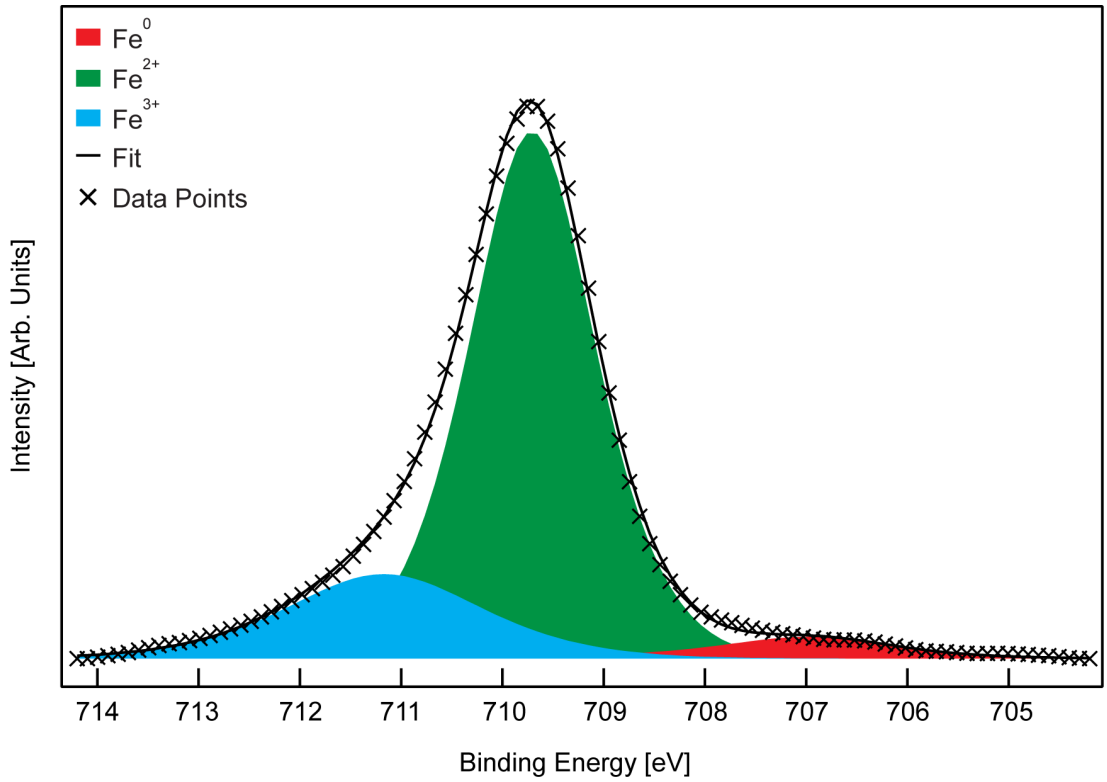

Figure 6.8 – X-ray photoelectron spectrum of the Fe $2p_{3/2}$ region of the iron nanowires grown on a rutile TiO_2(110) sample, acquired using a photon energy of 820 eV and a field of view of 6 μm. The deconvolution of the spectrum was performed using Gaussian-Lorentzian lineshapes (30:70), after a Shirley type background had been subtracted. The data were fit to three peaks pertaining to metallic Fe (red), and the oxidised iron species Fe^{2+} (green), and Fe^{3+} (blue).

The XPS spectrum of the Fe region of the nanowires is displayed in figure 6.8, and was fit to three peaks with Gaussian-Lorentzian type lineshapes (30:70), after a Shirley type background was subtracted [39]. Peaks pertaining to metallic iron and the oxidised Fe^{2+} and Fe^{3+} species were observed at 706.9 eV, 709,7 eV and 711.1 eV, respectively. Constraints regarding FWHM and peak positions were also applied during the fitting procedure [35,38,40,41].

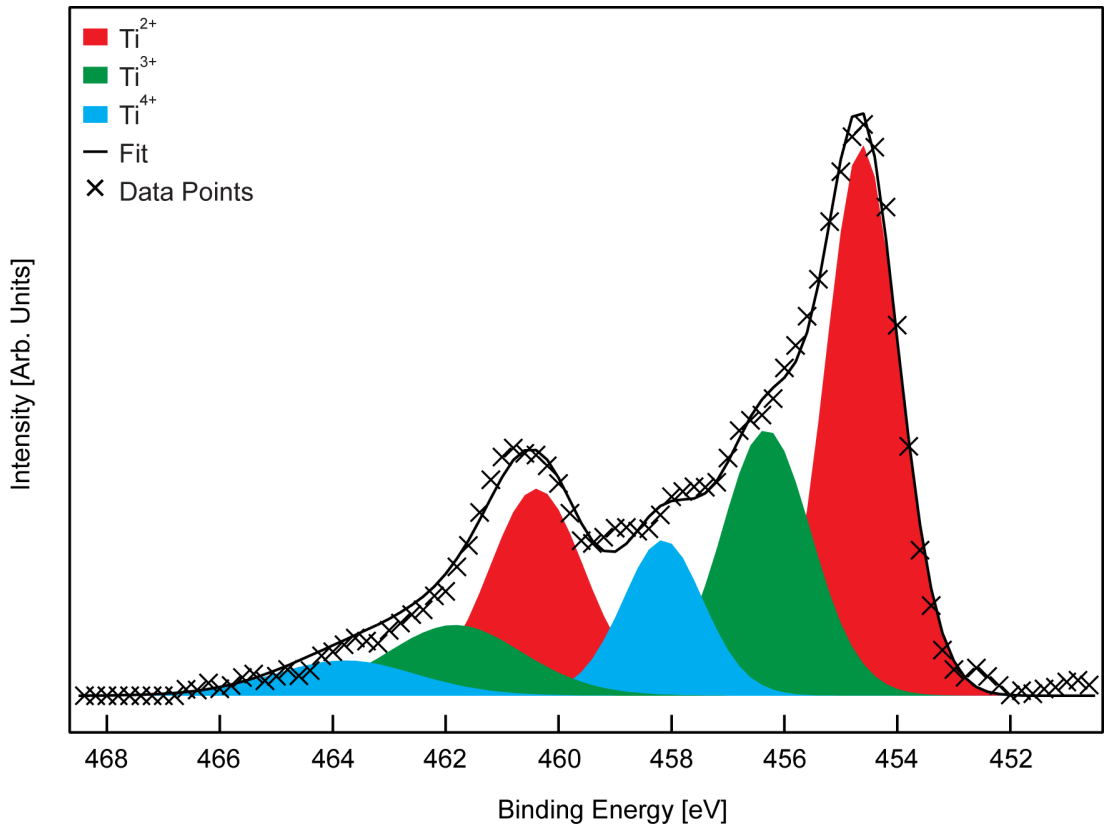

Figure 6.9 - X-ray photoelectron spectrum of the Ti *2p* region of the Fe nanowires grown on a rutile TiO_2(110) sample, acquired using a photon energy of 650 eV and a field of view of 6 μm. A Shirley type background was subtracted and the data were fit using two sets of three Ti 2*p* doublets with Gaussian-Lorentzian lineshapes (30:70), pertaining to Ti^{2+} (red), Ti^{3+} (green) and Ti^{4+} (blue).

The Ti photoemission spectrum reveals the presence of three types of titanium species, namely Ti^{2+}, Ti^{3+} and Ti^{4+}, as displayed in figure 6.9. A Shirley type background was subtracted from the data and each Ti *2p* doublet was fit to three contributions with Gaussian-Lorentzian lineshapes (30:70), corresponding to Ti^{2+}, Ti^{3+} and Ti^{4+} species. The fitting of this multiplet peak requires the imposition of certain restraints such as the peak area and position [35,42-44]; in accordance with the literature, the area of the peaks in the Ti $2p_{1/2}$ region was constrained to half that of the Ti $2p_{3/2}$ region, the multiplet separation of each oxidised Ti species was held constant at 5.7 eV, and the Ti^{2+} - Ti^{3+} and Ti^{3+} - Ti^{4+} energy separation for each multiplet peak was set to 1.7 eV and 1.8 eV, respectively [45].

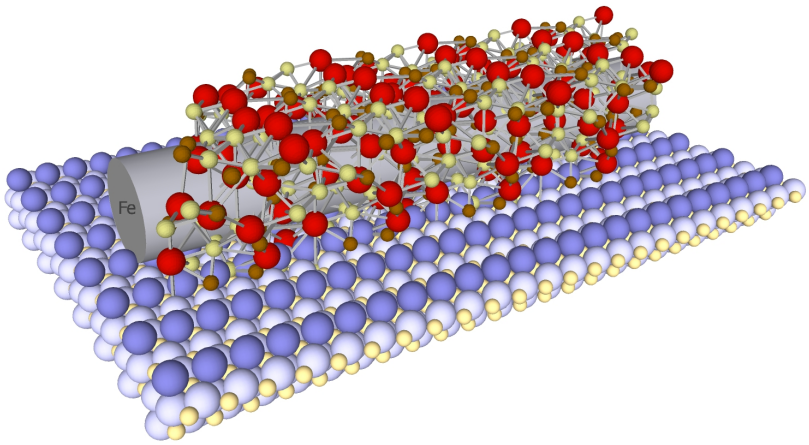

Figure 6.10 – Illustrative ball-model image of a metallic iron nanowire encapsulated by a $FeTiO_3$ overlayer on a rutile $TiO_2(110)$ surface.

The overall analysis of the chemical composition of the nanowires indicates the presence of oxygen, iron (Fe^0, Fe^{2+}, Fe^{3+}) and titanium (Ti^{2+}, Ti^{3+}, Ti^{4+}) species. Inelastic mean free path calculations (IMFP) were used to determine the degree of surface sensitivity of the XPS experiments, and it is estimated that the Ti ($h\nu$= 650 eV) and Fe ($h\nu$= 820 eV) ions originate from a depth up to about 5.0 nm and 4.2 nm, respectively [46]; considering that the average height of the nanowires was 14 nm, this represents a sampling depth of about ⅓ of the nanowire height. This suggests that, upon adsorption of Fe at elevated temperatures, oxygen and titanium species migrate from the $TiO_2(110)$ substrate and decorate the Fe nanowires. This phenomenon is known as encapsulation and has been reported in the literature for several group VIII metals [22,47-49]. Moreover, the reduction of the Ti^{4+} species to Ti^{3+} and Ti^{2+} is likely due to the effects of beam damage in micro-focus PEEM, which has been reported previously in the literature for several metal oxide systems, but not iron oxides [50]. Taking into account the fact that Fe is also still observed in its metallic state suggests that the core of the nanowires remains in a metallic state; the small amount measured in XPS may be due to the short sampling depth for Fe, i.e. 4.2 nm, approximately ⅓ of the total nanowire height. The simultaneous presence of both Fe^{2+} and Fe^{3+} suggests that the encapsulating layer is formed of mixed Fe-Ti oxides, possibly a combination of ilmenite ($FeTiO_3$) and hematite (α-Fe_2O_3) [35,51-56]. An illustrative

model of a nanowire encapsulation layer is displayed in figure 6.10. A similar observation has been made for the (011) surface of rutile TiO_2, which supports the formation of an ordered mixed $FeTiO_3$ layer [57]. The XPS results also indicate that there is a size dependence of the structure of the nanowires, with larger wires favouring encapsulation whilst smaller nanowires appear to contain an (16 × 5) oxygen overlayer, as indicated by STM.

X-ray Absorption Spectroscopy (XAS)

X-ray spectroscopy techniques, namely X-ray absorption spectroscopy (XAS) and x-ray photoelectron spectroscopy (XPS), were used in order to characterise the chemical nature and environment of the rutile TiO_2(110) substrate and the Fe nanowires. XAS probes ground state to excited state transitions. The XAS spectra were acquired in total electron yield mode (TEY) at the Ti $L_{2,3}$-edge of a clean TiO_2(110) and a Fe dosed sample, and are displayed in figures 6.11 and 6.12, respectively.

The spectrum of the clean TiO_2(110) single crystal displays four characteristic bands with alternating t_{2g} and e_g symmetries pertaining to the L_3 and L_2 edges as labelled in figure 6.11 [58-60]. The first pair of lower energy bands is separated from the second pair at higher photon energies by the spin-orbit interaction of the Ti *2p* core hole. The structure within these two sets of peaks is believed to arise from the crystal-field splitting of the *d*-derived final states into t_{2g}- and e_g- like levels [36,58]. Further splitting of the e_g band at ~ 459 eV into two features, ascribed to the $d_{x^2-y^2}$ and the d_{z^2} orbitals, has been justified by the reduction of local-site symmetry from octahedral to tetragonal [61,62]. An alternative explanation suggests that the splitting may originate from a dynamic Jahn-Teller effect, i.e. coupling of electronic and vibrational states [63]. However, the exact origin of the fingerprint L_3 e_g peak splitting remains unclear [64]. The two pre-edge features at ~ 456.3 eV and ~ 457.4 eV are related to intra-atomic multiplet

splitting effects [59,65]. The XAS results for the clean TiO_2(110) sample are in good agreement with those reported in the literature [58,62,64,66-69].

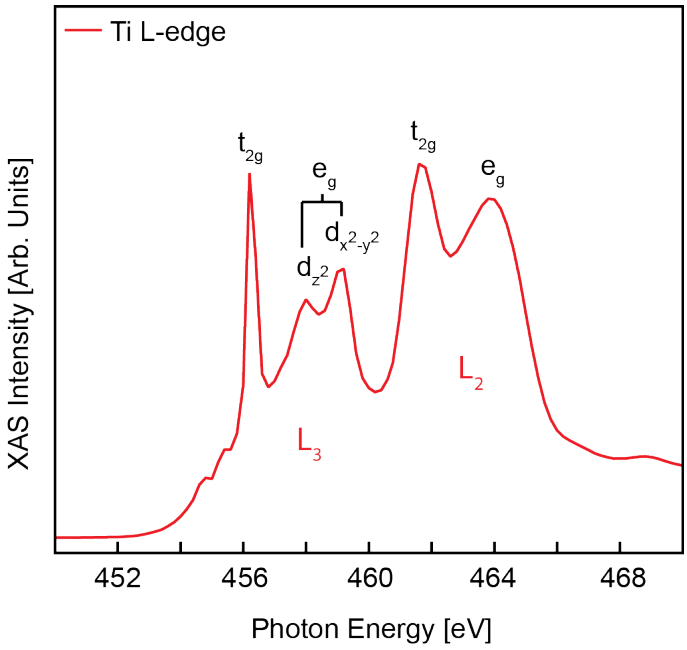

Figure 6.11. Total electron yield detection mode Ti $L_{2,3}$-edge XAS spectra of a clean rutile TiO_2(110) sample acquired with a field of view of 20 μm.

The XAS spectra displayed in figure 6.12 pertain to a Fe dosed sample and were acquired in TEY mode of the XPEEM. The substrate Ti $L_{2,3}$-edge spectrum (red) is identical to that of figure 6.11 and is readily assigned rutile TiO_2(110). The Ti $L_{2,3}$-edge spectrum of the Fe nanowires similarly display four distinct bands, however no splitting of the lower energy e_g band is observed. A careful analysis of the literature, in conjunction with the XPS results presented in this chapter, suggest that the Fe nanowires are in fact composed of an ilmenite-type ($FeTiO_3$) compound [51,62,70-72]. Similarly to that of rutile TiO_2(110), an ilmenite Ti $L_{2,3}$-edge spectra displays two pre-peaks, though there is no significant splitting of the lower energy e_g peak, as in figure 6.12 (blue).

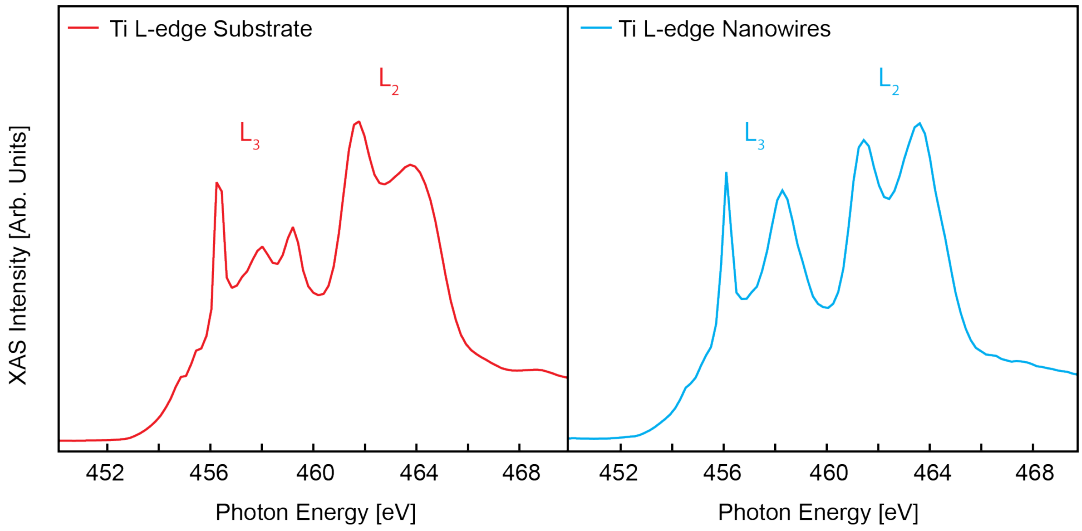

Figure 6.12 - Total electron yield detection mode Ti $L_{2,3}$-edge XAS spectra of the rutile TiO_2(110) substrate (red) and Fe nanowires (blue) from a sample from the first experimental run, acquired with a field of view of 20 μm.

X-ray Magnetic Circular Dichroism (XMCD)

The next step in the study of the Fe nanowires encompassed an investigation of the magnetic properties of the system using X-ray magnetic circular dichroism (XMCD). X-ray Magnetic Circular Dichroism (XMCD) is a surface sensitive technique (2-3 nm) that uses the differential absorption of left and right circularly polarised light to examine magnetic materials and properties. The study involved the recording of XMCD images and spectra while the sample was illuminated with either left or right circularly polarised light. A preliminary observation of an area of the sample was performed using XPEEM at a photon energy of 706.5 eV, corresponding to an energy near that of the Fe L_3 white line, as displayed in figure 6.13. After a suitable area of the sample was located, a pair of XPEEM images was acquired by tuning the photon energy to both the Fe L_2 and L_3-edge, i.e. the onset of excitation of transitions of the *2p* core electrons to empty states above the Fermi level, as is customary for *3d* transition metals [73].

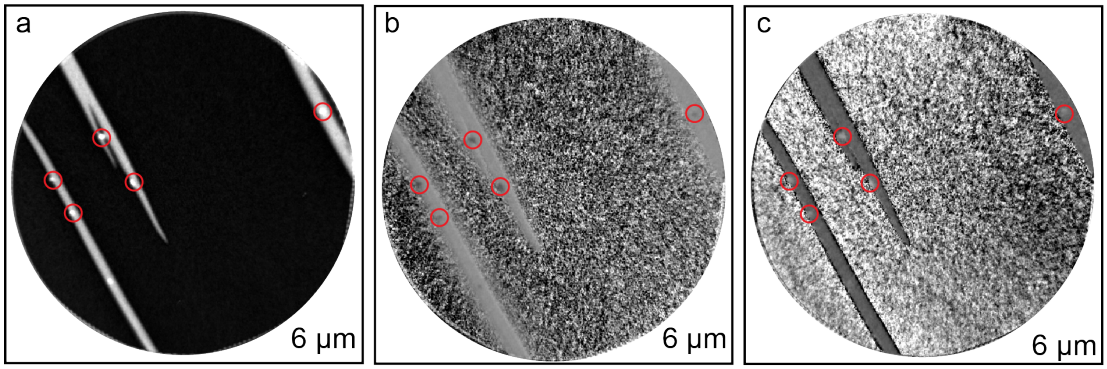

Figure 6.13 – Images of the Fe nanowires grown on a rutile TiO_2(110) substrate attained using a) XPEEM ($h\nu$ = 706.5 eV), b) XMCD-PEEM acquired in total electron yield detection mode at the Fe L_3-edge ($h\nu_{ON}$ = 706.5 eV, $h\nu_{OFF}$ = 703.0 eV), and c) at the Fe L_2-edge ($h\nu_{ON}$ = 719.5 eV, $h\nu_{OFF}$ = 703 eV). The field of view of all images is 6 µm, and $h\nu_{ON}$ / $h\nu_{OFF}$ denotes a photon energy on / off the core level energy. The broadening of the nanowires observed in the XMCD-PEEM images is drift related, as the images are the result of the addition of multiple images.

The XMCD image is obtained by subtraction of two XPEEM images obtained with light of opposite helicity, i.e. pixel-by-pixel intensity asymmetry ratio $(\mu_- - \mu_+) / (\mu_- + \mu_+)$, of two images sequentially recorded at the Fe $L_{2,3}$ edges with right (μ_+) and left (μ_-) circularly polarised light. In order to improve statistics, typically a series of twenty XMCD images are recorded, from which, upon drift correction, an average image is obtained. Domains magnetised parallel or antiparallel to the polarisation vector will appear black or white in the XMCD image, while domains with a magnetisation perpendicular to the polarisation vector will have a grey contrast [74,75]. Displayed in figure 6.13 are two XMCD images of the nanowires on a rutile TiO_2(110) substrate, acquired at the Fe L_2 and Fe L_3-edge. Intriguingly, the nanowires are observed to exhibit nanodots in certain regions, which are highlighted in red. An inversion of contrast of both the nanowires and the nanodots is observed, with the latter being more pronounced. This is a strong indication of the existence of ferromagnetic domains on these structures, which are further investigated in the XAS study that follows.

XAS is a highly sensitive *in situ* probe of orbital m_l and spin m_s magnetic moments, and in contrast to many other techniques, is capable of element and chemical state specificity. The

XAS signal related to transitions into empty *3d* states is manifested as two peaks at the energetic positions of the $2p_{1/2}$ (L_2) and $2p_{3/2}$ (L_3) states, whereas transitions into unoccupied *s*, *p* states give rise to a step-like background. The sum rules [76,77] are equations based on integrated XMCD spectra that allow the individual determination of the orbital and spin magnetic moments of the ground state, without resort to laborious simulation techniques [78,79]. The XMCD spectrum is the difference between two XAS spectra recorded with either left or right circularly polarised X-rays, denoted by μ_+ and μ_- respectively. According to the sum rules m_l and m_s can be determined from the XAS and XMCD spectra by using the following equations:

$$m_l = \frac{-4q(10 - n_{3d})}{3r} \tag{6.1}$$

$$m_s = \frac{-(6p - 4q)(10 - n_{3d})}{r} \tag{6.2}$$

where n_{3d} is the *3d* band electron occupation number of the specific transition metal atom, *p* and *q* are the integrals of the XMCD spectra over L_3 and over L_3 + L_2 respectively, and *r* is the integral of the sum of XAS spectra of opposite X-ray helicity ($\mu_+ + \mu_-$) after a two-step-like background is subtracted. This background removal process allows the elimination of the L_3 and L_2 edge jumps; the thresholds for the two-step-like function were set to the peak positions of the L_3 and L_2 white lines, with a relative step height of 2:1 in accordance with the occupation of the $2p_{3/2}$ and $2p_{1/2}$ core states [80-82]. The ratio of m_l to m_s is also often calculated as this can be performed without the prior knowledge of the n_{3d} value.

$$\frac{m_l}{m_s} = \frac{2q}{9p - 6q} \tag{6.3}$$

The sum rules allow the determination of m_l and m_s with an uncertainty of around 10 to 20%, whereas the m_l / m_s ratio is thought to be accurate within about 5% [79,80,83,84]. Here we report XMCD measurements of m_l and m_s in Fe nanodots and nanowires with sizes up to ~10 μm, supported on rutile TiO_2(110). The spectra acquired from the Fe nanodots and the

nanowires are displayed in figure 6.14 and figure 6.15, respectively. The top spectrum in both figures pertain to the individual XAS data collected using right μ_- (blue) and left μ_+ (red) circularly polarised light, in total electron yield (TEY) detection mode. The Fe $L_{2,3}$-edge spectra are nearly characteristic of the Fe^0 and Fe^{2+} states, however a small shoulder on the high binding energy side indicate the presence of Fe^{3+} species [51]. The middle section displays the XMCD spectrum (red) and respective integral (blue) of the aforementioned XAS spectrum, while the bottom spectrum shows the result of the integration of the $\mu_+ + \mu_-$ spectrum (red) after a two-step-like background was removed. The XAS and XPS results suggest that the nanowires are composed of a metallic iron core with an encapsulation layer consisting of mixed Fe-Ti oxides, possibly a mixture of $FeTiO_3$ and α-Fe_2O_3, which would explain the presence of the mixed valence state of Fe (Fe^0, Fe^{2+}, Fe^{3+}) and the existence of an XMCD signal; $FeTiO_3$ and α-Fe_2O_3 are antiferromagnetic, but their intermediate compositions are known to be ferrimagnetic [72,85]. Moreover, the nanodots display a more metallic character, with a much less pronounced shoulder on the high binding energy side characteristic of Fe^{3+}.

Using the values of p, q and r extracted from figures 6.14 and 6.15, and a value of 6.61 for the *3d* occupation number n_{3d} of bulk iron [80,86], a value of 1.02 μ_B/atom (0.04 μ_B/atom) and 3.48 μ_B/atom (0.18 μ_B/atom) was obtained for m_l and m_s of the nanodots (nanowires). These values differ considerably from the values of m_l = 0.085 and m_s = 1.98 reported in the literature for bulk iron [80,87]. It is important to note that the nanostructures may posses a modified bandstructure compared to that of pure metallic iron, which effects the value of n_{3d} and thus the calculated values of m_l and m_s values may be erroneous. A popular method to circumvent the error introduced by n_{3d} is to calculate the m_l / m_s ratio. Using equation 6.3, a value of 0.29 (0.24) is obtained for the nanodots (nanowires), which is much larger than 0.043 obtained for bulk Fe [88-90]. The enhancement of the ratio over the bulk value has also been reported for other Fe containing systems [72,80,86,91-94].

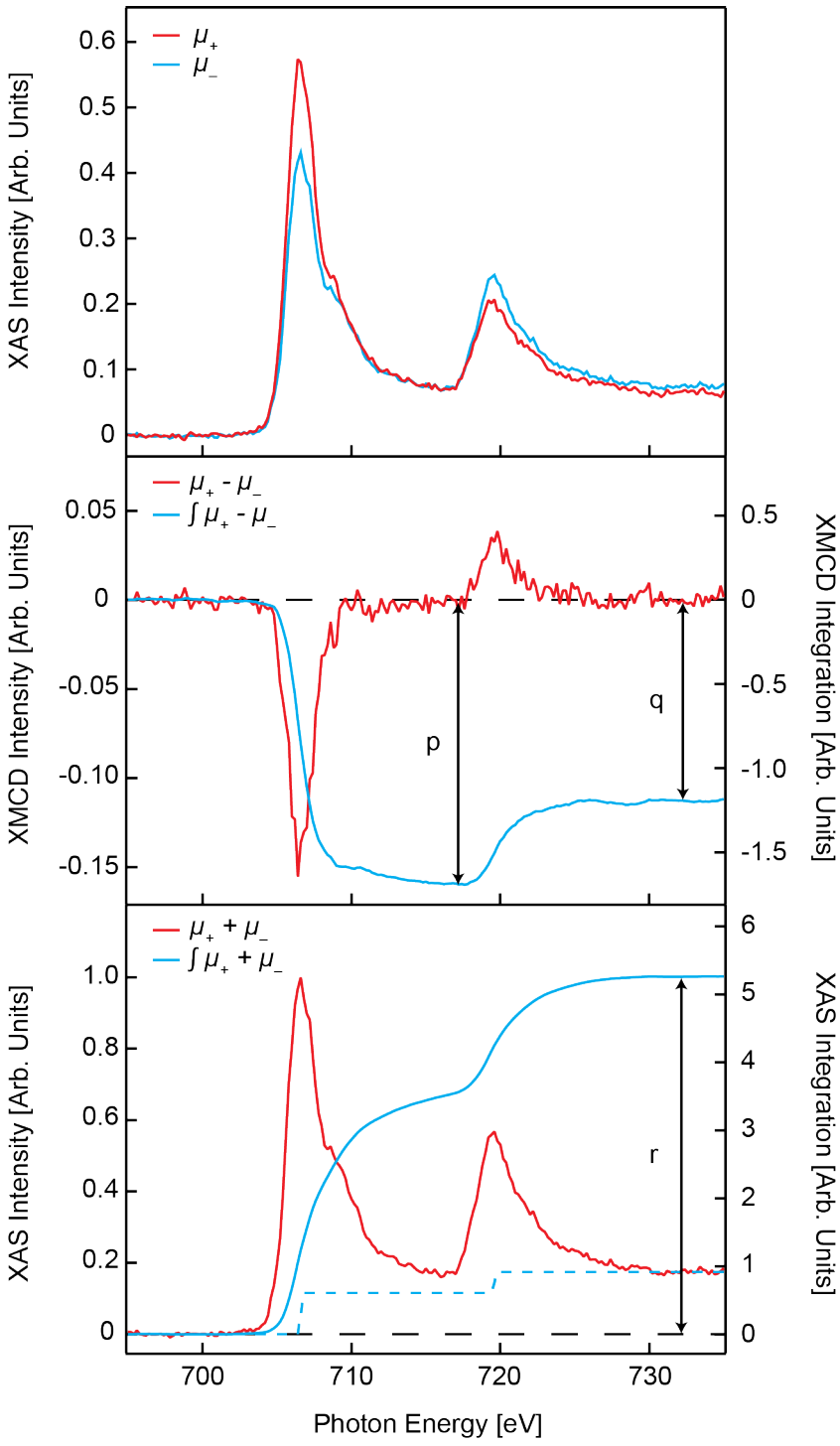

Figure 6.14 – Top: Fe $L_{2,3}$-edge XAS of the nanodots displayed in figure 6.12, acquired using left and right circularly polarised light in total electron yield detection mode. Centre: XMCD spectrum resulting from the XAS difference spectra (red) and integration spectrum of the XMCD signal (blue). Bottom: Sum of the XAS spectra (red) and corresponding integration spectrum (blue) performed after a step-like background was removed (blue dashed line).

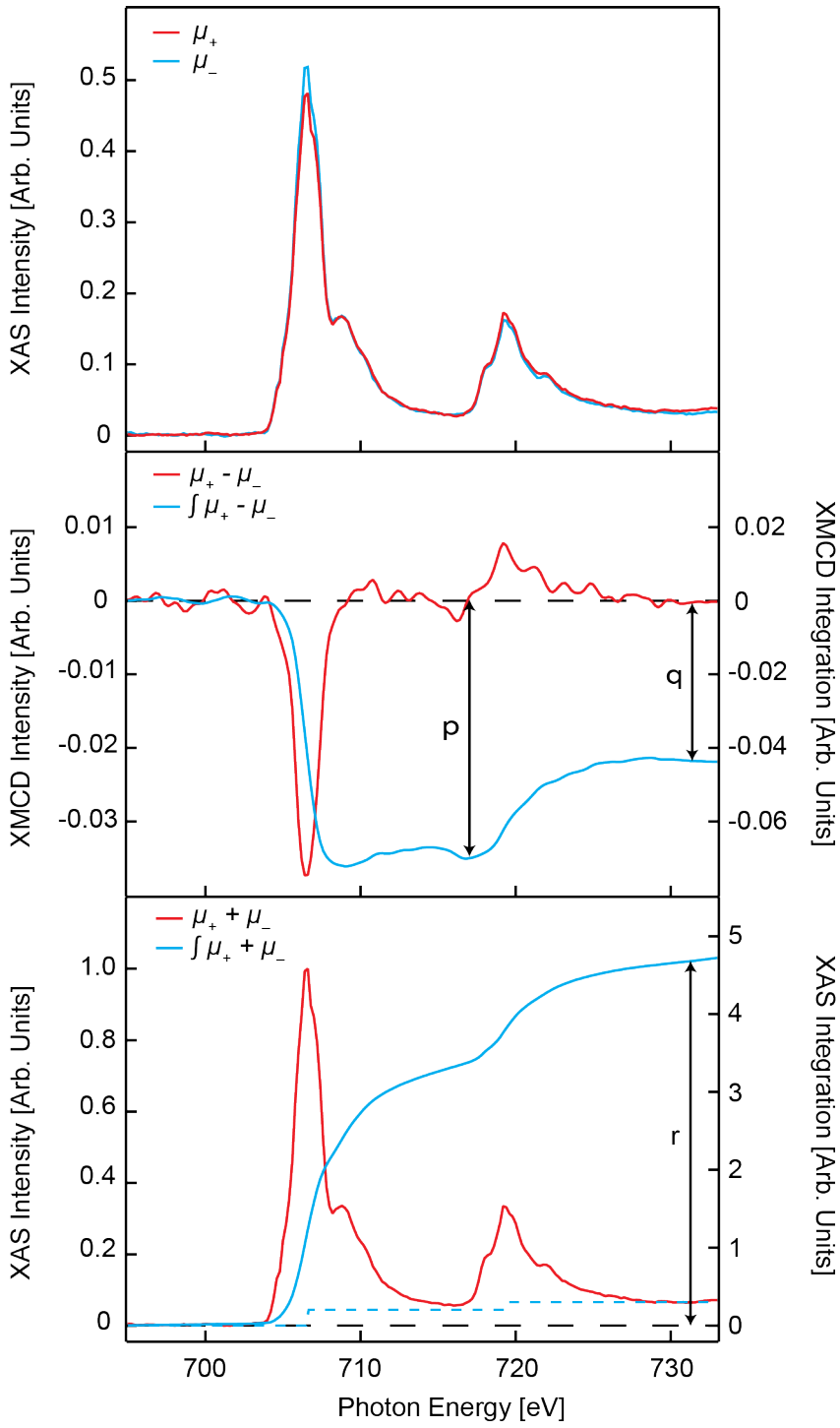

Figure 6.15- Top: Fe $L_{2,3}$-edge XAS of the nanowires displayed in figure 6.12, acquired with left and right circularly polarised light in total electron yield detection mode. Centre: XMCD spectrum resulting from the XAS difference spectra (red) and integration spectrum of the XMCD signal (blue). Bottom: Sum of the XAS spectra (red) and corresponding integration spectrum (blue) performed after a step-like background was removed (blue dashed line).

6.3.3 Spin-Polarised Low Energy Electron Microscopy

Spin-polarised low energy electron microscopy (SPLEEM) is a surface sensitive magnetic imaging technique for studies of the magnetic domain structures of surfaces and thin films [95,96]. The high brightness and highly spin-polarised LEEM instrument used in this study permits magnetic domain structures of surfaces to be observed with a lateral resolution of several nm, with real-time dynamic magnetic imaging [97,98].

The Fe nanowires were grown on a clean rutile TiO_2(110) sample, which was prepared via multiple Argon sputter and UHV anneal cycles as described in section 6.2.2. Displayed in figure 6.16 is a) a LEEM image with a field of view of 50 μm, and two sharp (1x1) LEED patterns acquired using an energy of b) 11 eV and c) 60 eV, indicative of a clean rutile TiO_2(110) surface.

The deposition of Fe on the rutile TiO_2(110)(1×1) surface was performed using an *Omicron EFM-3* electron-beam evaporator, with the substrate held at an elevated temperature (~1000 K). The initial deposition of 8 ML of Fe at ~ 1100 K resulted in the formation of nanowires, an example of which is displayed in figure 6.17. Subsequently, SPLEEM images were acquired with three orthogonal spin-polarisation directions along the $[110]$, $[1\bar{1}0]$ and $[001]$ crystallographic orientation of the substrate. A magnetic image, or asymmetry image, is obtained by acquiring two consecutive images with opposite spin-polarisation (P_0= 90%) by switching the helicity of the laser light; next the difference of the two images is divided by the sum image. The images were acquired with a field of view of 6 μm and no magnetic contrast was observed, as evidenced by the lack of contrast in image c) of figure 6.17.

A second deposition of 8 ML of Fe was also performed on the same sample at a temperature of ~1065 °C. This resulted in the formation of longer nanowires, with lengths up to ~6 μm, as

displayed in figure 6.18. A magnetic contrast study identical to that of the initial Fe deposition was also performed on these larger nanowires, yet no magnetic contrast was observed.

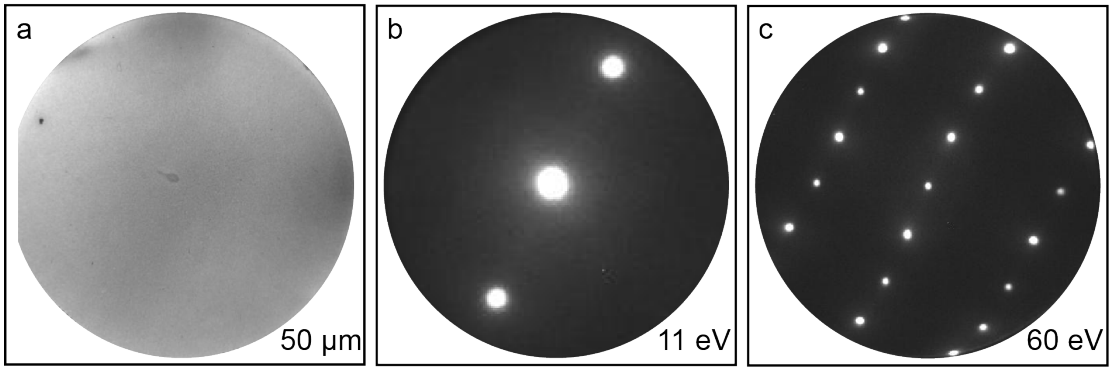

Figure 6.16 – Images pertaining to a clean TiO_2(110) sample acquired after seven sample preparation cycles acquired using a) low energy electron microscopy, b) and c) low energy electron diffraction, where a sharp (1×1) pattern is visible.

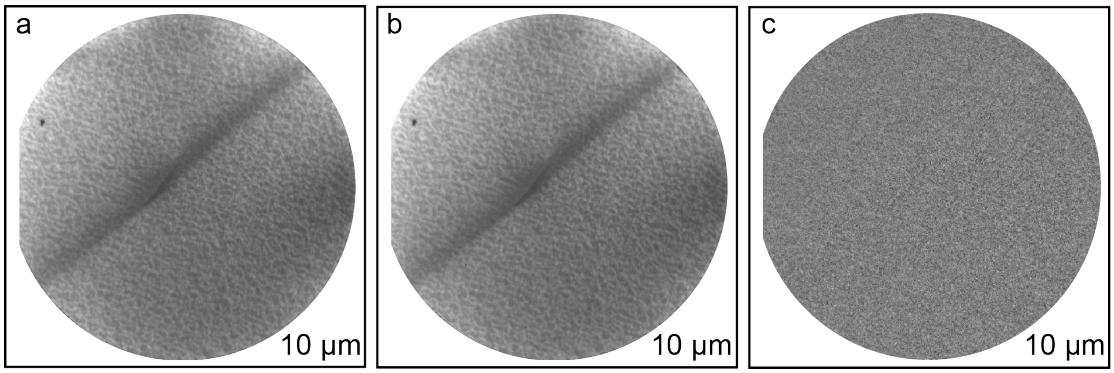

Figure 6.17 – Spin-polarised LEEM images of a typical nanowire formed after the initial deposition of 8 ML of Fe on rutile TiO_2(110), with the sample held at ~ 825°C. Images a) and b) were acquired at room temperature with electron beam polarization vector P // [110] with spin up and spin down, respectively. The resulting asymmetry image is displayed in c), where no magnetic contrast is observed. Images acquired with P // $[1\bar{1}0]$ and P // [001] were also acquired, however still no magnetic contrast was observed. The field of view off all images is 10 µm and the start voltage (SV) is 4.1 V.

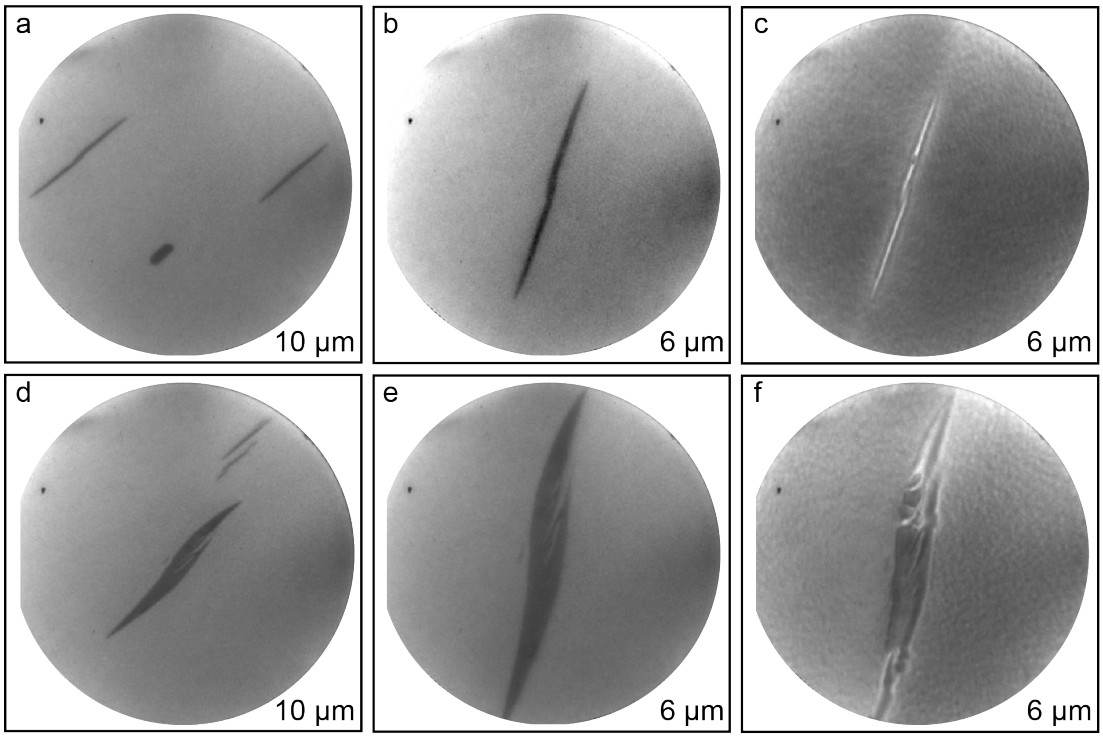

Figure 6.18 – Spin polarised LEEM images of nanowires formed after a second deposition of 8 ML of Fe on rutile TiO_2(110), with the sample held at a temperature of ~ 790°C. Images a), b), d) and e) were acquired with SV= 4.5 eV, whereas images c) and f) were obtained with SV= 4.0 V. The field of view of each image is displayed in the bottom right hand corner.

6.4 Summary and Conclusions

Experiments using multiple surface science techniques were conducted on the Fe/TiO_2(110) system in order to determine its chemical, topological and magnetic properties. The deposition of Fe on rutile TiO_2(110) at elevated temperatures (~1070 K) resulted in the formation of pseudohexagonal islands and nanowires along the [001] direction of the oxide substrate. The chemical structure of the larger nanowires was determined by μ-XPS, whereby the presence of Ti^{4+}, Ti^{3+} species and Fe^{2+}, Fe^{3+} was ascribed to the migration of Ti and O species from the substrate, resulting in the appearance of the reduced Ti species and the encapsulation of the nanowires by Fe-Ti mixed oxides. The presence of a small Fe^0 signal indicates that the core of the nanowires remains in a metallic state, while the Ti^{2+} component of the Ti spectra is assigned to reduction Ti species via beam damage. In contrast, the atomic resolution STM images of the surface of the Fe nanostructures suggest the oxidation of nanowires. Even though much care was taken to grow the Fe nanowires in a reproducible and systematic manner, the topography of the nanowires of each experiment was different (surface roughness, state of reduction, size), which would explain the differences observed in STM and μ-XPS; the encapsulation and oxidation of Fe have both been observed for this system [21,49]. The studies concerning the magnetic properties of the Fe nanowires also produced contrasting results, whereby a magnetic signal was detected in XMCD, but not in SPLEEM. This discrepancy is most likely due to the polarisation of the incident beam ($P_{0,\,SPLEEM}$= 90%, $P_{0,\,XMCD}$= 99%) and the surface sensitivity of each technique, whereby the metallic core of the nanowires is not probed in SPLEEM. The μ-XPS and the XAS results suggest that the nanowires are composed a metallic iron core (Fe^0) and an encapsulation layer formed of mixed Fe-Ti oxides, possibly a combination of $FeTiO_3$ and α-Fe_2O_3, which would explain the presence of Fe^{2+}, Fe^{3+}, Ti^{4+} and Ti^{3+}, and the magnetic signal observed in XMCD. On the other hand, the XAS spectra pertaining to the nanodots exhibit a more metallic character than the nanowires, with a much smaller Fe^{3+} contribution.

References

[1] A. Fujishima and K. Honda, Nature **238**, 37 (1972).

[2] H. Imagawa, A. Tanaka, N. Takahashi, S. Matsunaga, and H. Shinjoh, Studies in Surface Science and Catalysis 609 (2007).

[3] A. Fujishima, T. N. Rao, and D. A. Tryk, Journal of Photochemistry and Photobiology C: Photochemistry Reviews **1**, 1 (2000).

[4] R. Blossey, Nat Mater **2**, 301 (2003).

[5] B. Karunagaran, P. Uthirakumar, S. J. Chung, S. Velumani, and E. K. Suh, Materials Characterization **58**, 680 (2007).

[6] F. Jones, Surf Sci Rep **42**, 75 (2001).

[7] G. X. Shen, R. G. Du, Y. C. Chen, C. J. Lin, and D. Scantlebury, Corrosion **61**, 943 (2005).

[8] M. Grätzel, Nature **414**, 338 (2001).

[9] C. Lun Pang, R. Lindsay, and G. Thornton, Chem. Soc. Rev. **37**, 2328 (2008).

[10] I. Ganesh, P. P. Kumar, and A. K. Gupta, Processing and Application of Ceramics **6**, 21 (2012).

[11] S. Lee, C. Fan, T. Wu, and S. L. Anderson, J. Am. Chem. Soc. **126**, 5682 (2004).

[12] S. Hörold, K. D. Vorlop, T. Tacke, and M. Sell, Catalysis Today **17**, 21 (1993).

[13] Y. Huang, X. Duan, Q. Wei, and C. M. Lieber, Science **291**, 630 (2001).

[14] A. R. Hirst, B. Escuder, J. F. Miravet, and D. K. Smith, Angew. Chem. Int. Ed. **47**, 8002 (2008).

[15] D. R. Cornejo and E. Padrón-Hernández, Journal of Magnetism and Magnetic Materials **316**, 48 (2007).

[16] S. Yang, H. Zhu, D. Yu, Z. Jin, S. Tang, and Y. Du, Journal of Magnetism and Magnetic Materials **222**, 97 (2000).

[17] D. S. Humphrey, G. Cabailh, C. L. Pang, C. A. Muryn, S. A. Cavill, H. Marchetto, A. Potenza, S. S. Dhesi, and G. Thornton, Nano Lett. **9**, 155 (2009).

[18] Z. Majzik, N. Balázs, and A. Berkó, J Phys Chem C **115**, 9535 (2011).

[19] Z. Chang and G. Thornton, Surf Sci **459**, 303 (2000).

[20] M. Bowker, P. Stone, R. Bennett, and N. Perkins, Surf Sci **497**, 155 (2002).

[21] Q. Fu and T. Wagner, Surf Sci Rep **62**, 431 (2007).

[22] J. M. Pan and T. E. Madey, Catal Lett **20**, 269 (1993).

[23] D. Junzhuo, W. Dezheng, W. Xuming, Z. Runsheng, and W. Hongli, Surf Sci **249**, 213 (1991).

[24] N. Nakajima, H. Kato, T. Okazaki, and Y. Sakisaka, Surf Sci **561**, 79 (2004).

[25] Www.Diamond.Ac.Uk **1**, 8 (2016).

[26] S. Okumi, N. Yamamoto, and K. Tamagaki, AIP Conference Proceedings 1085 (2007).

[27] W. Erley and H. Ibach, Solid State Communications **37**, 937 (1981).

[28] T. Miyano, Y. Sakisaka, T. Komeda, and M. Onchi, Surf Sci **169**, 197 (1986).

[29] K. Freindl, T. Ossowski, and M. Zając, The Journal of Physical Chemistry C **120**, 3807 (2016).

[30] J. M. Pan, B. L. Maschhoff, U. Diebold, and T. E. Madey, Surf Sci (1993).

[31] U. Diebold, J. M. Pan, and T. E. Madey, Surf Sci (1995).

[32] A. Wight, N. G. Condon, F. M. Leibsle, G. Worthy, and A. Hodgson, Surf Sci **331-333**, 133 (1995).

[33] J. Weissenrieder, M. Göthelid, and M. Månsson, Surf Sci (2003).

[34] J.-M. Pan and T. E. Madey, J. Vac. Sci. Technol. A **11**, 1667 (1993).

[35] H. Mostéfa-Sba, B. Domenichini, and S. Bourgeois, Surf Sci **437**, 107 (1999).

[36] U. Diebold, Surf Sci Rep **48**, 53 (2003).

[37] L. E. Davis, J. F. Moulder, G. E. Muilenberg, and W. M. Riggs, *Handbook of X-Ray Photoelectron Spectroscopy* (Perkin-Elmer Corporation, 1979).

[38] G. Bhargava, I. Gouzman, C. M. Chun, T. A. Ramanarayanan, and S. L. Bernasek, Applied Surface Science **253**, 4322 (2007).

[39] D. A. Shirley, Phys. Rev. B **5**, 4709 (1972).

[40] P. C. J. Graat and M. A. J. Somers, Applied Surface Science **100-101**, 36 (1996).

[41] V. Shubina, L. Gaillet, S. Ababou-Girard, V. Gaudefroy, T. Chaussadent, F. Farças, T. Meylheuc, C. Dagbert, and J. Creus, Applied Surface Science **351**, 1174 (2015).

[42] B. A. Van Hassel and A. J. Burggraaf, Applied Physics A **53**, 155 (1991).

[43] J. T. Mayer, U. Diebold, T. E. Madey, and E. Garfunkel, Journal of Electron Spectroscopy and Related Phenomena **73**, 1 (1995).

[44] J. Pouilleau, D. Devilliers, H. Groult, and P. Marcus, Journal of Materials Science **32**, 5645 (1997).

[45] Jiangbin Xia, Naruhiko Masaki, A. Kejian Jiang, and S. Yanagida, J. Phys. Chem. B **110**, 25222 (2006).

[46] C. Powell and A. Jablonski, *Nist Standard Reference Database 71* (NIST Electron Inelastic–Mean–Free–Path Database— …, 2010).

[47] R. P. Galhenage, H. Yan, S. A. Tenney, N. Park, G. Henkelman, P. Albrecht, D. R. Mullins, and D. A. Chen, J Phys Chem C **117**, 7191 (2013).

[48] Z. H. Qin, M. Lewandowski, Y. N. Sun, S. Shaikhutdinov, and H. J. Freund, J Phys Chem C **112**, 10209 (2008).

[49] Q. Fu, T. Wagner, S. Olliges, and H.-D. Carstanjen, J. Phys. Chem. B **109**, 944 (2005).

[50] L. Gregoratti, T. O. Mentes, A. Locatelli, and M. Kiskinova, Journal of Electron Spectroscopy and Related Phenomena **170**, 13 (2009).

[51] T. Fujii, M. Yamashita, S. Fujimori, Y. Saitoh, T. Nakamura, K. Kobayashi, and J. Takada, Journal of Magnetism and Magnetic Materials **310**, e555 (2007).

[52] B. A. Van Hassel and A. J. Burggraaf, Applied Physics A **52**, 410 (1991).

[53] A. Mehdilo, M. Irannajad, and B. Rezai, Minerals Engineering **70**, 64 (2015).

[54] S. Zhou, G. Talut, K. Potzger, A. Shalimov, J. Grenzer, W. Skorupa, M. Helm, J. Fassbender, E. Čižmár, S. A. Zvyagin, and J. Wosnitza, J. Appl. Phys. **103**, 083907 (2008).

[55] A. Busiakiewicz, Applied Surface Science **311**, 391 (2014).

[56] A. A. Cristóbal, C. P. Ramos, P. G. Bercoff, and P. M. Botta, Materials Chemistry and Physics (2012).

[57] S. Halpegamage, P. Ding, X.-Q. Gong, and M. Batzill, ACS Nano **9**, 8627 (2015).

[58] K. C. Prince, V. R. Dhanak, P. Finetti, J. F. Walsh, R. Davis, C. A. Muryn, H. S. Dhariwal, G. Thornton, and G. van der Laan, Phys. Rev. B **55**, 9520 (1997).

[59] G. Drera, M. C. Mozzati, and P. Galinetto, Appl. Phys. Lett. **97**, 012506 (2010).

[60] K. Okada and A. Kotani, Journal of Electron Spectroscopy and Related Phenomena **62**, 131 (1993).

[61] A. Thomas, W. Flavell, A. Mallick, A. Kumarasinghe, D. Tsoutsou, N. Khan, C. Chatwin, S. Rayner, G. Smith, R. Stockbauer, S. Warren, T. Johal, S. Patel, D. Holland, A. Taleb, and F. Wiame, Phys. Rev. B **75**, 035105 (2007).

[62] F. De Groot, M. O. Figueiredo, and M. J. Basto, Physics and Chemistry of Minerals **19**, 140 (1992).

[63] R. Brydson, H. Sauer, W. Engel, J. M. Thomass, E. Zeitler, N. Kosugi, and H. Kuroda, J. Phys.: Condens. Matter **1**, 797 (1989).

[64] P. Krüger, Phys. Rev. B **81**, 125121 (2010).

[65] de Groot FM, J. Fuggle, B. Thole, and G. Sawatzky, Phys. Rev., B Condens. Matter **42**, 5459 (1990).

[66] G. Drera, L. Sangaletti, F. Bondino, M. Malvestuto, L. Malavasi, Y. Diaz-Fernandez, S. Dash, M. C. Mozzati, and P. Galinetto, J. Phys.: Condens. Matter **25**, 075502 (2013).

[67] G. van der Laan, Phys. Rev., B Condens. Matter **41**, 12366 (1990).

[68] J. P. Crocombette and F. Jollet, J. Phys.: Condens. Matter **6**, 10811 (1994).

[69] Y. Harada, T. Kinugasa, R. Eguchi, and M. Matsubara, Phys. Rev. B **61**, 12854 (2000).

[70] M. Klepka, K. Lawniczak-Jablonska, and M. Jablonski, Journal of Alloys and Compounds **401**, 281 (2005).

[71] F. M. F. de Groot, J. C. Fuggle, B. T. Thole, and G. A. Sawatzky, Phys. Rev. B **41**, 928 (1990).

[72] H. Hojo, K. Fujita, H. Ikeno, T. Matoba, T. Mizoguchi, I. Tanaka, T. Nakamura, Y. Takeda, T. Okane, and K. Tanaka, Appl. Phys. Lett. **104**, 112408 (2014).

[73] E. Beaurepaire, H. Bulou, F. Scheurer, and K. Jean-Paul, editors, *Magnetism and Synchrotron Radiation* (Springer Berlin Heidelberg, Berlin, Heidelberg, 2010).

[74] A. Locatelli and E. Bauer, J. Phys.: Condens. Matter **20**, 093002 (2008).

[75] W. Kuch, H. Hopster, and H. P. Oepen, *Magnetic Microscopy of Nanostructures* (Springer, Berlin, 2005).

[76] B. Thole, P. Carra, F. Sette, and G. van der Laan, Phys. Rev. Lett. **68**, 1943 (1992).

[77] P. Carra, B. T. Thole, M. Altarelli, and B. Wang, Phys. Rev. Lett. **70**, 694 (1993).

[78] G. van der Laan and A. I. Figueroa, Coordination Chemistry Reviews 1 (2014).

[79] T. Funk, A. Deb, S. J. George, H. Wang, and S. P. Cramer, Coordination Chemistry Reviews **249**, 3 (2005).

[80] C. Chen, Y. Idzerda, H. Lin, N. Smith, G. Meigs, E. Chaban, G. Ho, E. Pellegrin, and F. Sette, Phys. Rev. Lett. **75**, 152 (1995).

[81] D. A. Outka and J. Stöhr, J. Chem. Phys. **88**, 3539 (1988).

[82] G. Y. Yang and J. Zhu, Journal of Magnetism and Magnetic Materials **220**, 65 (2000).

[83] M. Altarelli, Nuovo Cimento Della Societa Italiana Di Fisica D-Condensed Matter Atomic Molecular and Chemical Physics Fluids Plasmas Biophysics **20**, 1067 (1998).

[84] R. Nakajima, J. Stöhr, and Y. Idzerda, Phys. Rev. B **59**, 6421 (1999).

[85] T. Fujii, T. Sugano, and M. Nakanishi, Journal of Physics: … (2010).

[86] K. W. Edmonds, C. Binns, S. H. Baker, S. C. Thornton, C. Norris, J. B. Goedkoop, M. Finazzi, and N. B. Brookes, Phys. Rev. B **60**, 472 (1999).

[87] A. Kleibert, K. H. Meiwes-Broer, and J. BANSMANN, Phys. Rev. B **79**, 125423 (2009).

[88] H. Fujisawa, S. Shiraki, M. Furukawa, S. Ito, T. Nakamura, T. Muro, M. Nantoh, and M. Kawai, Phys. Rev. B **75**, 245423 (2007).

[89] H. A. Dürr, S. S. Dhesi, E. Dudzik, D. Knabben, G. van der Laan, J. B. Goedkoop, and F. U. Hillebrecht, Phys. Rev. B **59**, R701 (1999).

[90] P. Schattschneider, *Linear and Chiral Dichroism in the Electron Microscope - Google Books* (CRC Press, 2012).

[91] L. R. Shelford, T. Hesjedal, L. Collins-McIntyre, S. S. Dhesi, F. Maccherozzi, and G. van der Laan, Phys. Rev. B **86**, 081304 (2012).

[92] E. Goering, S. Gold, M. Lafkioti, and G. Schutz, Europhys. Lett. **73**, 97 (2007).

[93] J. Vogel, A. Fontaine, V. Cros, F. Petroff, J.-P. Kappler, G. Krill, A. Rogalev, and J.

Goulon, Phys. Rev. B **55**, 3663 (1997).

[94] J. Chen, D. J. Huang, A. Tanaka, C. F. Chang, S. C. Chung, W. B. Wu, and C. T. CHEN, Phys. Rev. B **69**, 085107 (2004).

[95] N. Rougemaille and A. K. Schmid, Eur. Phys. J. Appl. Phys. **50**, 20101 (2010).

[96] M. S. Altman, J. Phys.: Condens. Matter **22**, 084017 (2010).

[97] M. Suzuki, K. Kudo, K. Kojima, and T. Yasue, J. Phys.: Condens. Matter **25**, 406001 (2013).

[98] M. Suzuki, M. Hashimoto, T. Yasue, T. Koshikawa, Y. Nakagawa, T. Konomi, A. Mano, N. Yamamoto, M. Kuwahara, M. Yamamoto, S. Okumi, T. Nakanishi, X. Jin, T. Ujihara, Y. Takeda, T. Kohashi, T. Ohshima, T. Saka, T. Kato, and H. Horinaka, Appl. Phys. Express **3**, 026601 (2010).